https://ntrs.nasa.gov/search.jsp?R=19860013161 2020-03-20T15:05:01+00:00Z

N. G. Stanch ED31

LMSC-HEC TR F042555

DUCT FLOW NONUNIFORMITIES STUDY FOR SPACE SHUTTLE MAIN ENGINE

Technical Report

Contract NAS8-34507

August 1985

By

Jürgen Thoenes

(NASA-CR-178734) DUCT FLOW NONUNIFORMITIES STUDY FOR SPACE SHUTTLE MAIN ENGINE (Lockheed Missiles and Space Co.) 129 p HC A07/MF A01 CSCL 21H G3/20

N86-22632 Unclas 08800

Prepared for

NATIONAL AERONAUTICS AND SPACE ADMINISTRATION
MARSHALL SPACE FLIGHT CENTER, AL 35812

APR 1986 RECEIVED NASA STI FACILITY ACCESS DEPT.

by

Lockheed
Missiles & Space Company, Inc
Huntsville Engineering Center
4800 Bradford Drive, Huntsville, AL 35807

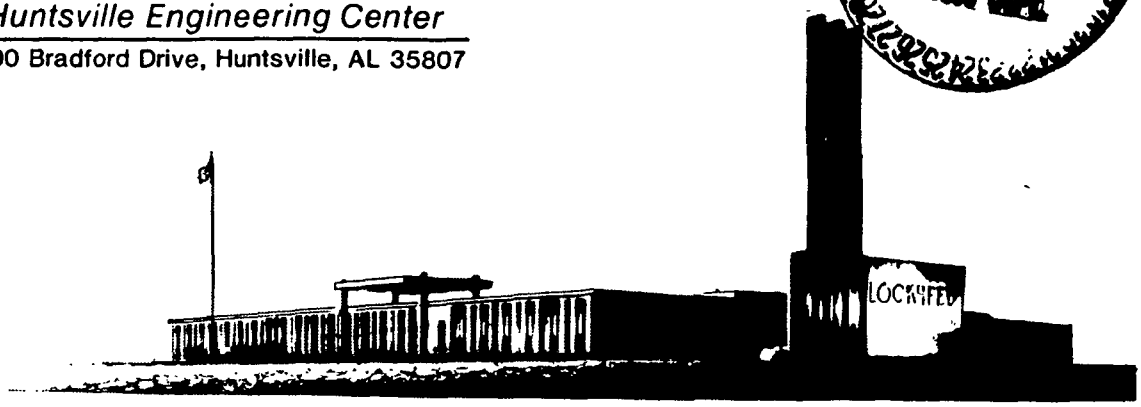

FOREWORD AND ACKNOWLEDGMENTS

This study was performed under Contract NAS8-34507 with Mr. Heinz Struck of NASA-Marshall Space Flight Center serving as technical monitor. Appreciation is expressed for his critical comments throughout the course of this investigation.

The experimental part of the study was performed by personnel of Rockwell International/Rocketdyne Division under Subcontract No. SM8OC6620M to Lockheed with Mr. Dennis G. Pelaccio serving as principal investigator. The cooperation and patience of Rocketdyne personnel in clarifying the many questions which arose from the experimental effort is very much appreciated. The summary of the experimental effort contained in the present report was largely taken from their documentation. The computational part of this study could not have been completed without the help of past and present members of the Lockheed-Huntsville Computational Mechanics Group. The author is grateful for all their contributions to this effort.

PRECEDING PAGE BLANK NOT FILMED

CONTENTS

LIST OF TABLES

LIST OF FIGURES

1. INTRODUCTION AND SUMMARY

Much of the U.S. activity in space over the coming years will be dependent upon the Space Shuttle and its derivative versions as a principal space transportation system. This dependence requires improved designs or techniques to extend the life, upgrade performance, reduce weight, lower operational costs, and generally improve the functional capability of the main propulsion system. The engines for this main propulsion system are advanced high pressure engines operating on oxygen and hydrogen. A need therefore exists to investigate, develop, and define basic concepts in support of the main propulsion system improvements. One basic area that bears investigation is the hot gas flow nonuniformities that occur within the manifold, duct work, and main injector. Nonuniformities result from highly distorted and mismatched flows within the ducts which create severe environments for the system components, thus limiting their useful life.

Development and verification tests of the Space Shuttle Main Engine (SSME) have shown that the three gas transfer tubes have an uneven flow distribution with large areas of separated flow. The outer transfer tubes each carry approximately twice as much of gas as the center tube. This causes the energy of the gas to be much higher in the outer tubes. Flow from the tubes impinge upon the main injector liquid oxygen posts which bend under the static load of the gas flow, the bending being more pronounced in line with the outer tubes. To alleviate this phenomenon and to keep the posts cooler, shields, linking pairs of posts in the outermost row, were installed. The design alteration enhanced the injector life; however, LOX post failures have shown that this change alone is insufficient to grant specified life at equal to or greater than rated power levels. Incorporation of the shields also affects circumferential flow in the annulus and degrades the engine performance and necessitates higher operating temperatures in the turbines.

To improve the SSME design and for future use in the development of new generation rocket engines, a combined experimental/analytical study was undertaken with the goals of first, establishing an experimental data base for the flow conditions in the SSME high pressure fuel turbopump (HPFTP) hot gas manifold (HGM) and, second, setting up a computer model of the SSME HGM flow field. Using the test data to verify the computer model it should be possible in the future to computationally scan contemplated advanced design configurations and limit costly testing to the most promising design.

This report documents in detail the effort of establishing and using the computer model. The experimental effort, performed by Rocketdyne under subcontract to Lockheed, is described in a companion report entitled "Duct Flow Nonuniformities Study, Final Report" (Ref. 1), while a shorter summary can be found in Ref. 2.

For the benefit of the reader, a brief summary of the experimental effort is also presented in Chapter 2 of the present report. The analytical work, performed by Lockheed, is described in detail in the main portion of the present report.

The comparison of computational results and experimental data observed as a result of this study clearly demonstrate that computational fluid mechanics (CFD) techniques can be used successfully to predict the gross features of three-dimensional fluid flow through configurations as intricate as the SSME turbopump hot gas manifold. Although gaps in the technology remain, such as the unavailability of an accurate turbulence model for internal flows, the principal factor which presently limits the extent to which prediction calculations can be performed is cost. Detailed calculations require high resolution. In spite of the great progress achieved in the last decade both with regard to computational methodology and facilities, such calculations must still be judged as too expensive to be performed routinely.

The high cost of experimental efforts, both with respect to hardware and labor, is, of course, common knowledge. For this reason, fewer measurements were performed than would have been desirable for this study. Careful examination of the data obtained raised almost as many questions as it answered, and pointed to the need for more detailed measurements, particularly in places of the configuration where the nature of the flow is uncertain.

2. SUMMARY OF EXPERIMENTAL EFFORT

2.1 INTRODUCTION

In this study, a full-scale, modified, fuel-side SSME was evaluated using a high-pressure, ambient-temperature, air blowdown system, which was directed toward improving the overall flow distribution and decreasing turbulence levels in the turbine exit, turnaround duct, and transfer duct regions compared to the present SSME hot-gas manifold design. Detailed steady state pressure measurement surveys were performed of the HGM fuel side flow field, using wall static ports, total pressure Kiel probes, directional probes, and total pressure rakes. Some high frequency pressure measurements were also included to quantify the turbulent nature of the flow.

Data were scaled to engine conditions and were compared to similar data for the current SSME three-duct HGM design. From these comparisons, flow system improvement trends associated with the advanced SSME hot-gas manifold design concept were then established.

2.2 TEST CONFIGURATION

A number of advanced HGM fuel-side design concepts were conceived and evaluated (Ref. 1). The concept options generated were guided by two major goals: (1) to produce a more favorable flow environment for the SSME main combustion chamber LOX injector posts and HPFT turbine by improving transfer duct flow distribution, velocity profile uniformity, decreasing turbulence levels, and minimizing streamline pressure losses; and (2) compatibility with flow conditions associated with projected increased SSME power levels. These HGM concepts were evaluated in terms of their flow aerodynamic, thermodynamic, structural, system integration, and fabrication

characteristics. From this design option task, an enlarged area, fuel-side, two-transfer duct concept was selected as the HGM configuration that was fabricated, tested, and analyzed in this study.

The selected design has the following key features incorporated on the fuel turbine side of the manifold: (1) two 6.50-inch diameter ducts that increase flow area approximately 30 percent over the current configuration decreasing the flow dynamic head proportionally; (2) increase in turnaround duct area, 8-deg outer wall fairing after the 180-deg turn to decrease the flow dynamic head; (3) slightly rounded duct inlets to assist in turning the flow into the transfer ducts; (4) slightly rounded duct outlets to assist in distributing the flow around the main injector LOX post bundle; (5) faired transfer ducts into the fuel preburner housing to assist in directing flow into transfer ducts and decreasing the HPFT exit pressure gradient; (6) faired transfer ducts into the main injector housing to assist in distributing flow around the main injector LOX post bundle; (7) increasing the HGM fishbowl volume by eliminating the present liner element to decrease the flow dynamic head in this region; and (8) compatibility to incorporate contoured turning vanes to assist in distributing flow into the transfer ducts and decreasing the HPFT exit pressure gradient. A schematic layout of this advanced HGM design identifying its key features is shown in Fig. 1.

A comparison of the two-duct HGM to the current SSME HGM design is displayed in Table 1. The major area increase in the turnaround duct exit area, fishbowl cross-sectional area, and duct cross-sectional area associated with the two-duct HGM design tends to decrease the flow dynamic pressure for a given operational setting, which assists in gradual turning of the flow. These HGM design features also improve duct flow distribution, uniformity, and decrease flow turbulence, as well as assist in producing uniform flow conditions at the HPFT exit.

A low-cost philosophy guided the design and fabrication of the hot-gas manifold test article. An existing surplus SSME hot-gas manifold was

Table 1 HGM DESIGN COMPARISONS

	SSME HGM Current Design	Flow Study Design Model, Two Ducts	Percentage Difference Two-Duct Design SSME Design
Turnaround Duct	FPL**	RPL (FMOF)+	-
Turnaround Duct Exit Area	29.5 in^2	49.68 in^2	68.5
Fishbowl Cross-Sectional Area	6.05 in^2	10.6 in^2	75.3
Duct Cross-Sectional Area	51 in^2	66.3 in^2	30.0
Faired Duct Inlets*	Yes	Yes	-
Faired duct Outlets	No	Yes	-

*Slightly rounded.
**Full power level configuration.
+Rated power level, first manned orbital flight configuration.

modified to produce the advanced, two-duct HGM test article. Additionally, where applicable, internal flow simulation components and instrumentation techniques that were successfully demonstrated in past HGM flow studies for the present SSME engine design (Ref. 3) were used. Numerous steady-state and high-frequency pressure instrumentation ports were incorporated in the fuel side of the model to define the flow field in detail from the model inlet to the transfer duct exits. The test model was designed for a working pressure of 300 psia.

The oxidizer flow was modeled with a preburner/turbine simulator and turnaround duct. Flow enters the oxidizer preburner, which then transitions into an annulus passage that has six long, equally spaced blades to impart a

ORIGINAL PAGE IS
OF POOR QUALITY

swirl velocity component to the flow. The swirling flow is typical of turbine exit flow conditions. The flow then enters the oxidizer turbine exit simulator where the flow direction is changed 180 deg and exits into the large oxidizer side HGM fishbowl region (Fig. 1). In the SSME the oxidizer side HGM fishbowl region contains the heat exchanger component. Flow then exits through the two oxidizer transfer ducts into the main injector. Aluminum and Cres were the materials used in oxidizer side simulator hardware designs. This design simulates the gross features of the SSME oxidizer flow field but lacks proper simulation of flowfield details. The degree of simulation designed into the test model was considered adequate because the oxidizer flow field does not influence the fuel side

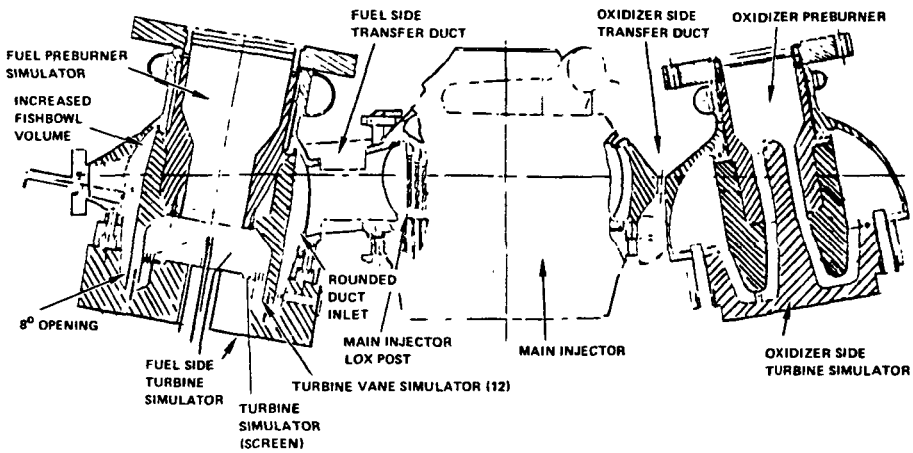

A. SIDE VIEW

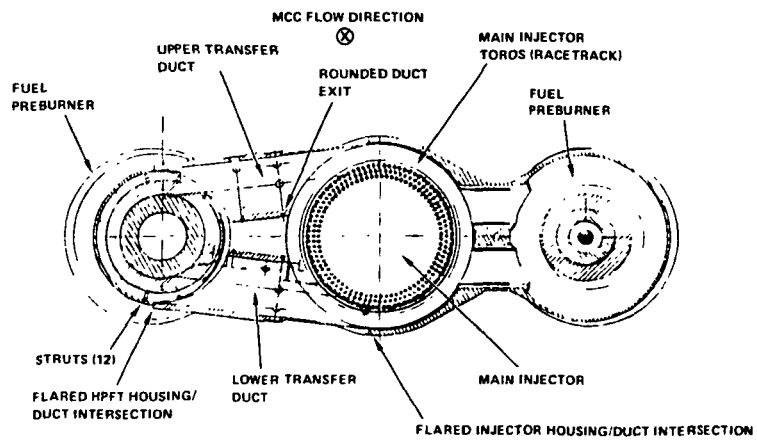

B. TOP VIEW

Fig. 1 Two-Duct HGM Air Flow Test Powerhead Configuration

transfer duct flow field to a great extent. This is considered a good assumption because only approximately 30 percent of the total HGM gas flow goes through the oxidizer side of the HGM, while the remaining 70 percent is passed through the fuel side during hot-fire engine operation, as previously mentioned.

In contrast to the oxidizer side simulator design, the fuel preburner/turbine simulation hardware was designed to simulate the SSME fuel side flow field in detail. Like the oxidizer side simulator, the fuel side simulator was based on a design that was successfully demonstrated in past HGM flow studies. Past flow study test data showed that this simulator design produced an HGM fuel side flow that correlated well with that measured in an SSME engine. In this design, the flow enters the fuel preburner simulator where it is manifolded into an annular passage. At the annular passage entrance, a turbine simulator screen is placed to produce flow effects that are characteristic of those associated with a 15 deg swirl angle clockwise if viewed in the direction of the flow downstream of the screen, which is typical of SSME HPFT exit flow conditions at rated power level. Constant velocity conditions are produced by varying the orifice diameter as a function of radial position. The screen was designed for a pressure loss coefficient ($\Delta p_t/q$) of 5.6, which is approximately 25 percent of that exibited by the HPFT while still having enough resistance to stabilize flow exit conditions. Twelve thin fins, which span the width of the annular channel, are positioned just downstream of the screen exit in an equally spaced circumferential fashion. These fins simulate flow interference blockage associated with the turbine exit coolant liner supports. They are set at an angle of attack to the flow because of the swirl angular velocity component, and therefore add eddy vortex (vorticity) structure to the flow. The flow then changes direction, 180 deg, in the turnaround duct region. The turnaround duct geometry simulates that used on the Space Shuttle Columbia's first set of flight engines known as the First Manned Orbital Flight (FMOF) configuration. Downstream of the 180 deg turn, the outer wall of the annular flow channel is designed with an outward 8 deg

taper. Twelve large support struts are then equally spaced circumferentially in the annular passage at the fishbowl entrance and simulate major structural components associated with the engine in this region. In the design of the HGM fuel-side fishbowl, the coolant liner was removed to increase the fishbowl volume. Two 6.5-in. constant ID ducts were integrated into the fishbowl and main injector housing, completing the fuel-side gas flow path to the main injector assembly. The coolant liner on the fuel side of the main injector was removed to accommodate the large transfer ducts. The two-duct HGM design also incorporates slightly rounded entrance and exit duct geometries and flush internal surfaces at the outer intersection points between the transfer ducts and the HGM fuel preburner and main injector housing (Fig. 1). Like the oxidizer simulator hardware, the fuel side simulation hardware was designed to be made of aluminum and Cres material.

The SSME powerhead main injector was designed to be removable for ease in instrumentation and configuration changes. A modified SSME main combustion chamber (MCC), which incorporates the addition of a long throat ASME flow metering type nozzle is bolted to the HGM main injector exit face. The flow metering nozzle chokes the flow maintaining high pressure within the flow model and also functions as a model total flow metering device.

Integration of an extensive amount of pressure instrumentation was incorporated into the fuel side test model. The model instrumentation measurement locations were placed to give detailed steady-state flow field definition at the model inlet, turnaround region, fishbowl entrance, transfer duct entrance and exit planes. High frequency instrumentation was included in the model to give a qualitative assessment of the turbulent nature of the flow. A layout of instrumentation (location and type) is shown in Fig. 2 and listed in the legend given in Table 2, respectively. The upper transfer duct was designed to accept a pressure survey at the entrance. Flow conditions are defined at both transfer duct exits (Symbols

ORIGINAL PAGE IS
OF POOR QUALITY

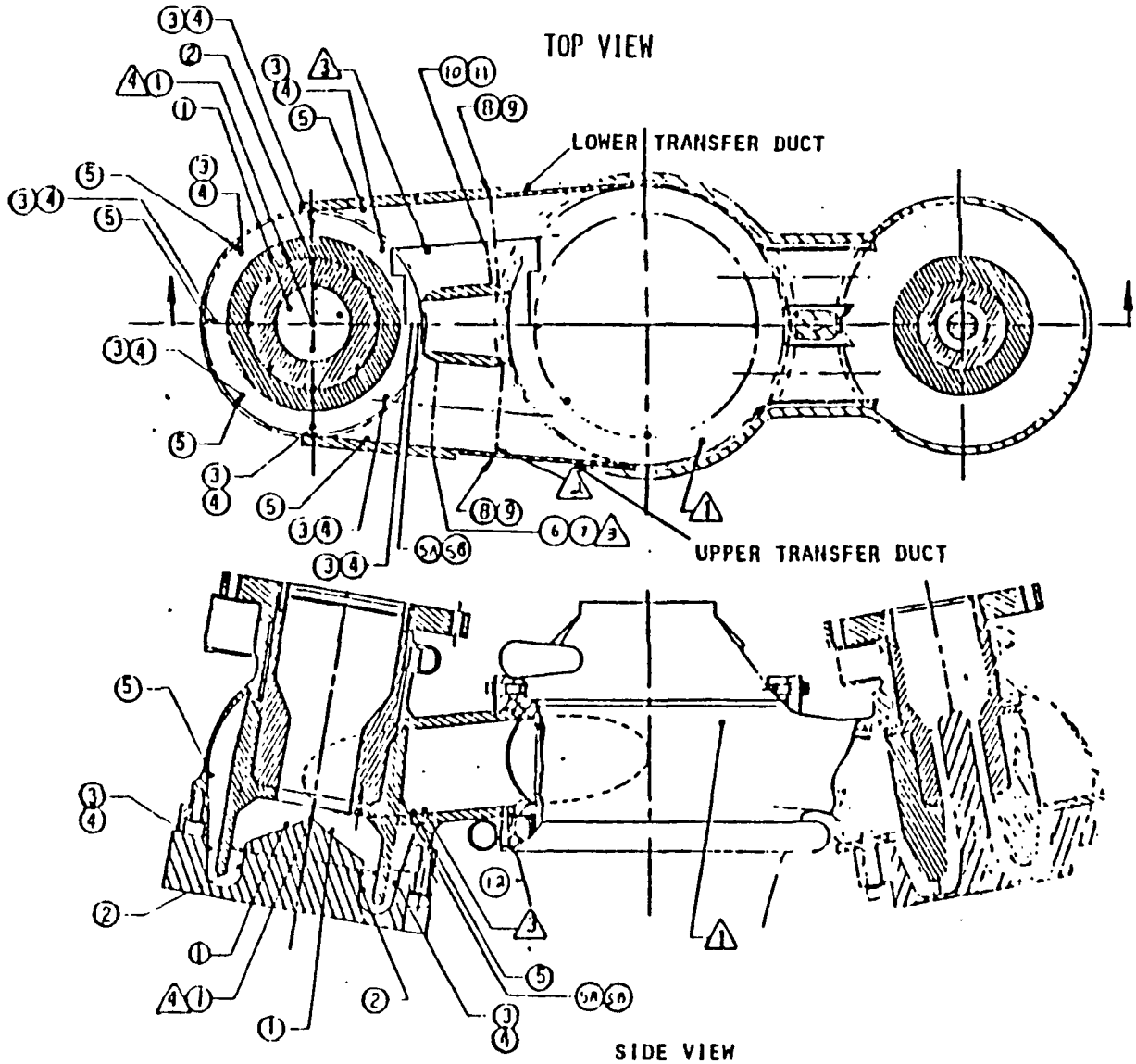

Fig. 2 Instrument Layout

Table 2 TEST ARTICLE INSTRUMENTATION LEGEND

Symbol	Location/Type
	State Pressure Measurements
(1)	Model Inlet/3 Static - 1 Total
2	Screen Exit - Upstream 180 deg Turnaround/Static
3	Downstream 180 deg Turnaround/Static
4	Downstream 180 deg Turnaround/Total
5	Fishbowl - Entrance Upstream of Transfer Duct (3-D Probes)
5A	Fishbowl Entrance/Static
5B	Fishbowl Entrance/Total
6	Transfer Duct Entrance/Static
7	Transfer Duct Entrance/Total
8	Transfer Duct Exit Plane/Total
9	Transfer Duct Exit Plane/Static
10	Transfer Duct Exit Inner Wall/Static
11	Transfer Duct Exit Inner Wall/Total
12	Main Combustion Chamber/Total
	High Frequency Measurements
△1	CG1P - Racetrack Flow
2	Upper Transfer Duct - Exit
3	Upper Transfer Duct - Entrance
4	Fuel Side Model Inlet

8 and 9, Fig. 2) by placement of exit total pressure survey rakes. In the lower duct, a pressure rake element was placed to measure the inner wall region flow field at a position 1.25 in. upstream of the exit rake plane. These total pressure rake elements were designed to be easily removable, have rotational capability, and be interchangeable with all rake locations. When assembled the cross-sectional area blockage of the rakes was no greater than 9 percent of the total transfer duct cross-sectional area. Total pressure Kiel probes were used downstream of the 180 deg turnaround region and three-dimensional directional probes were used to map the flow at the fishbowl entrance plane (Fig. 2).

Detailed measurements were made of the fuel-side HGM internal surfaces to support configuration definition for use by complementary computational model flow analysis efforts (See Chapter 3, also Ref. 4).

2.3 TEST RESULTS

Tests were run at three flow conditions (Reynolds number, based on transfer duct diameter and flow conditions, approximately equal to $2 \cdot 10^6$, $5 \cdot 10^6$, and $7 \cdot 10^6$; see Table 3) to determine the influence of Reynolds number on the fuel-side flow field.

Test repeatability was considered quite good between individual tests at the approximate same operating conditions. In general, little or no Reynolds number effect was observed throughout the HGM fuel-side flow system except at the fishbowl entrance plane where the local dynamic pressure

Table 3 TWO-DUCT/SSME HGM REYNOLDS NUMBER COMPARISON

	Cold Flow 2-Duct			SSME*, Hot-Fire		
	Low Flow	Medium	Maximum	65% Throttle	100% Throttle	109% Throttle
Fuel Mass Flow (lbm/sec)	26.9	52.3	73.5	90.6	151.8	173.0
Re x 10^6	2.59	5.08	7.07	4.57	7.68	8.14
Re/D x 10^7	0.48	0.94	0.94	1.11	1.86	1.98

*Based on Columbia SSME configuration.

circumferential variations increased by approximately one dynamic pressure head at the low Reynolds number test condition ($Re_D \simeq 2.6 \times 10^6$). These results give confidence that at the high Reynolds number test conditions (69 percent of SSME rated power level Reynolds number), the critical Reynolds number conditions have been exceeded as is characteristic of engine operation. This implies that major separation and turbulent flow structure features present in a hot gas manifold operated at engine conditions should also be present in the hot gas manifold cold flow model when operated at high Reynolds number test conditions.

2.3.1 Two-Duct HGM Test Results

In order to compare test results with results to be obtained from model calculations, experimental data in appropriate form are needed for the entire configuration from the turnaround duct inlet (turbine exit) to the transfer duct exit. Constraints and/or limitations with respect to the number of probes as well as the number of channels in the data recording system available unfortunately did not allow the taking of as many data as would have been desirable at exactly the same overall conditions. Table 4 summarizes averaged pressure data obtained from several high Reynolds number test runs. Since little effect of Reynolds number on the qualitative behavior of the flow was noted, we can assume that small variations in Reynolds number should not invalidate a compilation of data from different runs to serve as a data base to: (1) anchor the model calculations; (2) to

Table 4 DFNUS HGM PRESSURE TEST DATA (psi)

Test		1.07	1.09	2.09	2.15	3.06
$\dot{m}$ (lb/sec)		61.63	61.98	73.48	71.34	72.86
TI	p			255.03	244.4	247.6
	p_t			265.95	254.4	258.3
TE	p					176.0
	p_t					188.7
TAD E	p					190.2
	p_t					209.9
BI	p				174.7	
	p_t				179.0	
TD I	p			179.3		
	p_t			(182.3)		
TD E	p	172.9	178.3		169.5	
	p_t	(175.1)	(180.4)			

Legend: TI = Turbine inlet; TE = turbine exit; TAD E = turnaround duct exit; BI = bowl inlet; TD I = transfer duct inlet; TD E = transfer duct exit.

compare theory and experiment; and (3) to provide the overall total pressure loss from the turbine exit to the transfer duct exit.

Inspection of Table 4 reveals that the pressure measurements at the turbine exit (TE, Test 3.06) are inconsistent with those obtained at the turnaround duct exit. The most likely cause for this is the very difficult flow environment that exists where the swirling flow exiting the turbine simulator impinges on the guide vanes which are aligned with the turbine axis. Detailed prior knowledge of the flow field would have been necessary to properly place probes in this region. The difficulty of obtaining data in this region is also believed to be the cause for the oscillations in the circumferential pressure distribution shown in Fig. 3. The bottom line of this discussion is that in order to match the measured data in the computational model, at least those from the turnaround duct exit to the transfer duct exit, the inconsistent measured pressure data at the turbine exit had to be replaced by estimated values based on turnaround duct exit values and an estimate of the pressure loss through the turnaround duct.

The remaining data (Figs. 4 through 8) showing absolute as well as dimensionless circumferential* pressure distributions at the turnaround duct exit and at the fishbowl entrance were used for comparison with results from the computational model.

2.3.2 Comparison of Two-Duct and Three-Duct HGM

The SSME HGM at the exit of the high pressure fuel turbopump imposes considerable circumferential variations in static and total pressure on the turbine. This effect is due to the compactness of the manifold and to its one-sided discharge through the transfer tubes, as confirmed by SSME hot-firing tests, as well as by past HGM air-flow test studies (Ref. 3).

*Circumferential location is defined to be 0 between the transfer ducts and 180 deg at the opposite side.

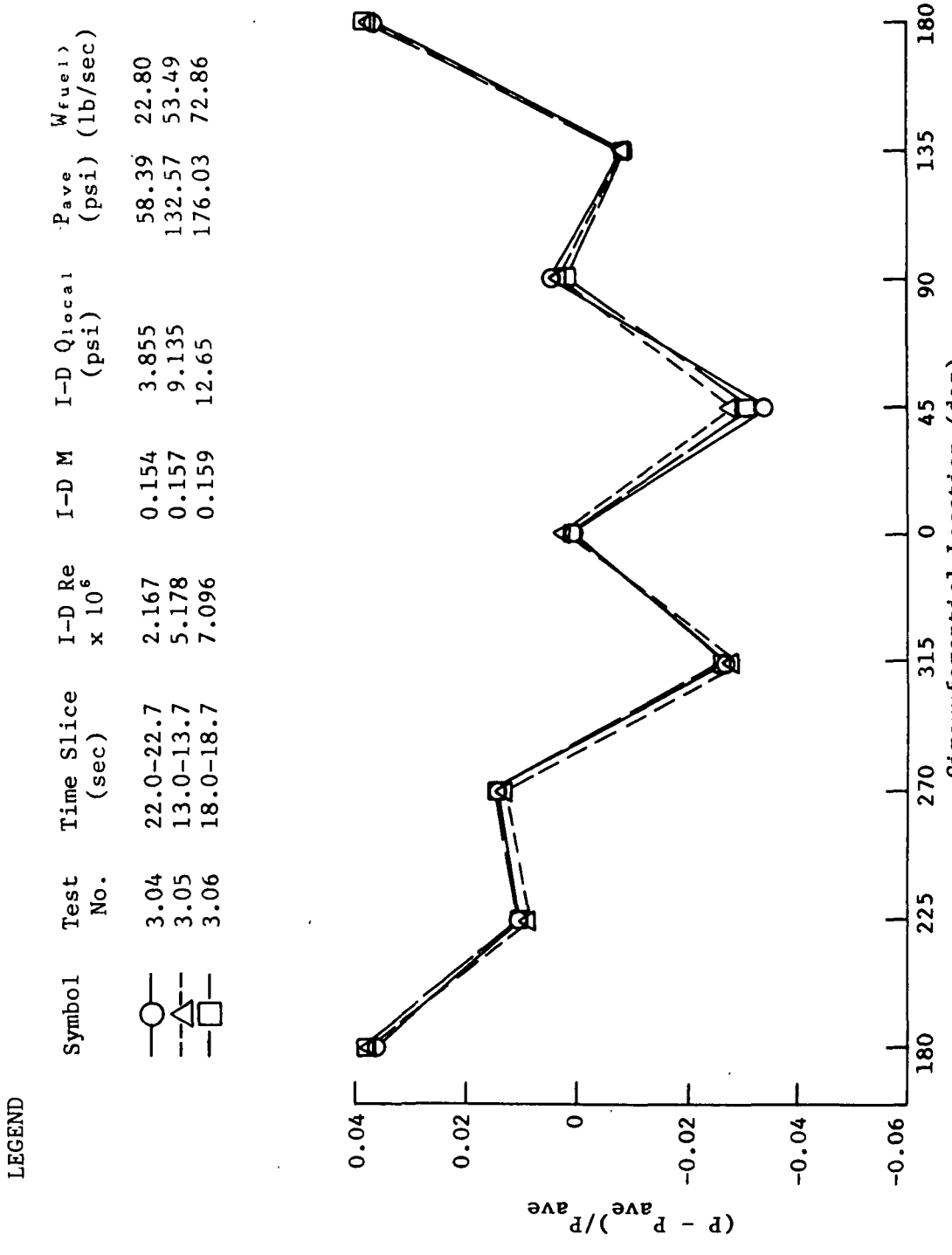

Fig. 3 Screen Exit Static Pressure Distribution

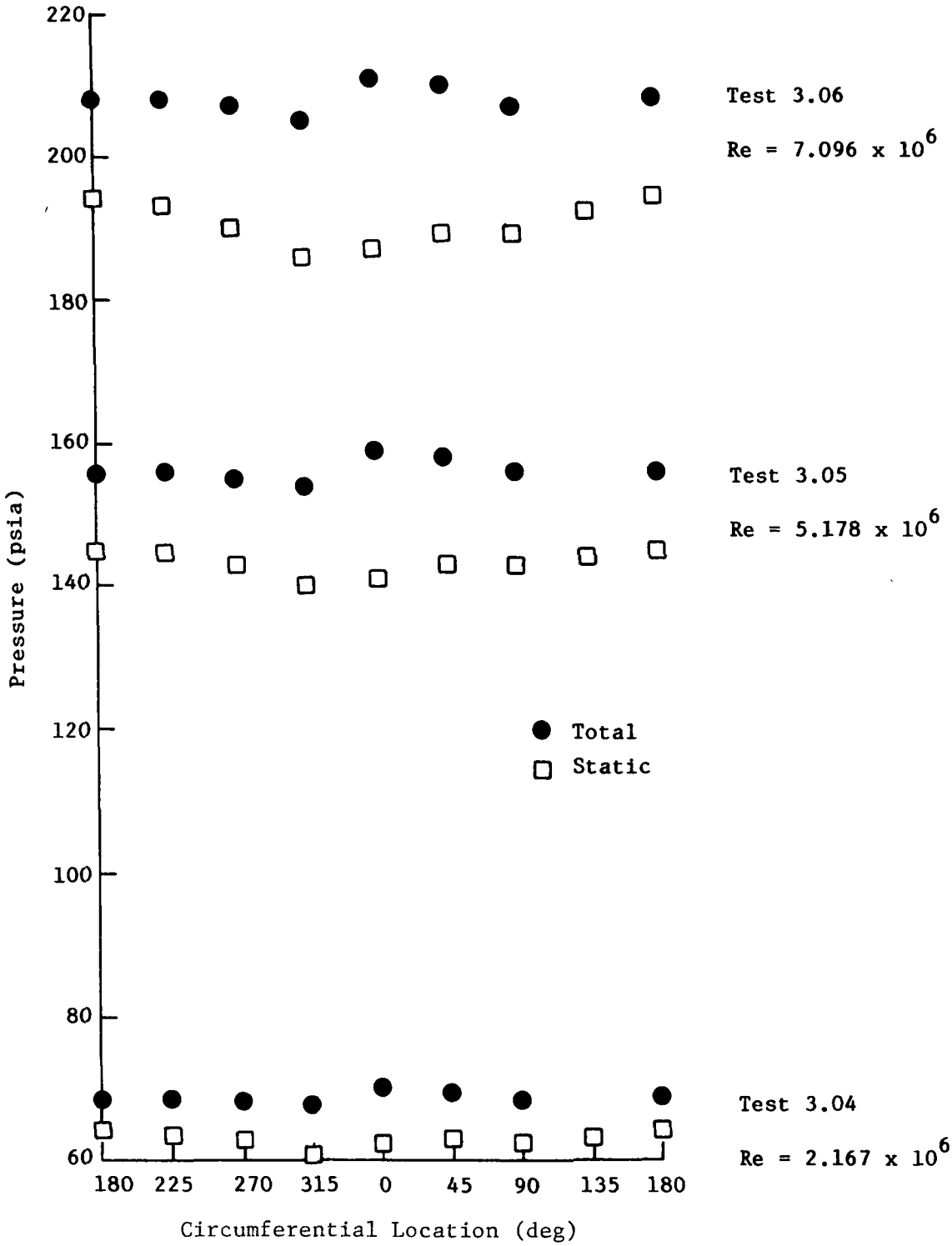

Fig. 4 Static and Total Circumferential Pressure Variation D/S of 180 deg Turn

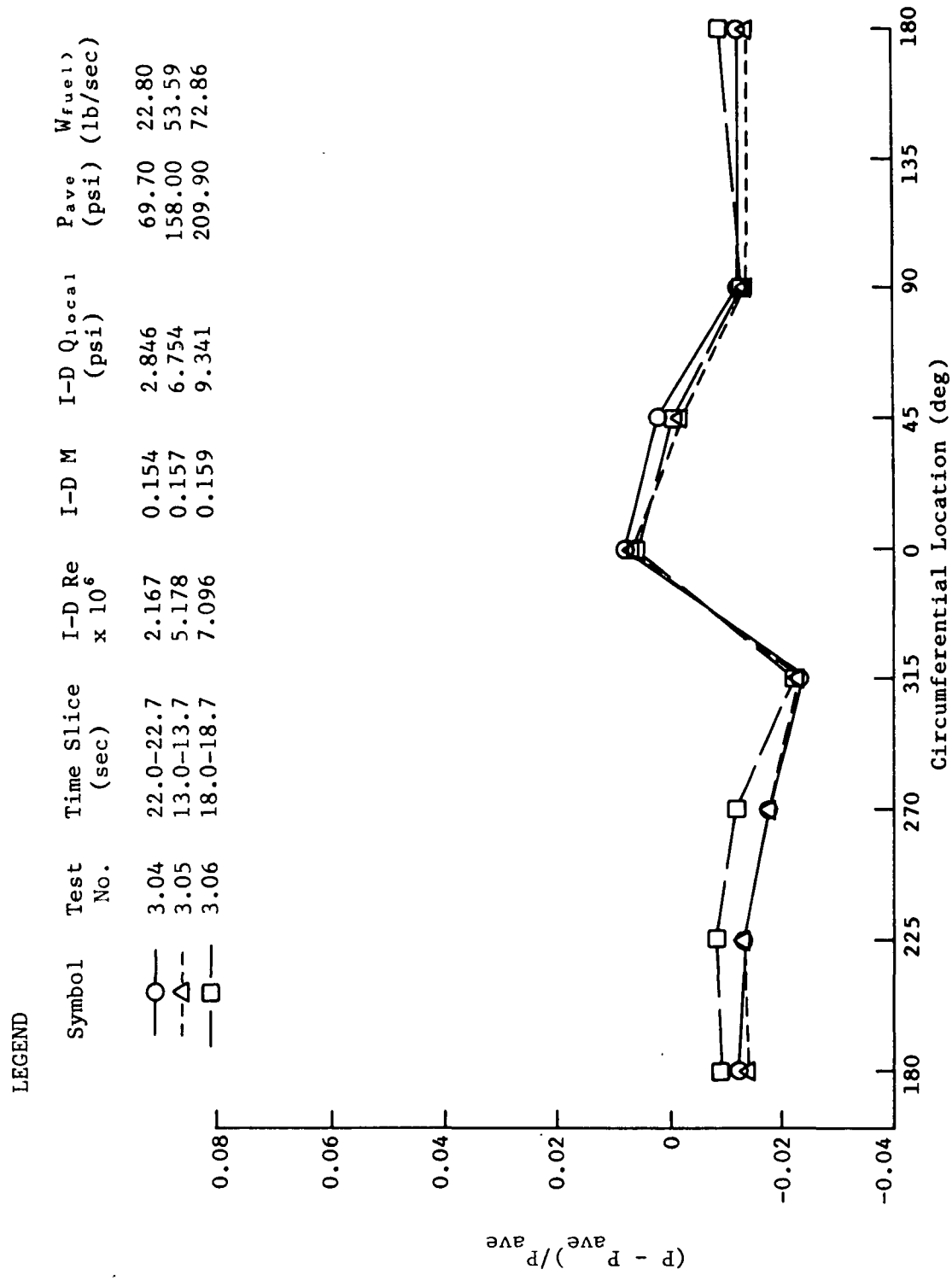

Fig. 5 Downstream 180-deg Turn Total Pressure Distribution

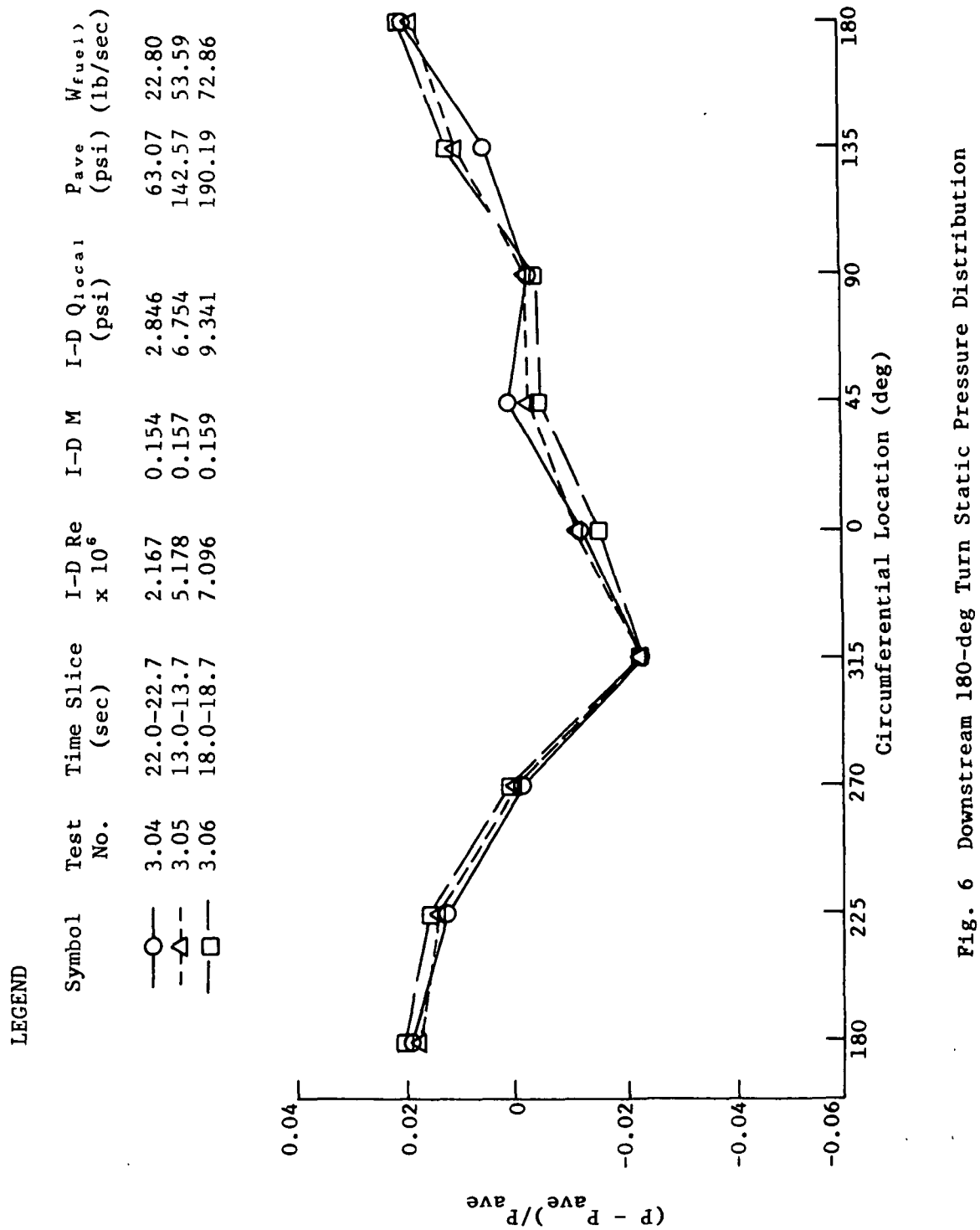

Fig. 6 Downstream 180-deg Turn Static Pressure Distribution

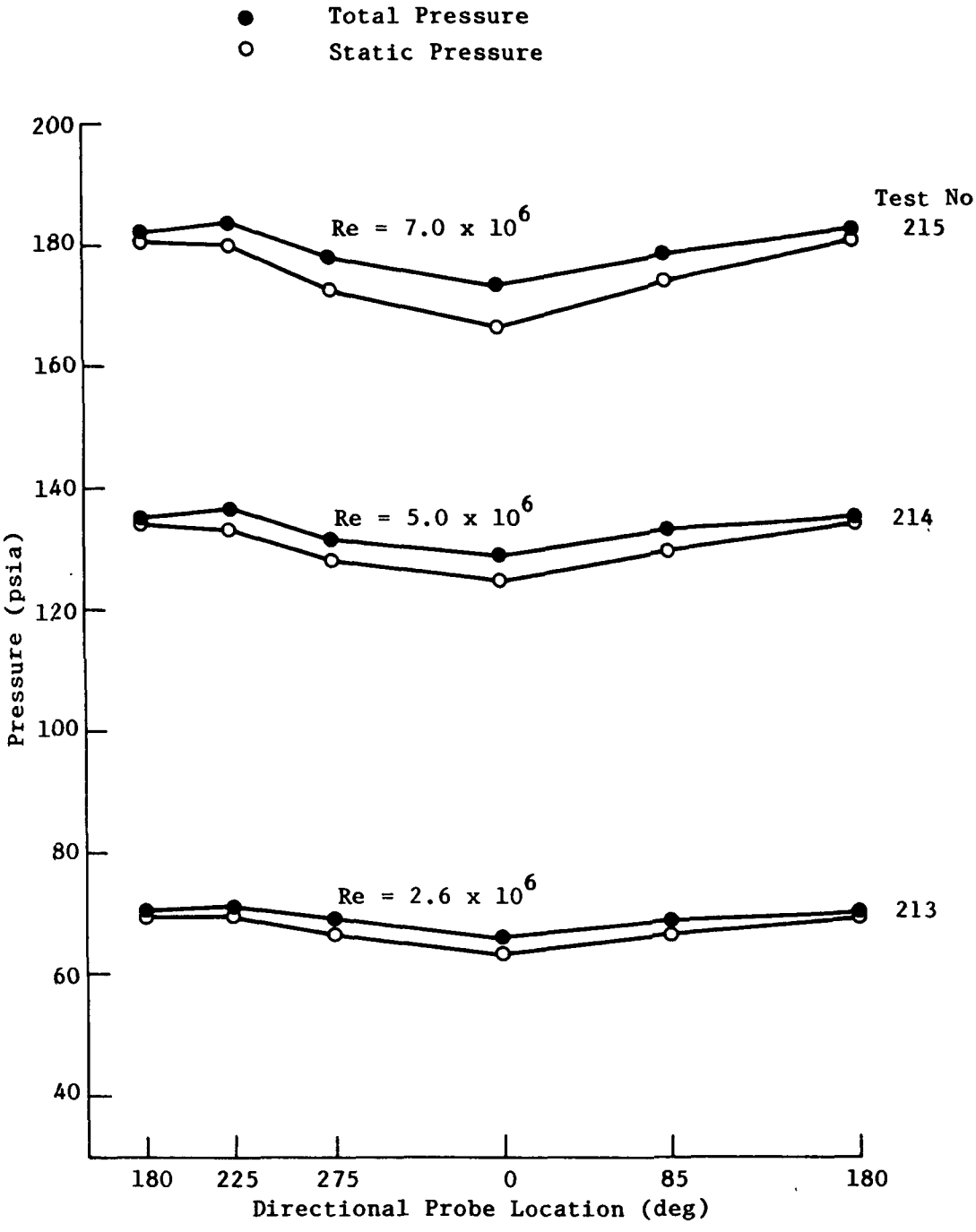

Fig. 7 Two-Duct HGM Fishbowl Entrance Pressure Variation

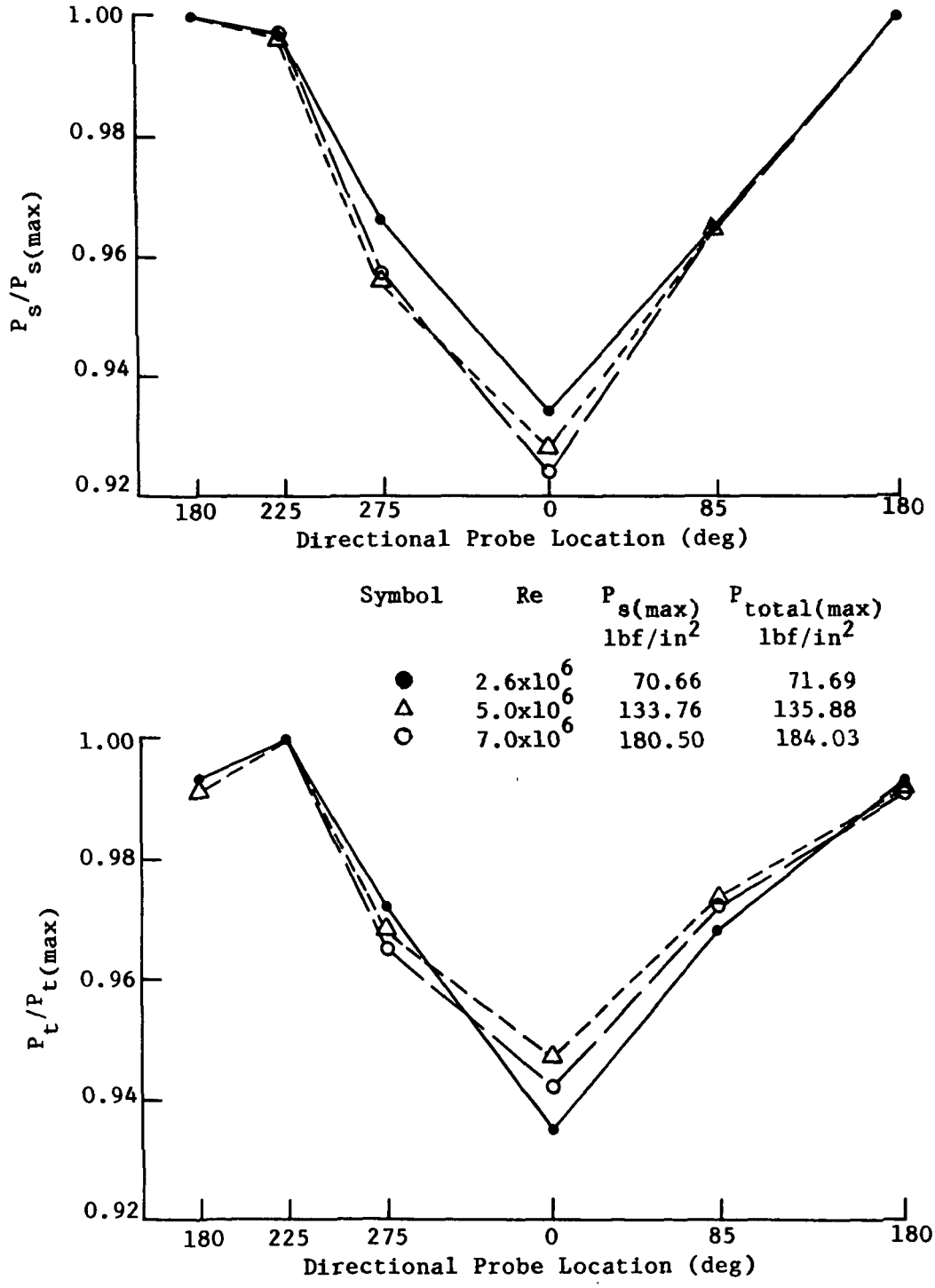

Fig. 8 Two-Duct HGM, Fishbowl Dimensionless Pressure Variation

The two-duct HGM greatly reduced the pressure (flow) nonuniformities in the turbine exit/turnaround duct region compared to the present three-duct SSME design. A reduction of about two-thirds of the total pressure variation around the turbine exit region (Fig. 9) is achieved by the two-duct HGM design.

The turbine simulator screen in the flow model enforces constant velocity conditions implying that the static pressure distribution measured is characteristic of the total pressure distribution. The increased uniformity in the pressure distribution should result in the following improvements: (1) increased turbine life; (2) decreased radial loads and shaft movements, which tend to produce increased clearances and/or rubbing; (3) reduction or avoidance of maldistributions of coolant flow; (4) reduction in deformation and cracking of sheet metal; and (5) decreased HPFT turbine temperatures for a given power level.

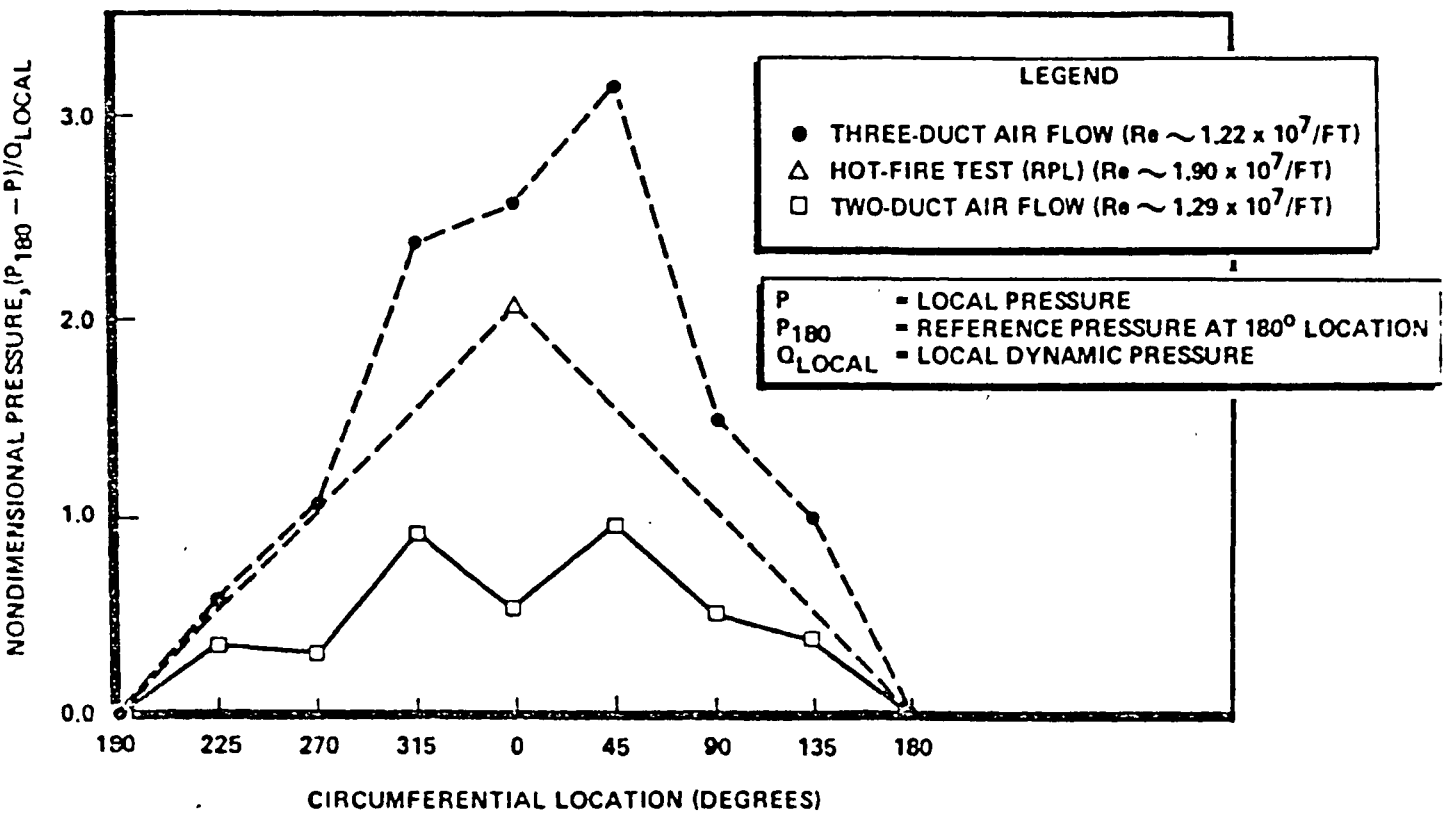

Fig. 9 Circumferential Static Pressure Variation at Turbine Exit

It should be noted when examining the data that a 16-deg swirl was induced in the fuel-side flow at the turbine simulator screen in the clockwise direction (upper to lower transfer duct direction) when viewed from the top (LOX dome) of the flow model. In the fuel-side simulator region, the circumferential location was defined as 0 deg between the two transfer ducts, the position angle increasing in the counterclockwise direction when viewed from the top of the model.

Both the static and total circumferential pressure variation downstream of the 180-deg turnaround duct (Figs. 10 and 11, respectively) were greatly reduced for the two-duct HGM configuration. Examination of Fig. 10 indicates the static pressure difference, referenced at the maximum pressure position at the 180-deg location, is approximately 25 percent of that exhibited in the present SSME HGM design. The minimum static pressure was recorded at the 315-deg location for the two-duct configuration while the three-duct configuration minimum static was identified at 0 deg for HGM air-flow tests and 45-deg for SSME hot-fire tests. The total pressure circumferential pressure variation exhibited for the two-duct HGM is radically different (Fig. 11) from that associated with the present HGM design. The two-duct HGM total pressure distribution varies little and is nearly symmetric with the maximum total pressure located between the two transfer ducts. The increased uniformity in the turnaround duct region in the two-duct hot gas manifold configuration would increase HGM coolant sheet metal liner life over the present design.

The flow through the transfer duct exit planes of the two-duct manifold was more uniform than that present in the current three-duct manifold design. The improvement in flow uniformity should decrease main injector LOX posts loading and increase their operational lifetime.

The percentage of the flow area stagnant is less for the two-duct configuration. A rough comparison of stagnation areas for the two- and three-duct hot gas manifold configurations is displayed in Fig. 12 for

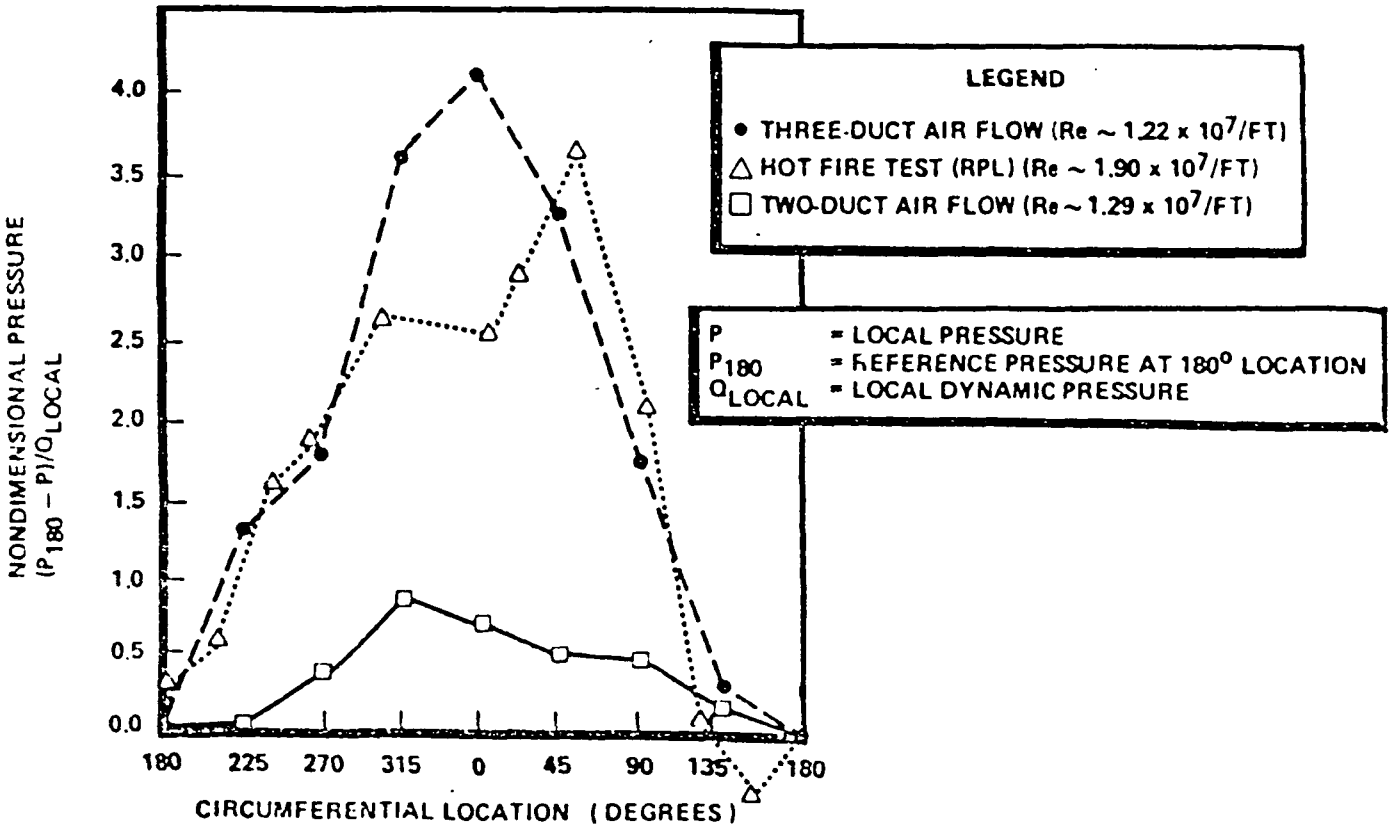

Fig. 10 Static Pressure Variation Downstream of 180-deg Turn

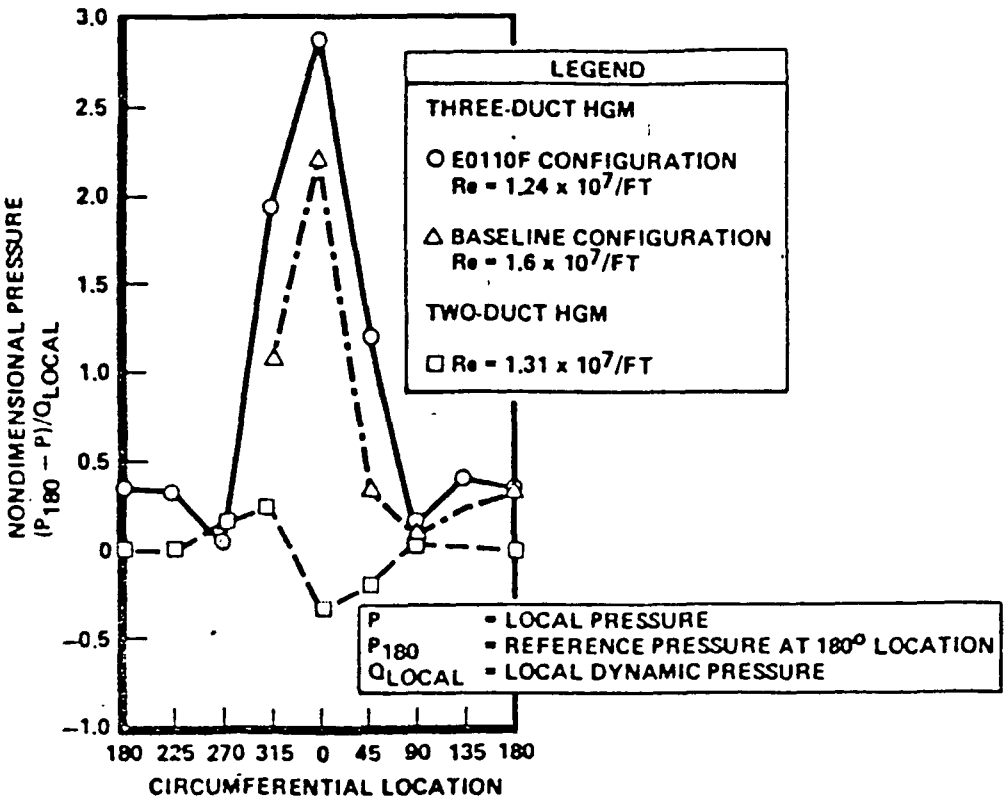

Fig. 11 Total Pressure Variation Downstream of Turnaround Duct 180-deg Turn

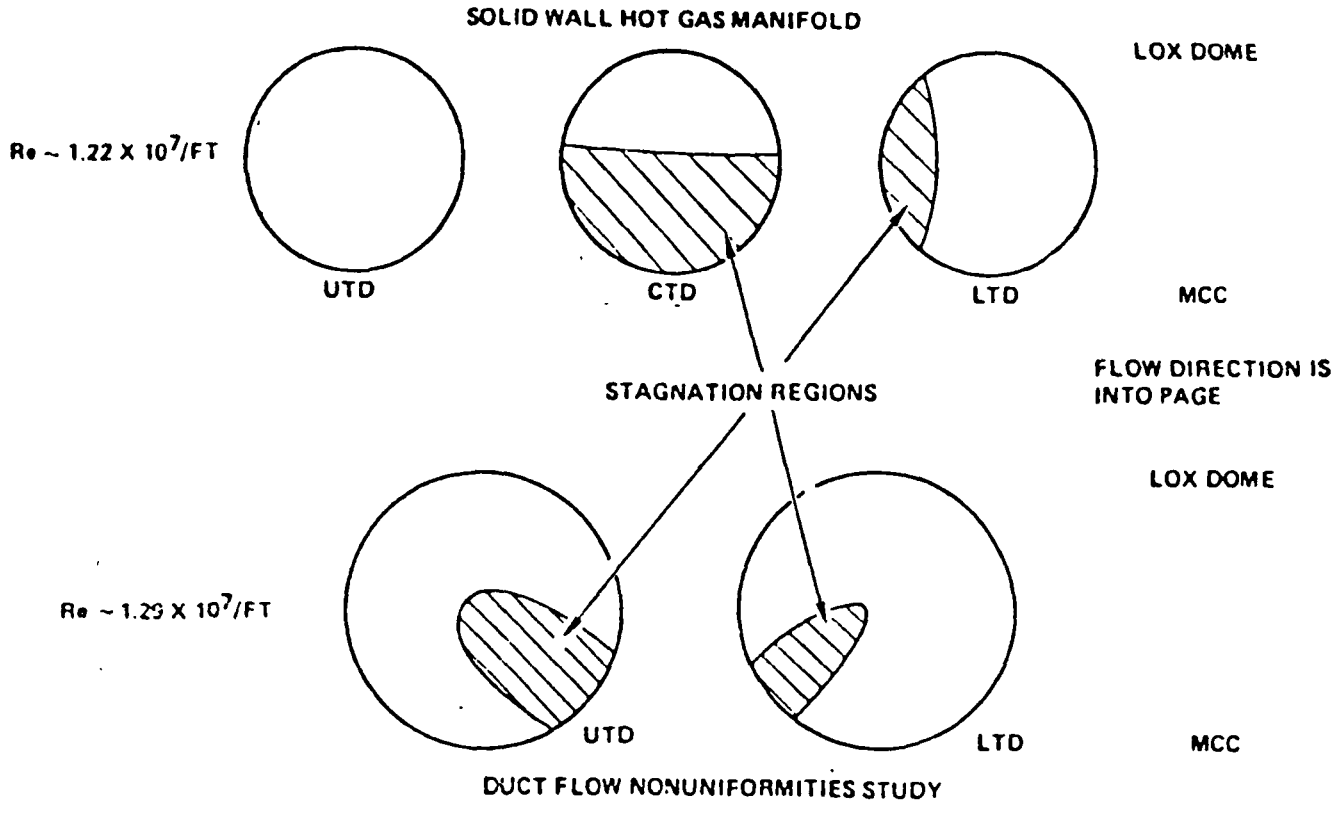

Fig. 12 Stagnation Region Comparison Between Two- and Three-Duct Configurations

comparable Reynolds numbers. Typical mass flow splits are 52 percent in the UTD and 48 percent in the LTD for the two-duct system, while the three-duct configuration exhibits typical mass splits of UTD: 52 percent, CTD: 9 percent, and LTD: 39 percent, where CTD is the center transfer duct. Typical Mach number profiles for the two- and three-duct hot gas manifold configuration scaled to engine RPL (100 percent) conditions are shown in Figs. 13 and 14, respectively. The maximum Mach number observed in the two-duct configurations is 0.16 while the three-duct HGM exhibited a maximum Mach number of 0.26.

It can be observed from the side view profiles (Fig. 14) that there is more flow in the upper portion of the ducts as expected because the flow has an upward bias after coming around the 180-deg turn. The contours of these vertical profiles are basically the same in both ducts. The top view shows

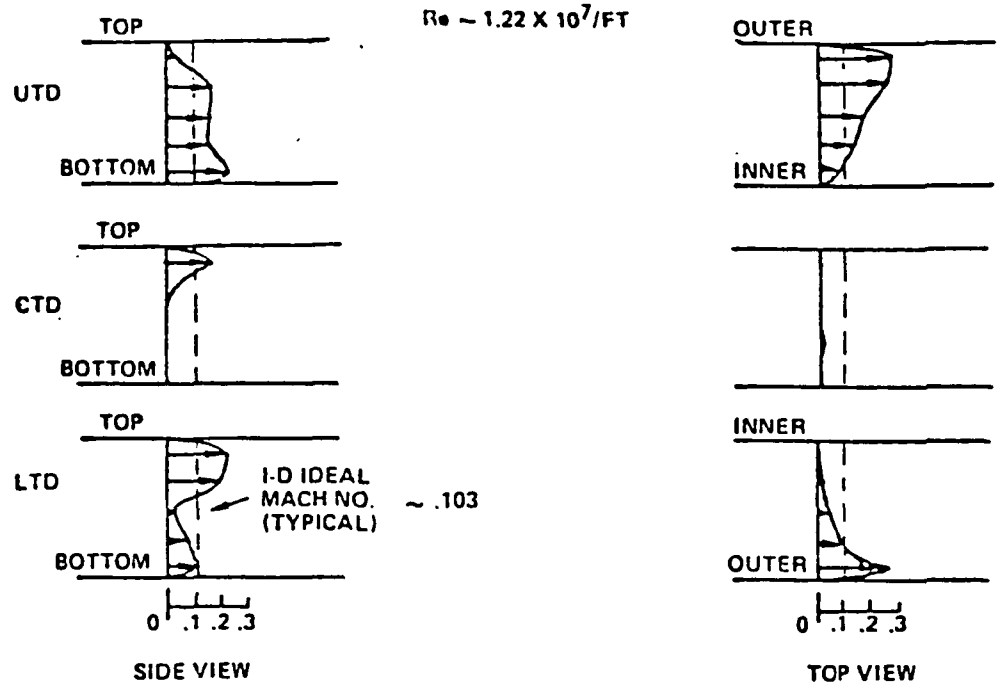

Fig. 13 Engine-Scaled Three-Duct Manifold Mach Number Profiles Along Duct Major Axes (100 Percent Power Level Condition)

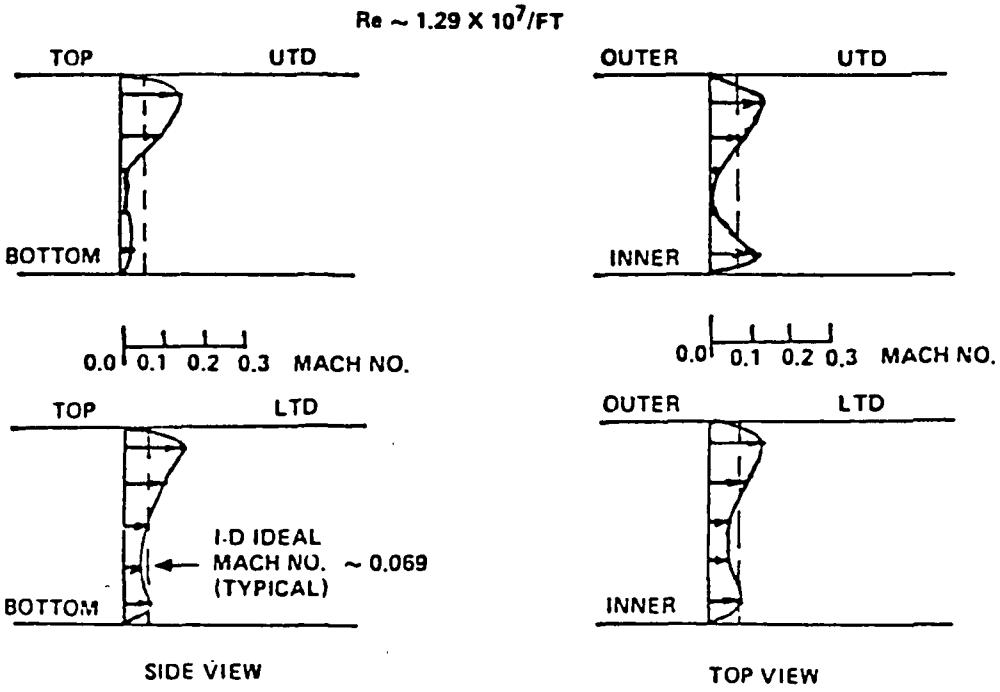

Fig. 14 Engine-Scaled Two-Duct Manifold Mach Number Profiles Along Duct Major Axes (100 Percent Power Level Condition)

that there is more flow on the outside of each duct. This is because flow travels circumferentially in both directions around the fishbowl where most of the flow enters the transfer ducts at the outside regions. Examination of the corresponding Mach number profiles associated with three-duct manifold displays that little appreciable flow passes through the center transfer duct. In addition, the flow is nonuniform within each duct and from one duct to another. This observation is true for both the vertical and horizontal axis. The two-duct HGM configuration Mach number profiles for both ducts approach the one-dimensional ideal Mach number condition (0.16). This ideal Mach number uniformity condition was only approached in the upper transfer duct in the present three-duct design. It should be noted that the one-dimensional constant Mach number profile across the transfer duct exit plane is the best flow condition achievable for a given mass flow and transfer duct cross-sectional area. The flow through the transfer duct exit plane, in the two-duct HGM configuration, is clearly more symmetrical and uniform than that associated with the current three-duct HGM design.

3. METHOD OF ANALYSIS

3.1 THE PAGE CODE

This study employed the PAGE code which evolved from the General Interpolants Method (GIM) for constructing numerical analogs of the partial differential equations governing fluid flow (Refs. 5 and 6). The formulation considers the flow to be unsteady, viscous, heat conducting, and compressible. Steady flow is treated as the asymptotic limit of the unsteady case. Viscous effects are treated as either laminar flows or through algebraic turbulence models. Incompressible flows, or flows at low Mach numbers with almost no changes in density, are easily treated by use of artificial compressibility.

The partial differential equations solved are the time-averaged Navier-Stokes equations together with the equations for conservation of mass and energy. These equations, written in three-dimensional conservative form for a Cartesian coordinate system, are expressed as follows:

$$\frac{\partial U}{\partial t} + \frac{\partial E}{\partial x} + \frac{\partial F}{\partial y} + \frac{\partial G}{\partial z} = 0 \qquad (1)$$

where

$$U = (\rho,\ \rho u,\ \rho v,\ \rho w,\ \rho \mathcal{E}) \qquad (2)$$

is the solution vector of conserved variables, and E, F and G are the flux vectors. The set of equations is completed by providing transport properties and an equation of state relating pressure, density, and temperature.

Boundary conditions are required to obtain a unique solution to the above set of equations, the specific form of the boundary conditions

obviously being dependent on the problem. Generally, configurations with a definable mass flux are assumed to have a set of specified "inflow" conditions at some point upstream of the domain of interest. Subsonic flows require the static pressure to be specified in some form as a downstream or exit condition. The no-slip condition is imposed along all solid walls. Thermal boundary conditions consist of either constant wall temperature or adiabatic wall conditions. For elliptic problems, the integration commences at time t = 0 with all variables initiated over the entire domain of interest. After each time step, the flux vectors are recalculated after evaluating the primitive variables via a decoding procedure. The solution proceeds for a specified time or until a steady state condition is reached.

The geometric treatment uses concepts from finite element theory to obtain discrete models of the conservation equations in arbitrary geometric domains. Complex domains can be subdivided into a number of smaller regions, the edges and surfaces of which can be described by analytic functions. Intrinsic curvilinear coordinate systems can be produced by a univalent mapping of a unit cube onto any simply connected bounded subdomain. Any complex region can then be transformed piecewise and assembled using blending function interpolation. While the local intrinsic coordinates are designated η_1, η_2, and η_3, the shape of the geometry is completely defined by eight corner point functions P_i, twelve edge functions, E_i, and six surface functions, S_i. Based on previous work by Gordon and Hall (Ref. 7), a general relationship between physical and local, intrinsic, coordinates has been developed in the form of a general trilinear interpolant function:

$$X(\eta_j) = \sum_{i=1}^{12} f_{E,i}(\eta_j)\, E_i + \sum_{i=1}^{8} f_{P,i}(\eta_j)\, P_i + \sum_{i=1}^{6} f_{S,i}(\eta_j)\, S_i \qquad (3)$$

where $X(\eta_j)$ denotes the Cartesian coordinate vector (x,y,z) as a function of intrinsic coordinates η_1, η_2, η_3, and $f_{P,i}$, $f_{E,i}$ and $f_{S,i}$ are respectively, known trilinear, bilinear and linear functions of the intrinsic coordinates η_1, η_2 and η_3. With this transformation, any point with intrinsic coordinates η_j can be related to global Cartesian coordinates x,y,z.

A grid of discrete nodal points is generated using this concept of multivariate blending function interpolation. Virtually any stretching function can be accommodated to concentrate nodes near walls, large gradient regions, etc. In addition, the edges of the local hexahedrals can be segmented, thereby allowing another means of grid spacing control.

Discrete analogs of the conservation equations are derived by employing the Method of Weighted Residuals (MWR). The procedure followed here differs from the classical one in several ways: the weight functions are not necessarily equal to the shape functions; the conserved variables U and the respective flux terms E,F, and G rather than the primitive variables, are approximated over an element. Assuming the shape functions to be multilinear interpolants, written in intrinsic coordinates, the value of any function Q at any point within the element can be expressed in terms of the values of the function at the corner nodal points as

$$Q(\eta_j) = \sum_{i=1}^{8} S_i(\eta_j)\, Q_i \tag{4}$$

where the shape function S_i is formally identical to $f_{p,i}$ as defined in Eq. (3). Derivatives with respect to physical coordinates x_j are then easily evaluated from

$$\frac{\partial Q}{\partial x_j} = [J]^{-1} \frac{\partial Q}{\partial \eta_j} \tag{5}$$

where [J] is the Jacobian of the transformation obtained by differentiating Eq.(3).

Having defined the variables over each element we proceed to produce a discrete analog of the governing equations for each element using the Method of Weighted Residuals. Accordingly,

$$\int_V W \mathcal{D}\, dV = 0 \tag{6}$$

where W is an arbitrary weight function, and $\mathcal{D}$ represents the differential equation, Eq. (1). Utilizing Eqs. (4) and (5) to derive a detailed expression for the differential equation $\mathcal{D}$, and substituting into Eq. (6), we arrive at the discrete analog for each element

$$I_e = A^e_{ij}\, \dot{U}_j + B^e_{ij}\, E_j + C^e_{ij} F_j + D^e_{ij}\, G_j \tag{7}$$

where $\dot{U}_j$, E_j, F_j, G_j now are evaluated at the element node points, and the geometry dependent element coefficient matrices are given by

$$A^e_{ij} = \int_e W_i\, S_i\, \frac{\partial(x,y,z)}{\partial(\eta_1,\eta_2,\eta_3)}\, d^3\eta \tag{8a}$$

$$B^e_{ij} = \int_e W_i\, \frac{\partial(S_j,y,z)}{\partial(\eta_1,\eta_2,\eta_3)}\, d^3\eta \tag{8b}$$

$$C^e_{ij} = \int_e W_i\, \frac{\partial(x,S_j,z)}{\partial(\eta_1,\eta_2,\eta_3)}\, d^3\eta \tag{8c}$$

$$D^e_{ij} = \int_e W_i \frac{\partial(x,y,S_j)}{\partial(\eta_1,\eta_2,\eta_3)} d^3\eta \qquad (8d)$$

After all elements are so processed, the coefficients are assembled at all node points which are connected to each other. This assembly is characteristic of finite element procedures and consists of a weighted Boolean sum over the eight elements surrounding each node.

The assembled equation becomes

$$A_{NM}\dot{U}_M + B_{NM}E_M + C_{NM}F_M + D_{NM}G_M = 0 \qquad (9)$$

where

$$A_{NM} = \sum_{e=1}^{8} \alpha_e A^e_{ij} \qquad (10)$$

and similar expressions are obtained for the B, C, and D matrices. The α_e are a set of arbitrary element influence coefficients which are used to select a specific difference scheme.

At this point the weight functions W are arbitary, and therefore, Eq. (9) is generally implicit in the time derivative term $\dot{U}$. It can be shown that, if the weight functions are selected to be equal to the shape functions, Eq. (9) represents a classical Galerkin finite element model. Any other choice for the weight functions will result in what is now called a Petrov-Galerkin method. Choosing weight functions which are orthogonal to the shape functions results in a scheme which is explicit in the time derivative $\dot{U}$ and thus represents finite difference schemes. In practice such schemes have the advantage that a great wealth of experience exists concerning their behavior during numerical integration.

The general form of the weight functions is

$$W_i * \Delta_J = \alpha_i (a_i - \eta_1)(b_i - \eta_2)(c_i - \eta_3) \qquad i = 1,\ldots, 8 \qquad (11)$$

where Δ_J is the determinant of the Jacobian matrix [J]. Since the weight functions are orthogonal to the shape functions, the A(mass) matrix becomes diagonal, which results in explicit, uncoupled time derivatives. However, the resulting element integrals, Eq. (8), must be evaluated by quadrature.

With the goal of refining the general interpolants method a new set of orthogonal tricubic weight functions has recently been derived by Stalnaker (Ref. 8), viz.

$$W_i = a_i \left(\sum_{k=0}^{3} b_k \eta_1^k\right) \left(\sum_{k=0}^{3} c_k \eta_2^k\right) \left(\sum_{k=0}^{3} d_k \eta_3^k\right) \qquad (12)$$

The principal advantage of these weight functions is that they allow the element matrix integrals to be evaluated analytically. Analytical evaluation introduces less numerical "noise" into the calculation than Gaussian quadrature, and it allows a progressive assembly of generalized elements (PAGE) to be used resulting in large savings of computer storage by not having to store matrix coefficients in memory. Furthermore, progressive assembly of the full domain matrices lends itself to vectorization and thus efficient use of modern supercomputers.

3.2 GEOMETRY AND GRID CONSTRUCTION

The definition of all baseline configurations to be modeled was obtained from drawings supplied by NASA-MSFC and/or Rocketdyne. Relevant dimensions were extracted from these drawings and are given in Figs. 15 and 16. The schematic sketches given in these figures completely define the flow boundaries for the turnaround duct and the fishbowl (Fig. 15), and the positioning of the transfer ducts relative to the fishbowl (Fig. 16). The transfer ducts were terminated at the position of the transfer duct exit pitot probe rakes (13.315 inches from point B along the axis given by BA in Fig. 16).

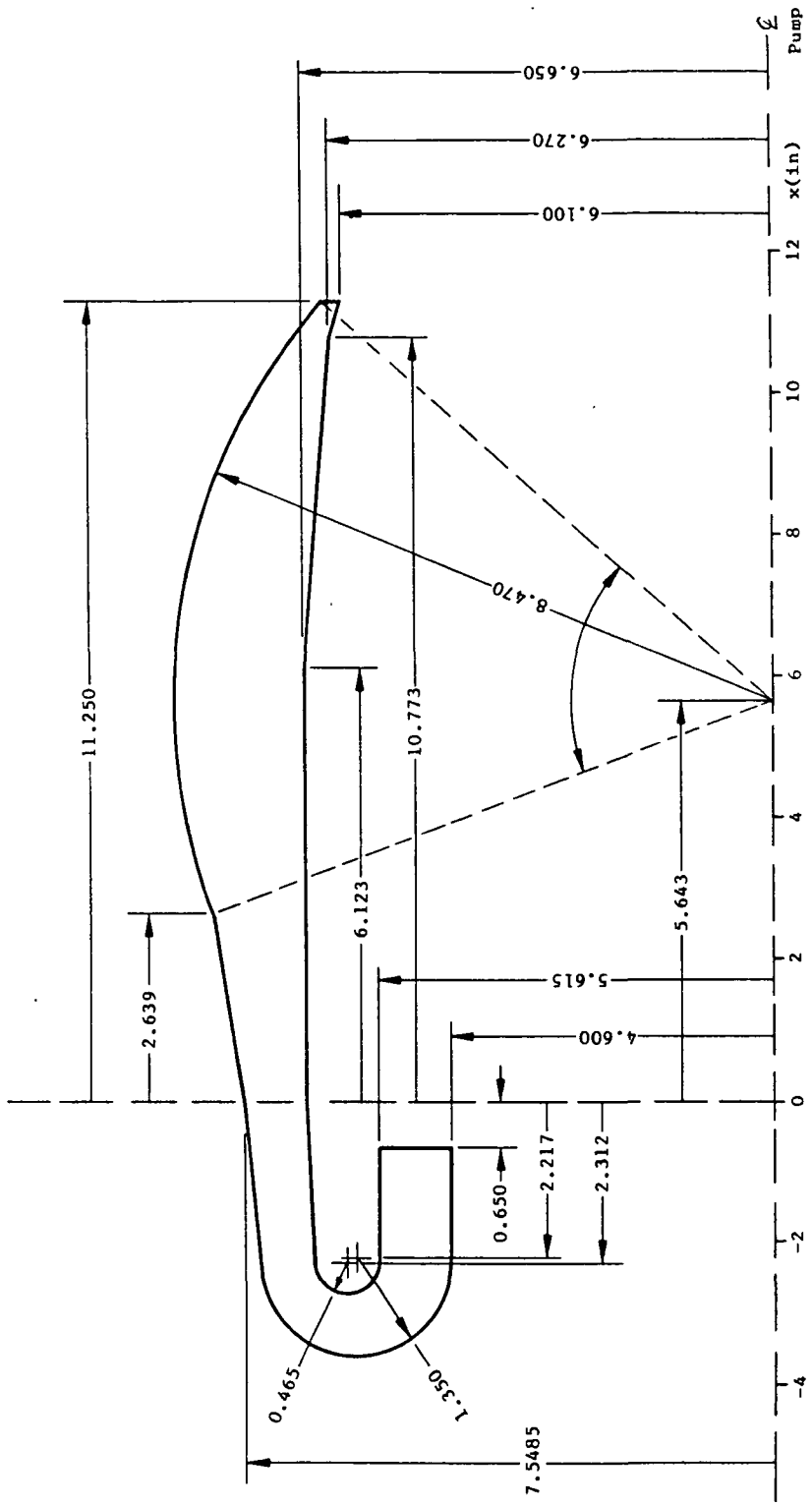

Fig. 15 DFNUS Hot Gas Manifold Turnaround Duct and Bowl Cross-Section Definition

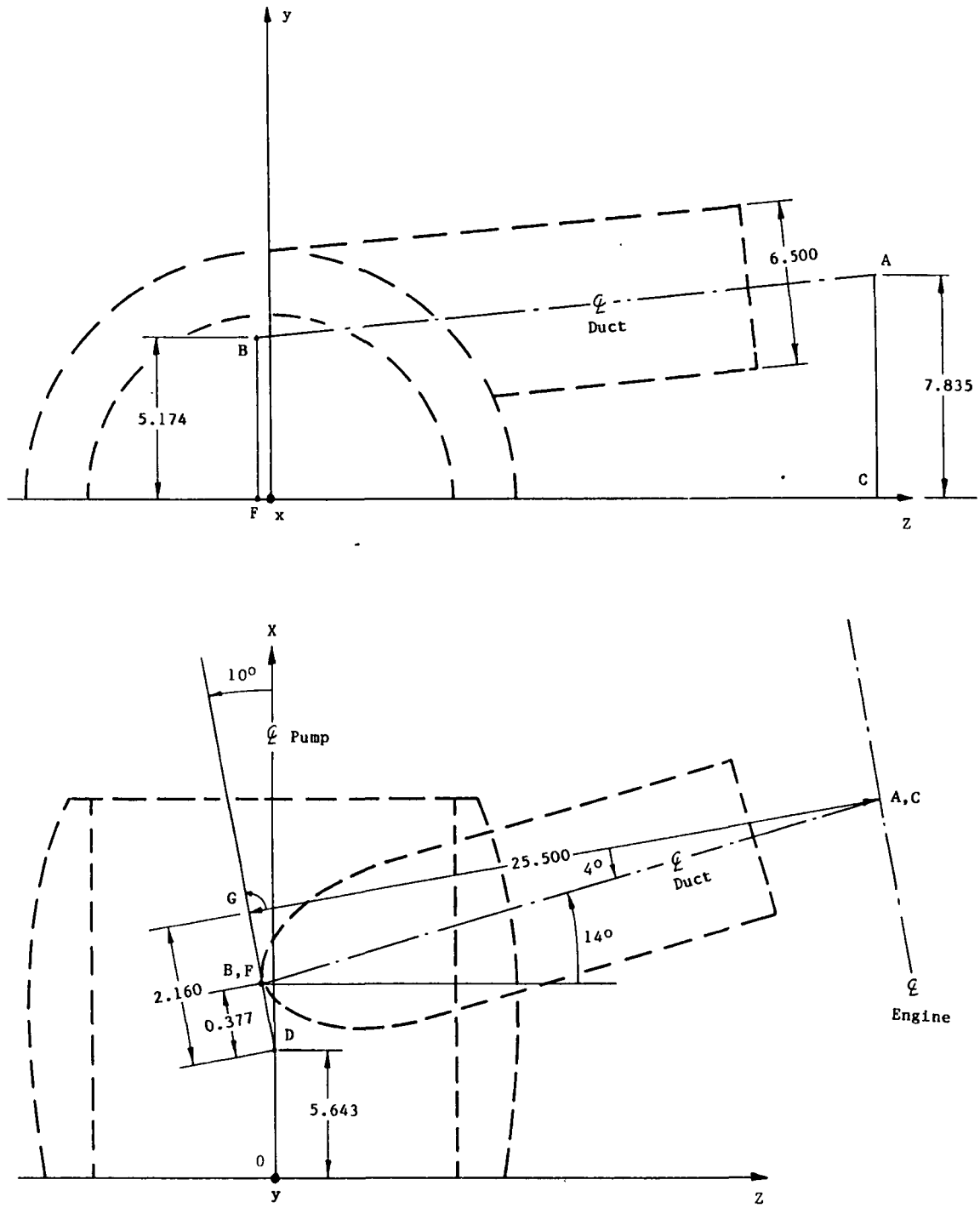

Fig. 16 Definition of Transfer Duct Location Relative to Hot Gas Manifold Bowl

Construction of the grid (as well as subsequent flowfield calculation) was performed in several phases:

I Fishbowl and Transfer Ducts

II Turnaround Duct

III Combination of Turnaround Duct, Fishbowl and Transfer Ducts.

In all cases, the configuration geometry was assumed to be symmetric with respect to a plane containing the HGM pump axis and a fishbowl meridional cut between the two transfer ducts. Struts and guide vanes were neglected in the computational model. While the actual flow field is truly three-dimensional due to the swirl imposed on the flow exiting the turbine simulator, neglection of the swirl in the analysis made it possible to perform the flowfield analysis using only a half-geometry.

Geometrical detail and truth of the model (i.e., nodal density and contour detail) is dictated by a compromise between what is needed for reasons of computational stability and desired flowfield detail on the one hand, and what one can afford financially on the other hand. Note that computational cost is directly proportional to nodal density.

3.2.1 Fishbowl and Transfer Ducts

The Phase I HGM Bowl and Transfer Duct Half-Model was set up using a total of 6798 nodes. Oblique (sparse grid) views of the complete bowl inner wall, outer wall plus transfer duct as well as a composite view are given in Figs. 17 through 19. The inner wall consists of a circular cylinder followed by a cone frustum with another cone frustum of larger included angle at the end. The HGM spherical bowl outer wall is shown in the next illustration. Since the standard geometry module of the PAGE code only permits simply connected surfaces to be modeled, extensive code refinements were required to model the spherical bowl circular cylinder transfer duct intersection. Note that the duct inlet edges are slightly rounded, which was achieved by input of an appropriate mathematical function rather than by tabulated data. An unwrapped view of the fishbowl grid is shown in Fig. 20.

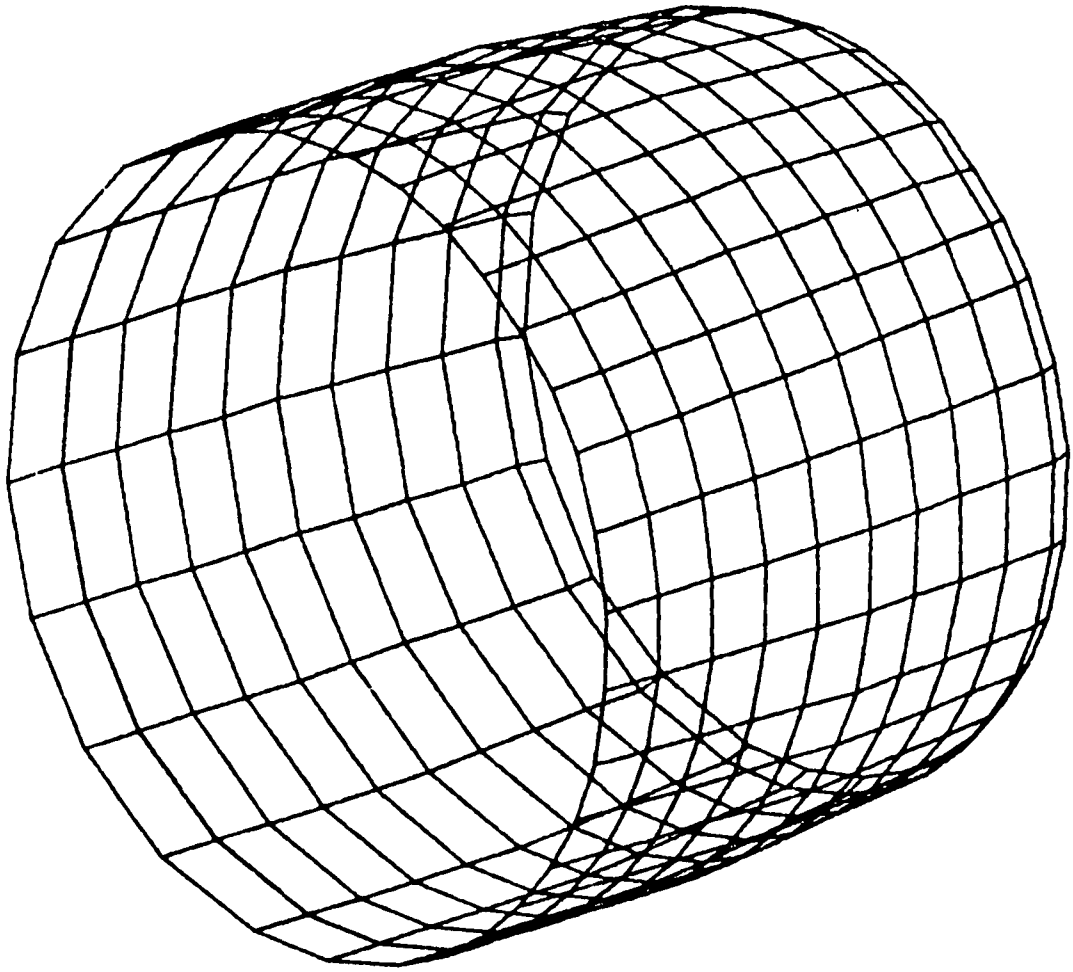

Fig. 17 Hot-Gas Manifold Bowl Inside Wall Sparse Grid

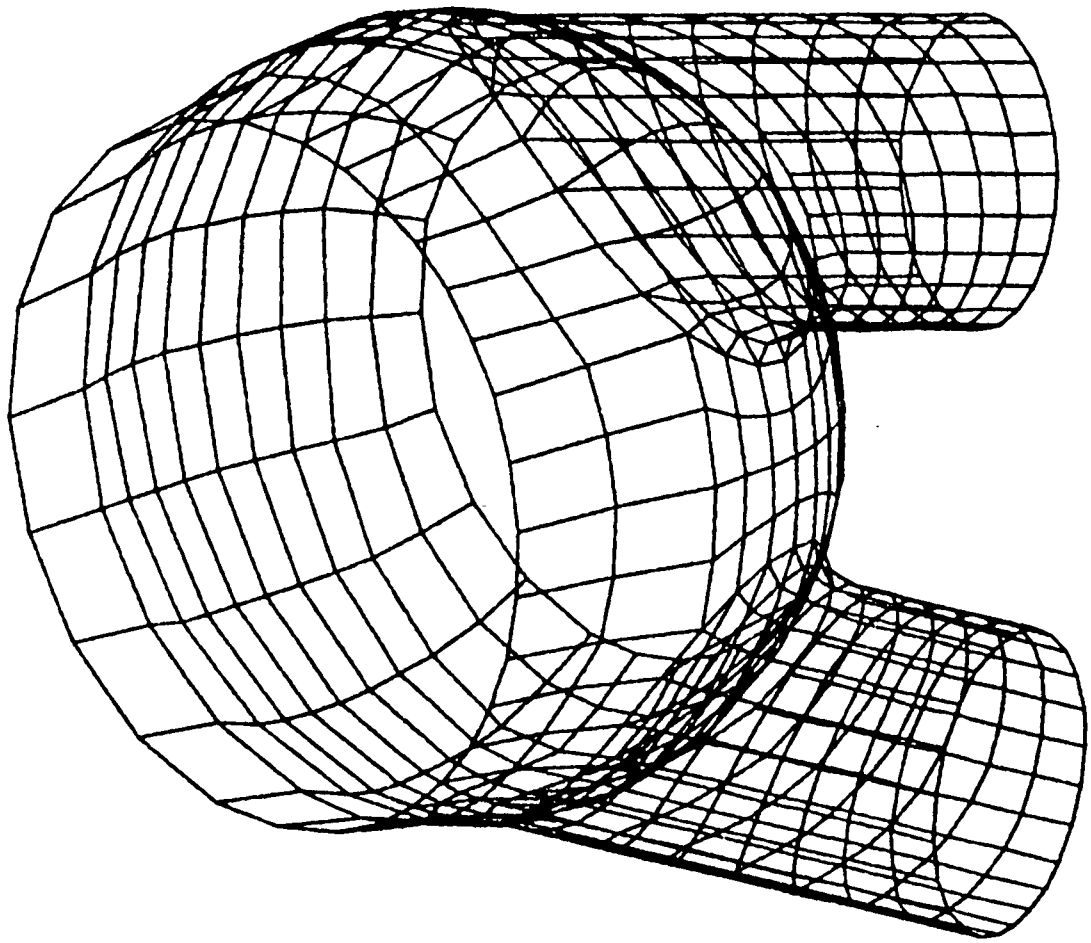

Fig. 18 Hot-Gas Manifold Bowl Outside Wall Sparse Grid

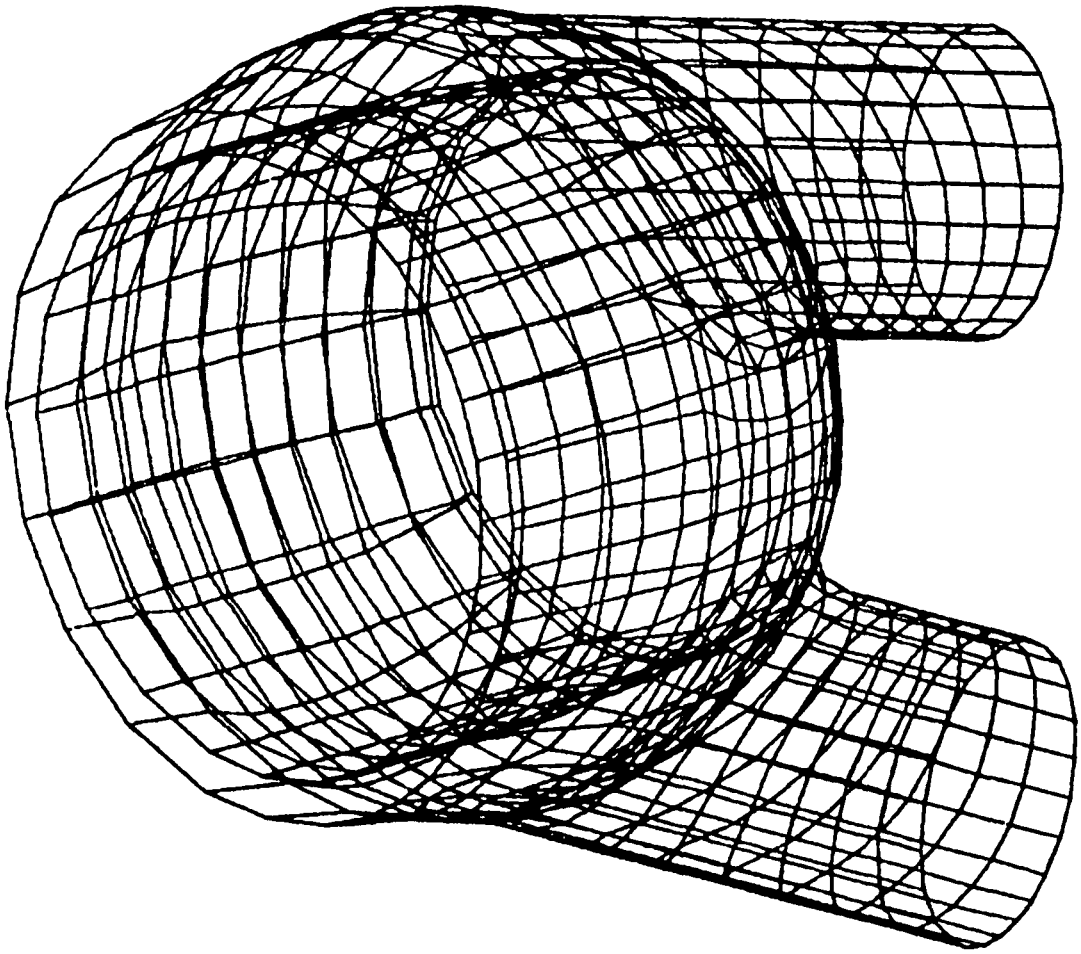

Fig. 19 Hot Gas Manifold Composite Grid

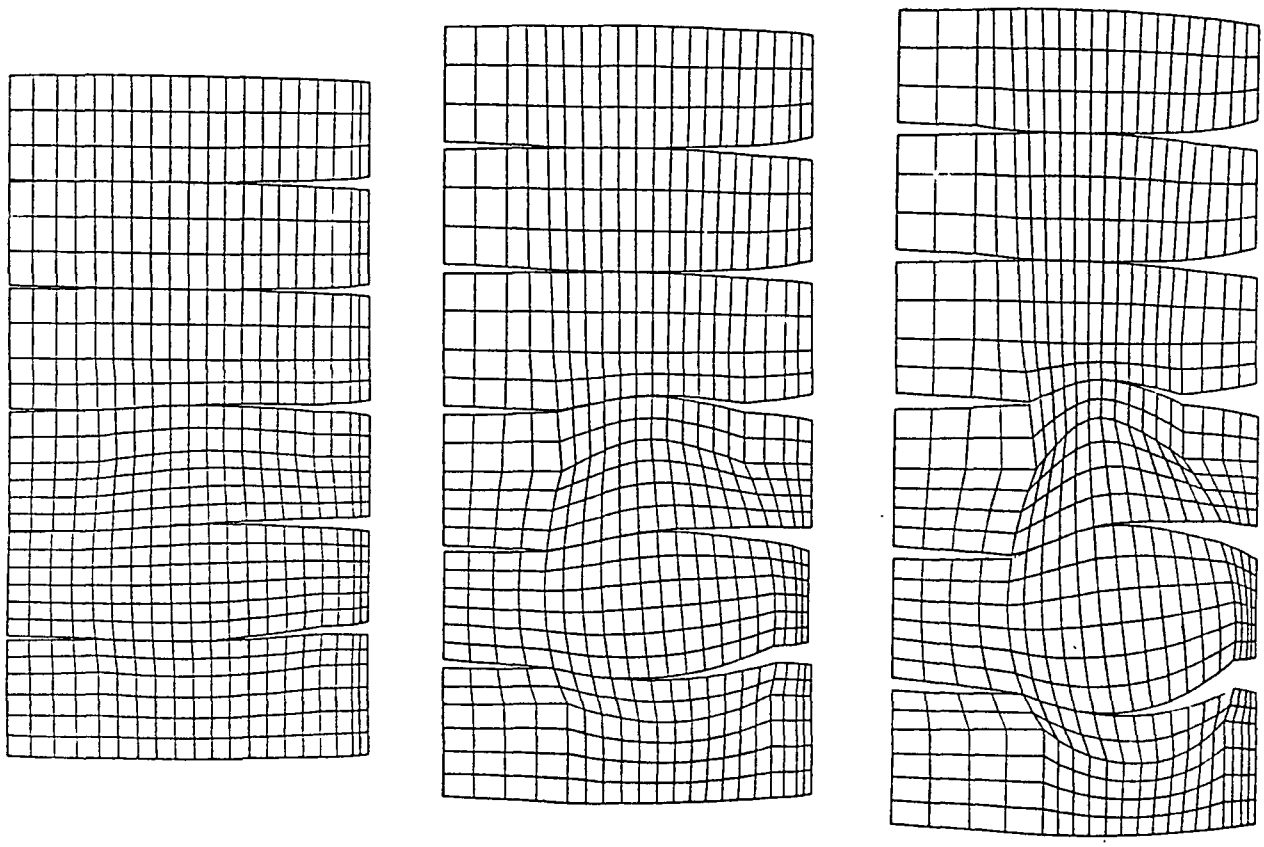

Fig. 20 Hot-Gas Manifold Bowl Grid (Unwrapped Inside, Center, Outside Surface)

Considerable effort was expended to construct the grid network keeping economy of the calculations in mind. By this we mean using a relatively coarse grid in regions where relatively small gradients are expected, with an orderly transition to a higher nodal density for regions with rapid changes in the flow properties. Given the constraints of the formulation of the geometry module of the PAGE code it is extremely difficult to satisfy all requirements simultaneously. Stability problems were expected and encountered, particularly at the top end of the bowl where inner and outer wall converge, and in the region of the transfer duct inlet, where highly distorted (skewed) elements could not be avoided entirely, particularly on the outside where the transfer duct wall joins the bowl contour almost tangentially, as shown in Fig. 21.

For reasons which will become clear after discussing the flowfield results, a second version of the HGM was investigated. This second version incorporates a modified transfer duct inlet geometry. Specifically, a much larger radius of curvature of the duct inlet contour in the lower inner duct quadrant was provided with the goal of preventing flow separation in this region. The modified geometry is illustrated and compared to the nominal geometry in Figs. 21 and 22. Again, the modified duct inlet geometry was implemented using functional input rather than tabulated data. Overall views of the outer wall and the assembled HGM (sparse) grid are shown in Figs. 23 and 24, respectively. No changes were made to the dimensions of the fishbowl and the transfer duct and its position relative to the fish bowl as specified in Figs. 15 and 16.

The next step (Phase II) of the geometry effort was to establish a grid structure for the turnaround duct using the dimensions given in Fig. 15. Grid structures were set up first for an axisymmetric configuration to be used in conjunction with the testing of certain inlet and exit boundary conditions to be discussed later. A typical cross-section using 270 nodes is shown in Fig. 25.

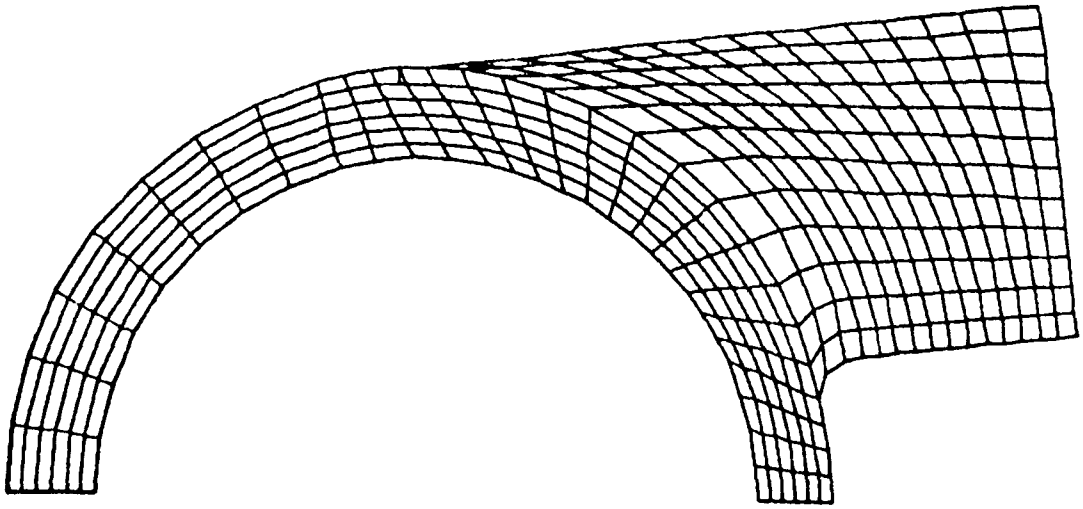

a. Nominal Configuration

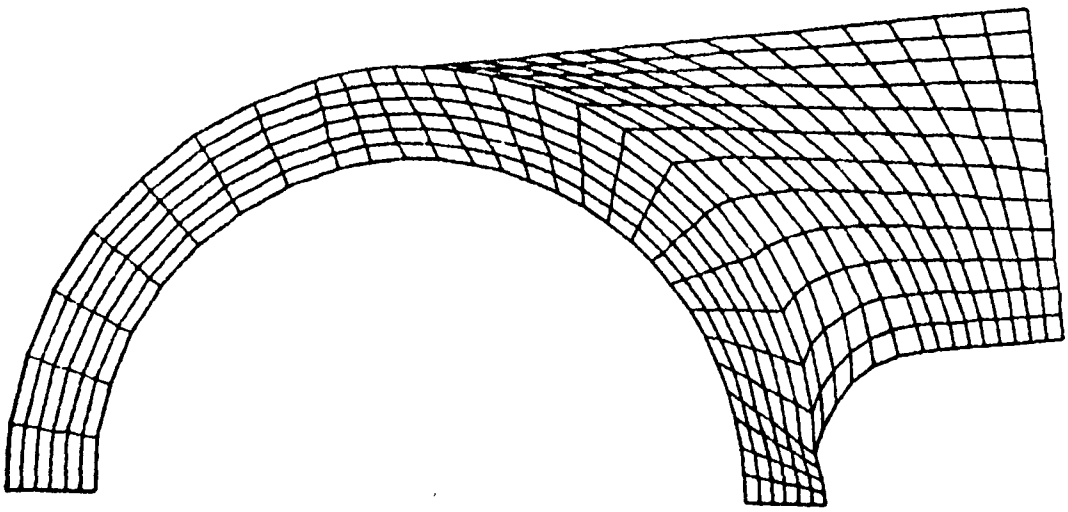

b. Modified Configuration

Fig. 21 Hot-Gas Manifold Bowl Cross-Section Grid

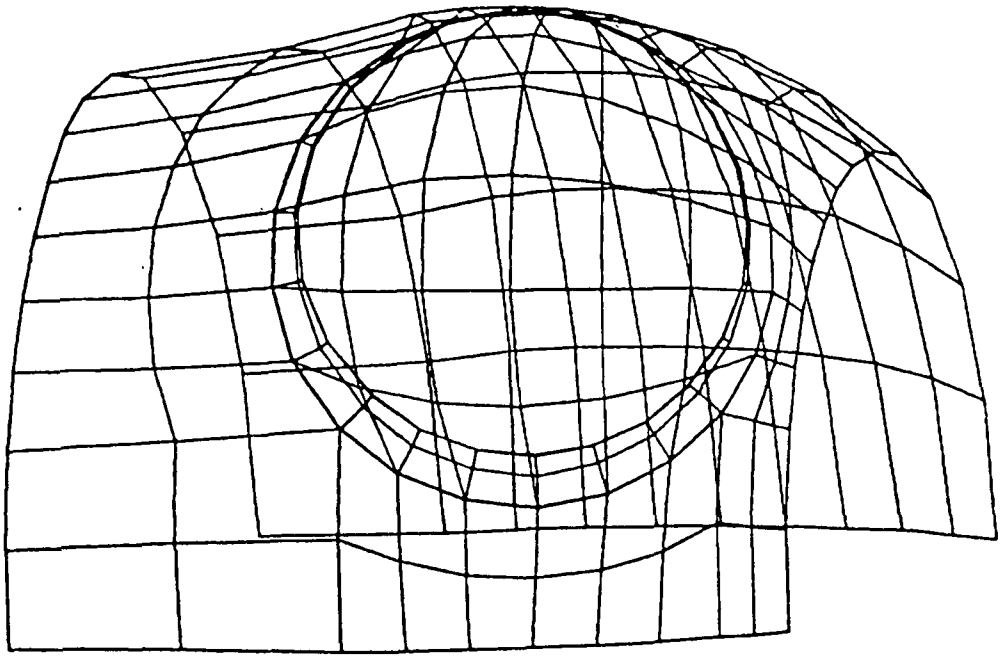

a. Nominal Configuration

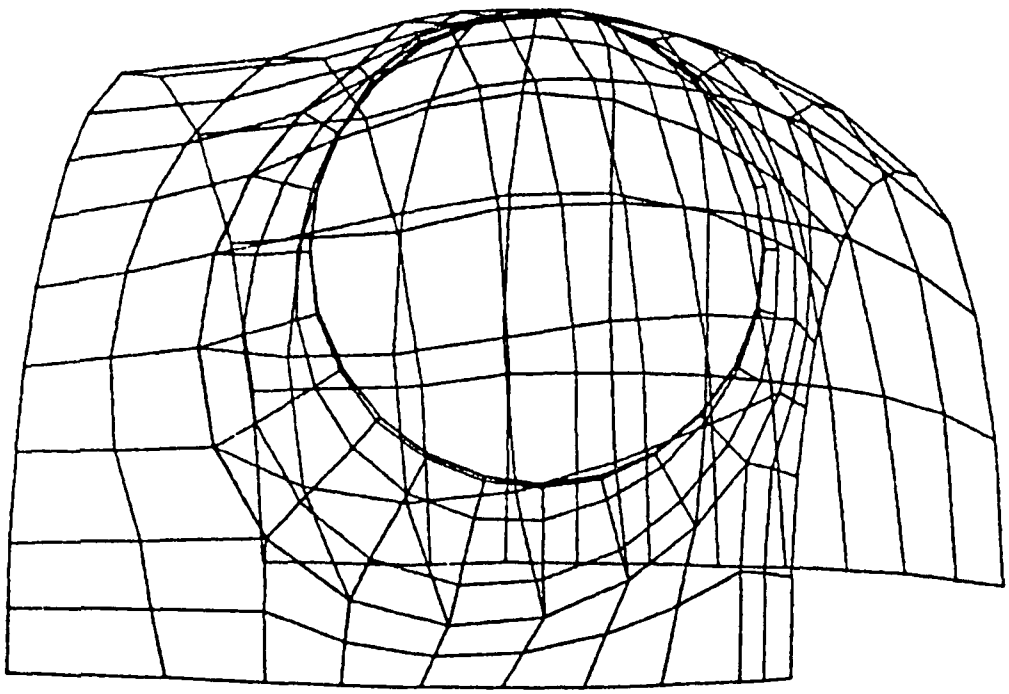

b. Modified Configuration

Fig. 22 Hot-Gas Manifold Grid, View Along Transfer Duct Axis

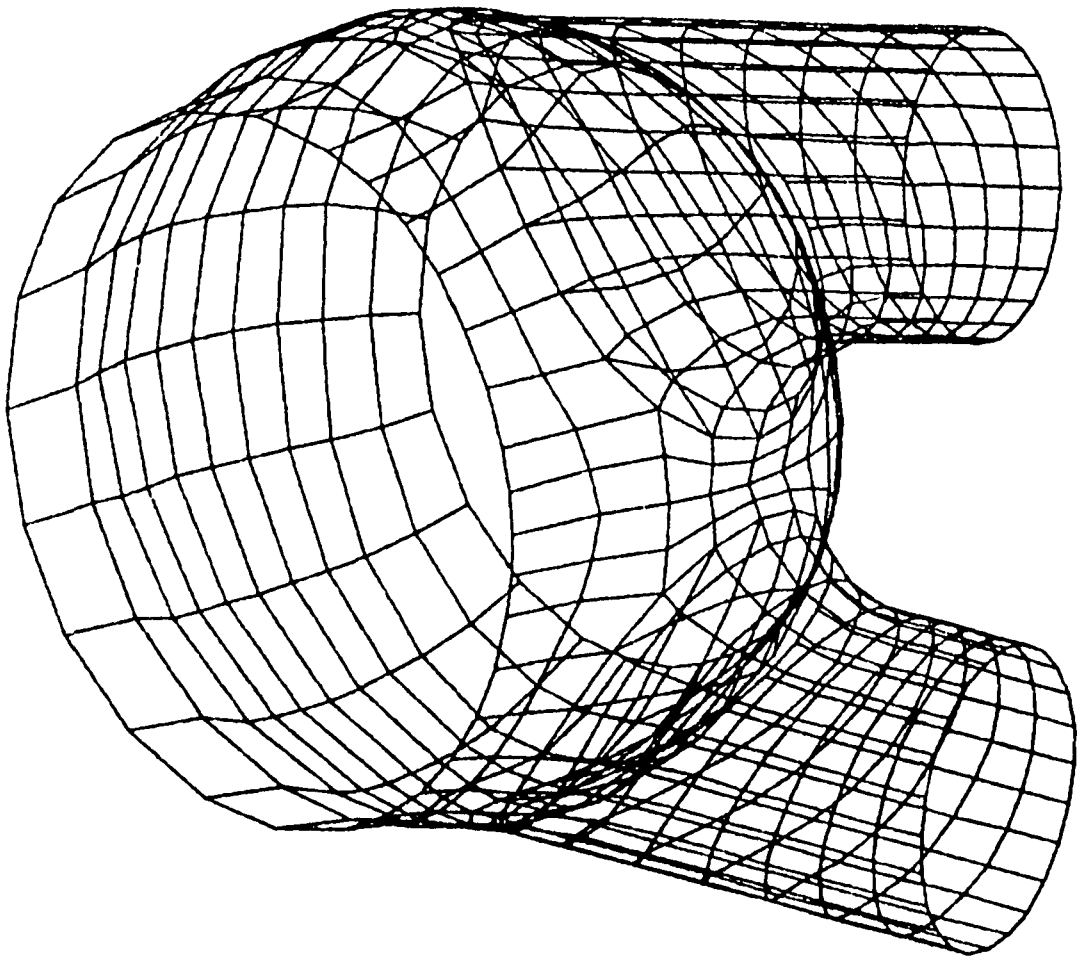

Fig. 23 Modified HGM Bowl Outside Wall Sparse Grid

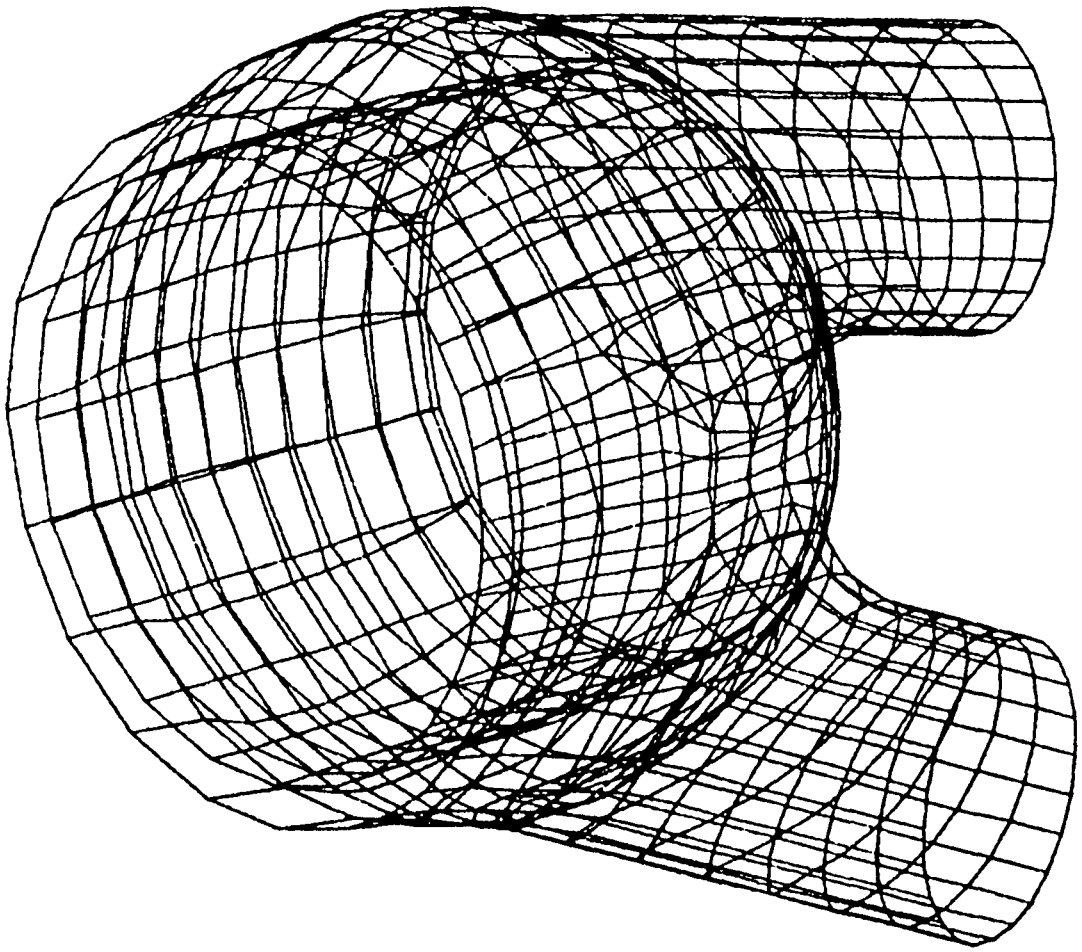

Fig. 24 Modified HGM Composite Grid

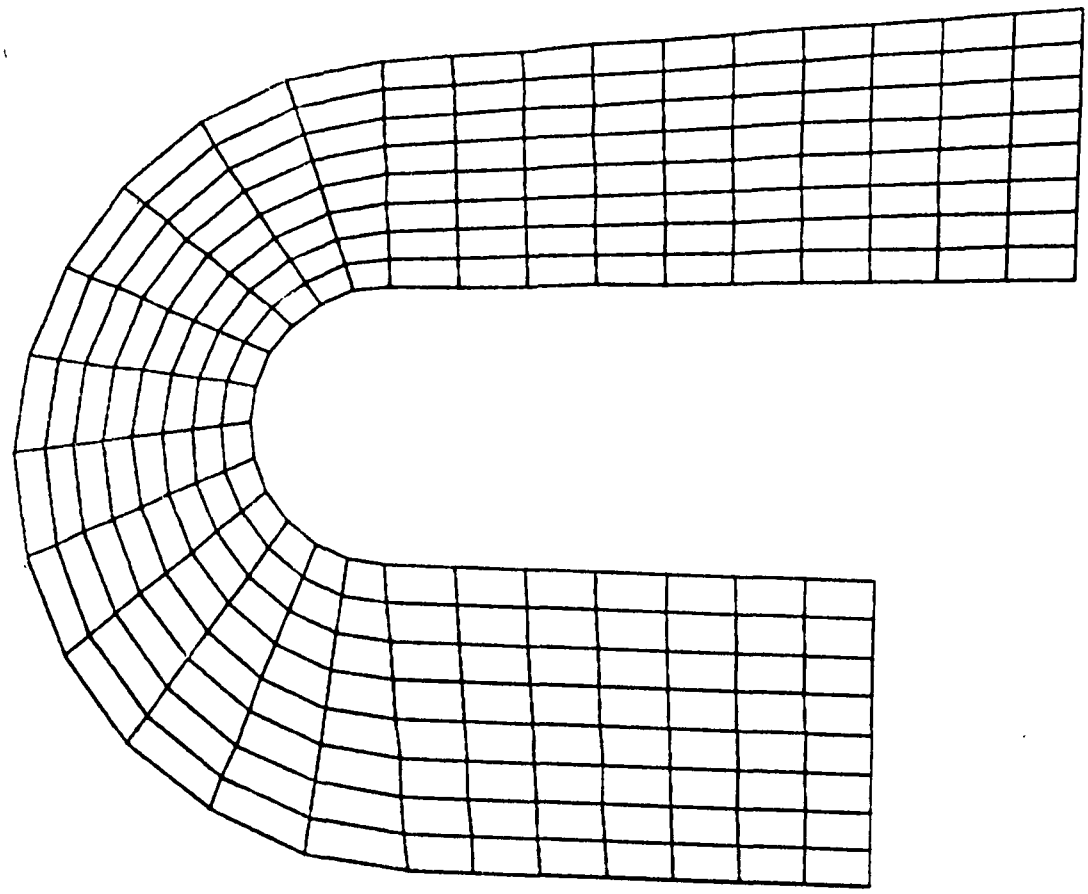

Fig. 25 Nominal Turnaround Duct Cross-Section Grid

Having accomplished this, the grid structure for a three-dimensional turnaround duct was set up to be matched to the fishbowl at x = 0 (turnaround duct - fuel bowl interface, see Fig. 15). Various oblique views of this three-dimensional turnaround duct are given in Figs. 26 through 28.

In Phase III of the geometry effort the turnaround duct grid was joined to that of the fishbowl - transfer duct to form a 14703 node assembled grid structure for the complete DFNUS hot-gas manifold from the turbine exit to the transfer duct exit. The inner wall of the turnaround duct and fuel bowl is displayed in Fig. 29, while Fig. 30 shows the outer wall of the complete HGM. A typical flow channel through turnaround duct and fuel bowl is shown in Fig. 31.

3.3 FLOWFIELD INITIALIZATION

Integration of the governing equations in time requires initial values in the spatial domain for all nodal points. The large number of nodes to be evaluated in these problems requires a sizable amount of computer time, and the cost of integration can be minimized by providing an initialization which is as close as possible to the solution of the flow field. A systematic initialization procedure for all nodes was implemented by utilizing the interpolative capability already built into the geometry module.

Variables which must be initialized include the density, the three velocity components and the pressure. For a perfect gas, the temperature is then determined from the equation of state. In the case of the SSME fuel turbo pump HGM we are dealing with nearly incompressible flow (Mach number $\leq$ 0.3). Under these circumstances, temperature changes are expected to be minimal and we therefore assumed the flow to be isothermal. The initialization is greatly helped by some knowledge of the flow field to be calculated, either by intuition or by examining measured data and flow visualization results. The initialization is implemented in two steps as follows.

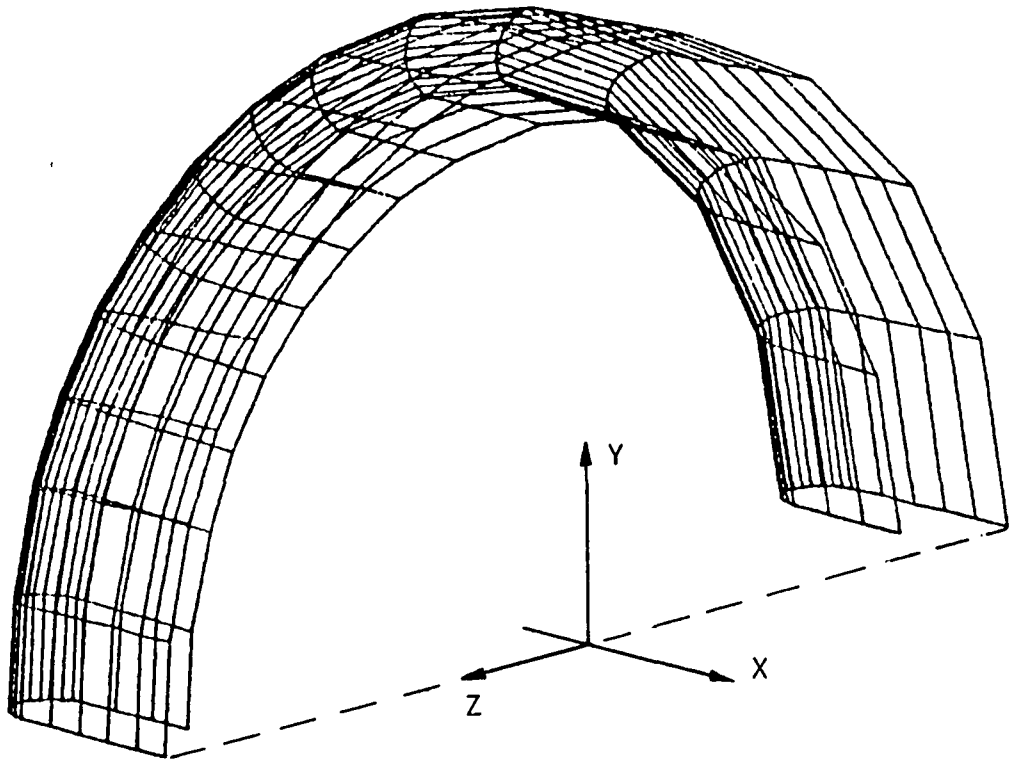

Fig. 26 Nominal Turnaround Duct Inside Wall Grid

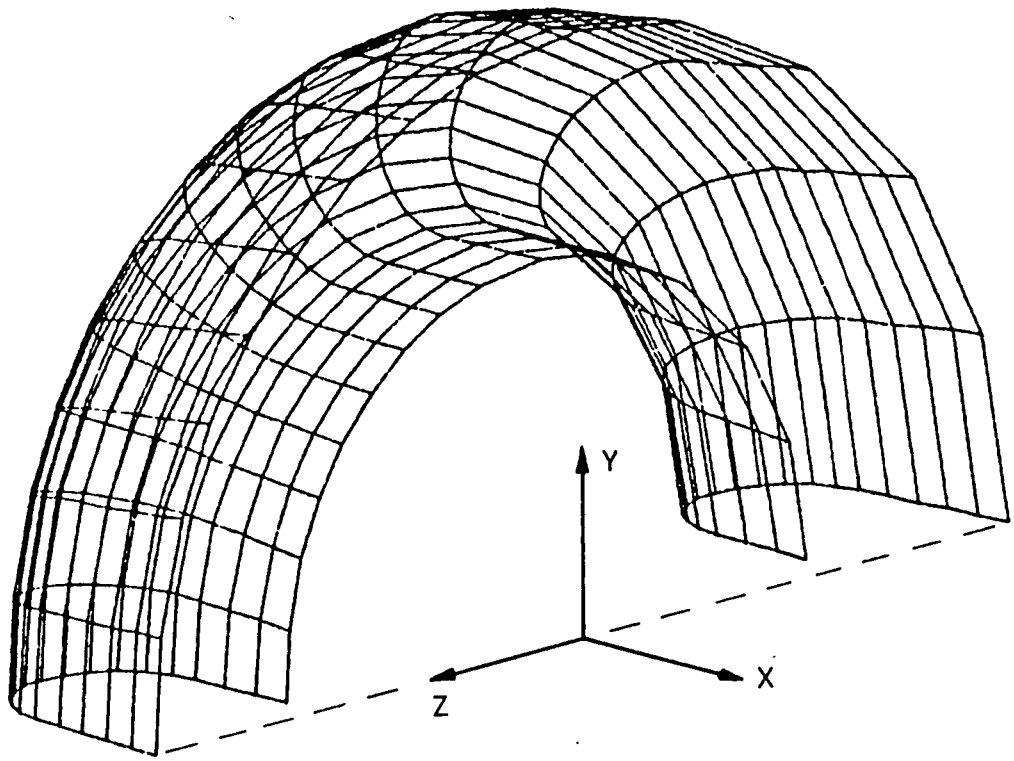

Fig. 27 Nominal Turnaround Duct Outside Wall Grid

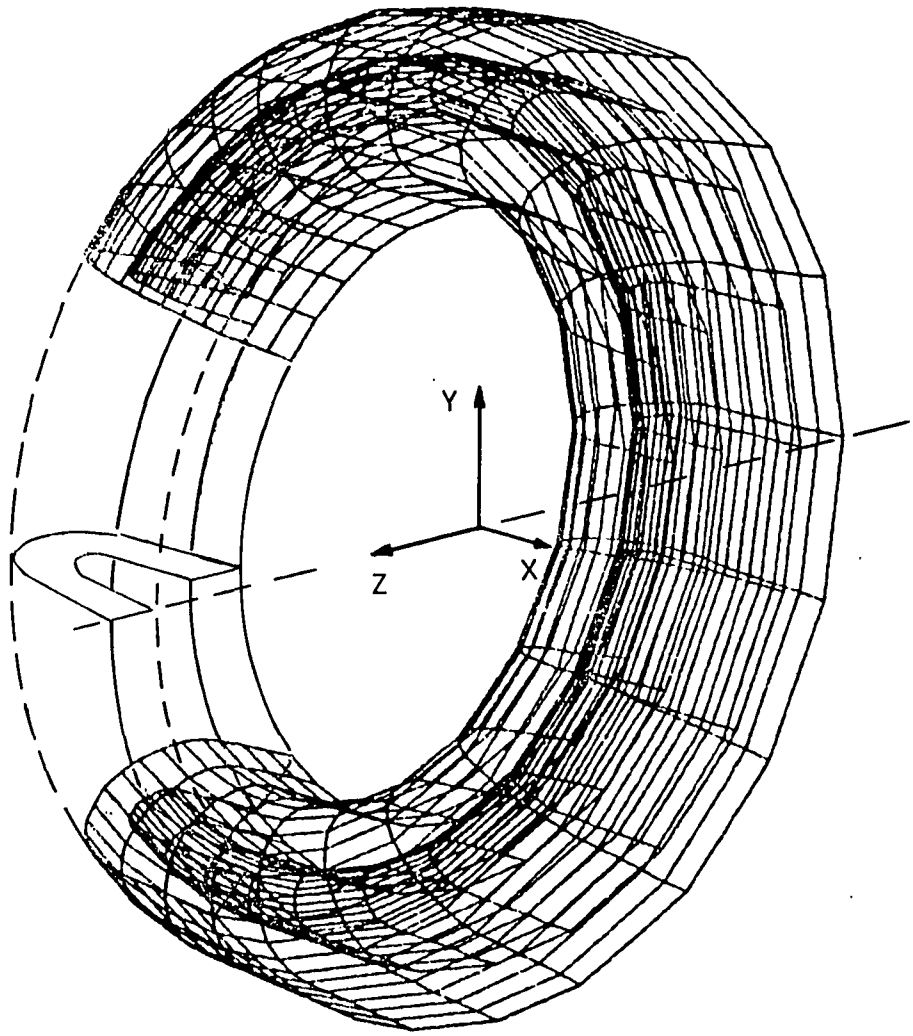

Fig. 28 Nominal Turnaround Duct Composite Grid

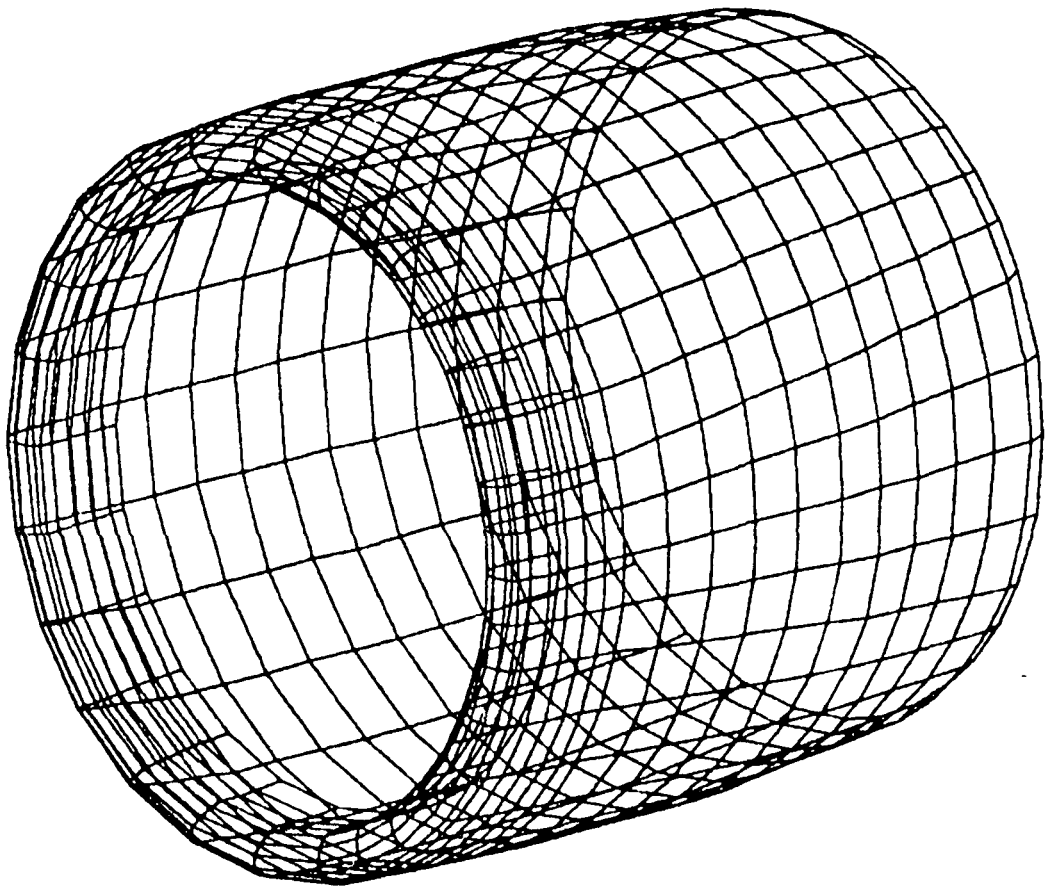

Fig. 29 Nominal Inside Wall Grid

ORIGINAL PAGE IS
OF POOR QUALITY

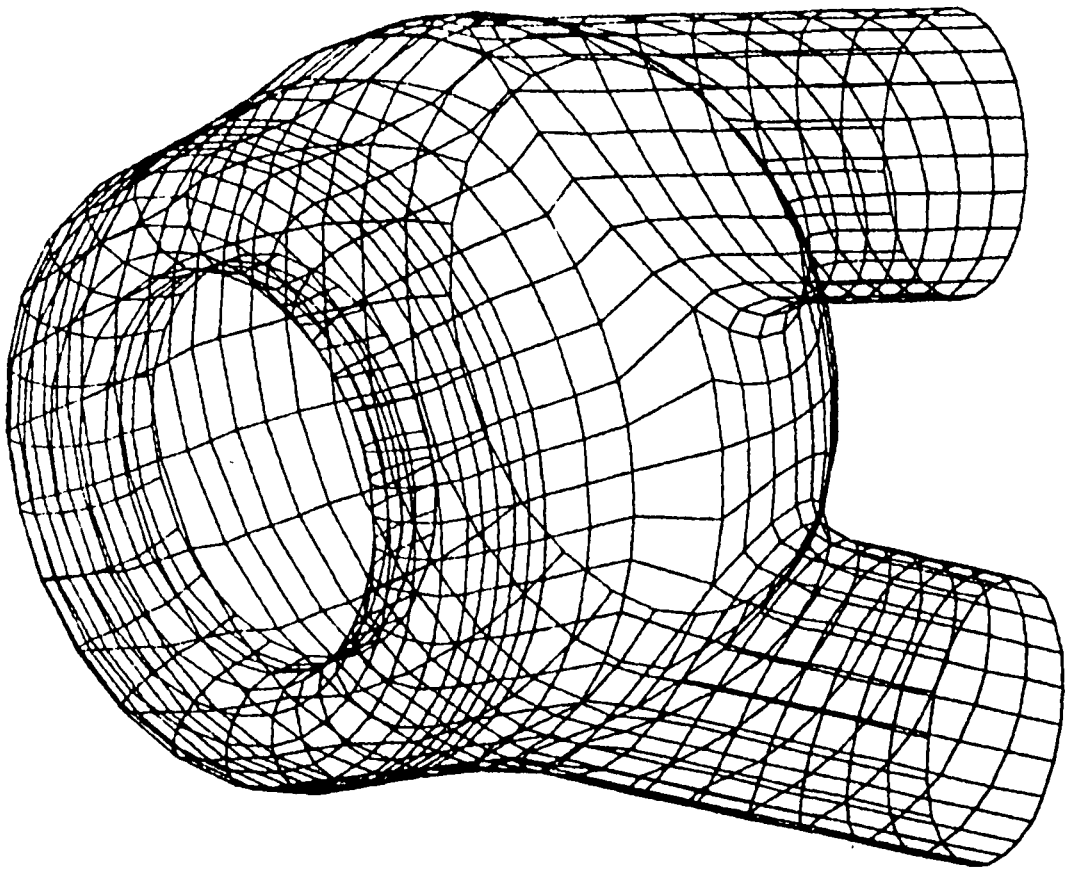

Fig. 30 DFNUS HGM Nominal Outside Wall Grid

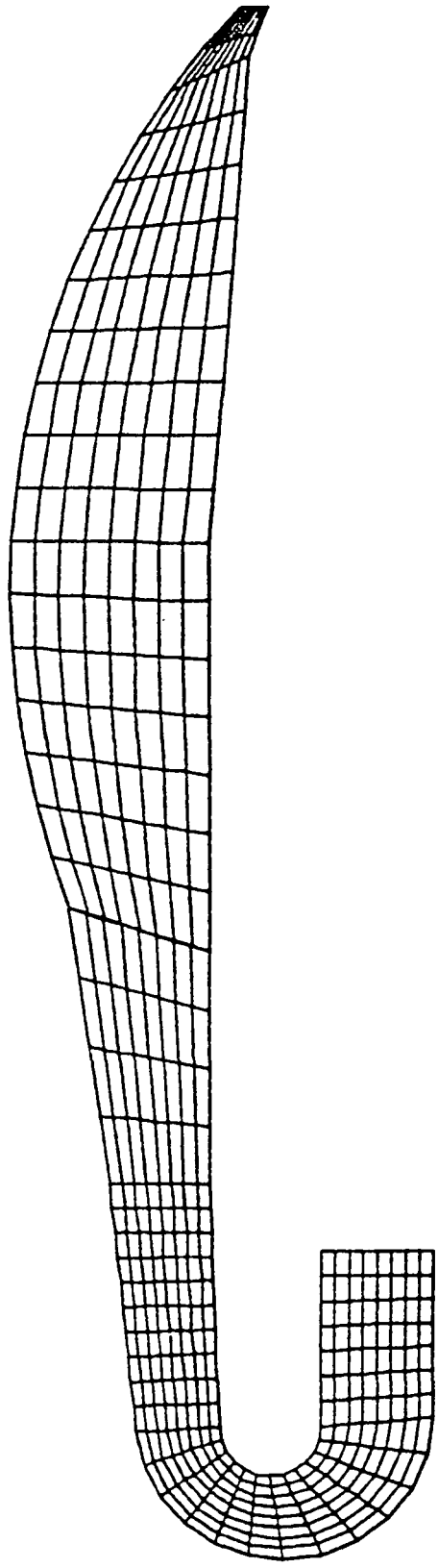

Fig. 31 DFNUS HGM Turnaround Duct and Bowl Cross-Section Grid

Step one takes place in the geometry module where we make use of the aforementioned built-in interpolation capability to assign flow angles θ_{xy} and θ_{xz} (see Fig. 32), total pressure and the magnitude of the velocity to all nodal points. This is achieved by assigning values for all four quantities to zonal and/or sectional corner points as well as to all edge segmentation points. Values for all nodes along edges are then obtained by interpolation. Further interpolation over surfaces and interior spaces completes the process.

Initial flow angles clearly must be specified in a manner such that the resultant velocity vector is first, tangent to the walls involved, and second, in the general direction of flow as perceived or as obtained from flow visualization for the location in question.

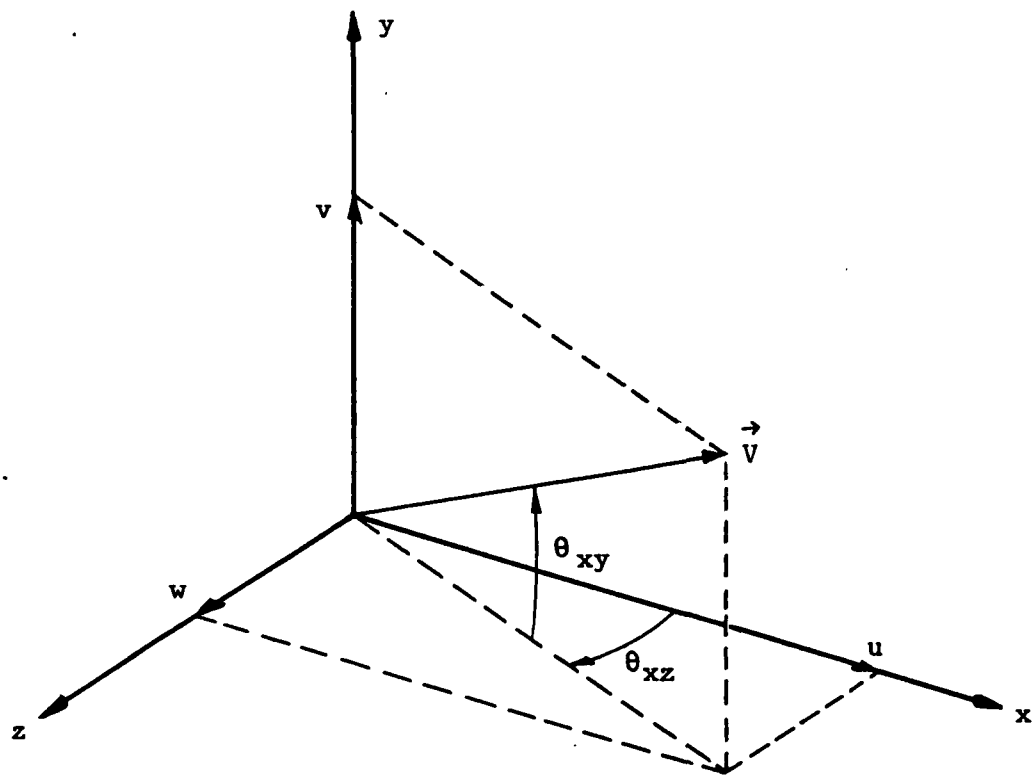

Fig. 32 Definition of Flow Angles

To set up the total pressure initialization, either experimental data must be available, or preliminary calculations must be performed using simplified methods. In the present study, total pressure values were used wherever available from experiment, and for nodal point locations where no experimental data were available values were estimated.

Assuming that the mass flow through the configuration is known, we can use the total pressure data in conjunction with cross-sectional area values from the geometry to arrive at velocity data by using a one-dimensional stream tube analysis.

Given the equations of continuity and state as well as Bernoulli's equation, i.e.,

$$\rho V = \dot{m}/A \tag{13}$$

$$p/\rho = RT \tag{14}$$

$$p + (\rho/2)\, V^2 = p_t \tag{15}$$

we can eliminate p from Eqs. (14) and (15) and solve for ρ and V. The result is

$$\rho = \frac{p_t}{2RT}\left[1 + \sqrt{1 - \frac{2RT}{p_t^2}\left(\frac{\dot{m}}{A}\right)^2}\,\right] \tag{16}$$

and

$$V = \frac{1}{\rho}\left(\frac{\dot{m}}{A}\right) \tag{17}$$

While the procedure just described is straightforward in the turnaround and the transfer ducts, it is a little more difficult in the fuel bowl. Inspection of the situation in the fuel bowl shows that there must be two stagnation points, one each at $\varphi = 0$ and one at $\varphi = 180$ deg in the fuel bowl symmetry plane at the top of the bowl. This implies that another stagnation point must occur in the region of $30 \leq \varphi \leq 60$ deg at the top of the fuel bowl above the transfer duct. Along the stagnation streamlines the

velocity, according to potential flow, decreases linearly to zero. Hence, for the purpose of initialization, we assign zero velocity at the corner points at $x = x_{max}$, and at the third stagnation point with assumed approximate values at edge segmentation points inbetween.

To establish initial values in the interior of the fuel bowl, it is useful to define streamtubes (approximately) on an unwrapped grid of the bowl as shown in Fig. 33. Local streamtube cross-sectional areas can then be calculated from the known geometry. Application of Eqs. (16) and (17) to individual streamtubes then leads to initial values for the interior of the fuel bowl. Values thus established for the two flow angles, the velocity magnitude and the total pressure are saved as part of the output from the geometry module.

Step two of the initialization process takes place in the integration module which uses as input the output from the geometry module.

As a first step, we use the velocity magnitude and the total pressure to solve Eqs. (14) and (15) for the density ρ and the static pressure p. Secondly, we use the velocity magnitude and the flow angles to compute the three velocity components u, v, and w. Further, we can use p, ρ, and V to compute initial values for the total internal energy

$$E = \frac{p}{\rho(\gamma-1)} + \frac{V^2}{2} \qquad (18)$$

The final step in the process is to set the velocity components to zero at all wall nodes in order to satisfy the no-slip boundary condition. This completes the initialization process.

3.4 FLOWFIELD ANALYSIS

The PAGE code, as described in Section 3.1, represents a rather general methodology to process the fluid flow governing equations so that they can

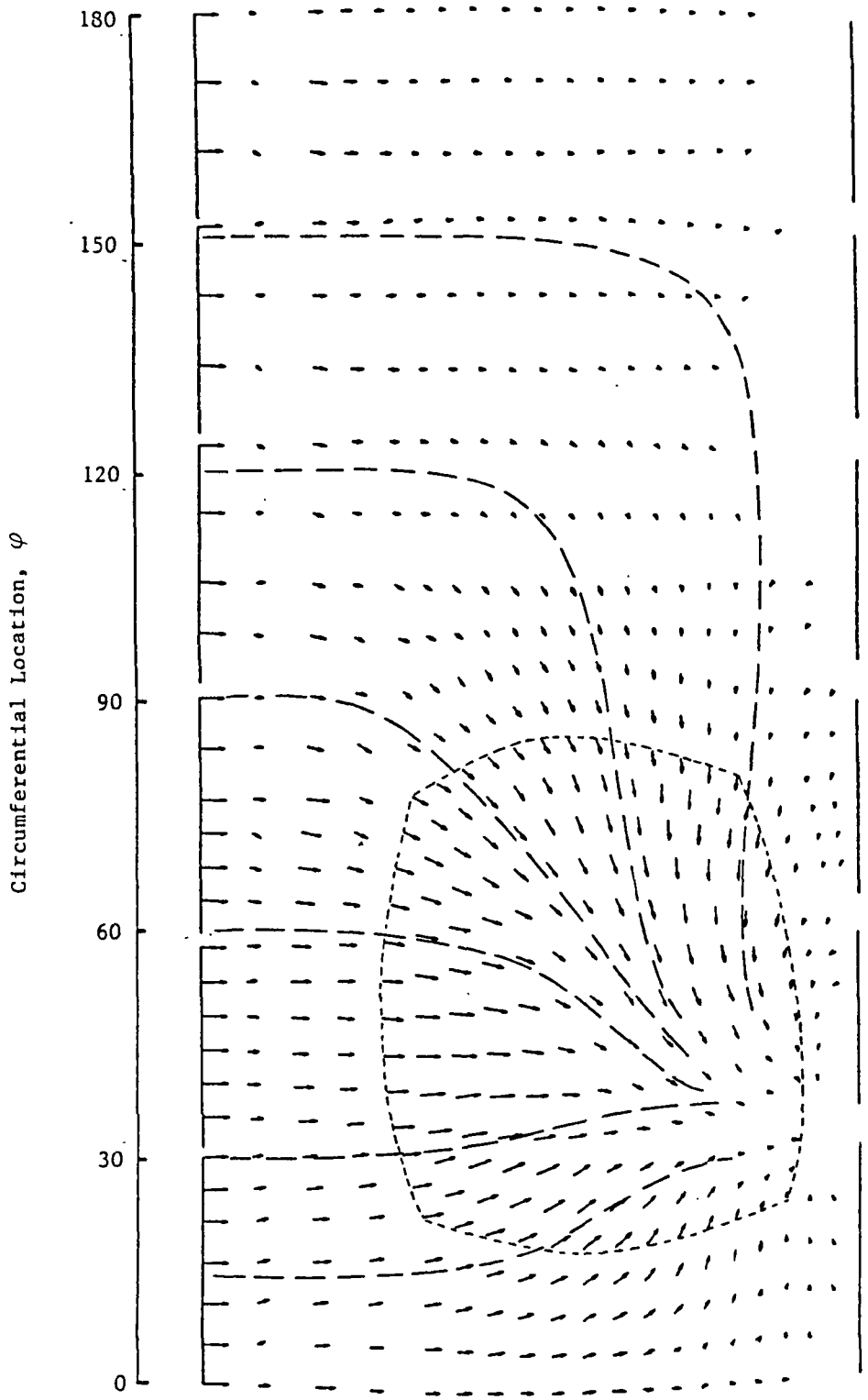

Fig. 33 HGM Bowl Center Plane Velocity Vector Plot and Streamtubes for Initialization

be solved by numerical integration. Actual numerical analysis requires the specification of a finite difference algorithm, thermodynamic, and transport properties as well as a procedure to implement the boundary conditions. This section will briefly discuss the treatment of all these topics.

3.4.1 Finite Difference Algorithm

For most of the cases calculated in the course of this study the two-step predictor-corrector MacCormack procedure was used which is one of the built-in finite difference schemes in the PAGE code. The time step used was generally a certain fraction of the (inviscid) smallest permissible CFL time step. The reduction factor was determined such that, depending on the local rate of change, a specified relative change in any of the primary flow variables was not exceeded. Nodal properties exhibiting unstable behavior in spite of the precautions taken, and which were encountered mainly in the region of the fuel bowl - transfer duct juncture due to highly skewed (i.e., nonorthogonal) grid elements in this region, were handled by averaging or interpolation.

As the study progressed, a multi-cycle predictor-corrector finite difference scheme (as illustrated in Fig. 34 for the two-dimensional case) was introduced. In conjunction with this, a time step routine which evaluated a local time step based on the local CFL condition, was implemented. This combination proved to be much superior to the previously used scheme and allowed us to get by with a very minimum of interpolation or averaging. It should be noted that the limitation of computational resources forced us to pursue these calculations using a rather coarse grid structure.

3.4.2 Transport Properties

Transport properties are specified in terms of dynamic viscosity and Prandtl number for turbulent flow. Effects of turbulence were modeled first

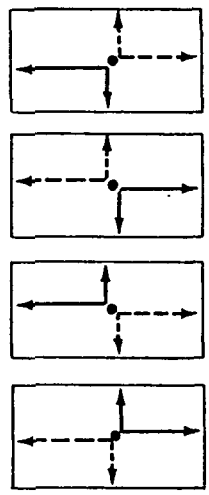

Step	Predictor		Corrector	
	x	y	x	y
1	F	F	B	B
2	B	F	F	B
3	F	B	B	F
4	B	B	F	F

Fig. 34 Multi-Cycle Predictor-Corrector Finite Difference Method

in simple form by applying an appropriate multiplier to the laminar viscosity, and second, by using a Prandtl-Van Driest algebraic turbulence model in which the turbulent viscosity is evaluated as a function of a local mixing length and the three-dimensional vorticity.

The magnitude of the effective turbulent viscosity in the hot-gas manifold can be estimated by applying Prandtl's mixing length hypothesis to the flow in the transfer duct. According to Prandtl (Ref. 9)

$$\mu_t = \rho \ell^2 \left|\frac{d\bar{u}}{dn}\right| \tag{19}$$

where ρ is the density, ℓ the mixing length, u the mean velocity and n the direction normal to the wall. For turbulent pipe flow ($Re > 10^5$) we can make use of the correlation established by Nikuradse (Ref. 9).

$$\frac{\ell}{R} = 0.14 - 0.08\left(1 - \frac{y}{R}\right)^2 - 0.06\left(1 - \frac{y}{R}\right)^4 \tag{20}$$

where y is the distance normal from the wall and R is the pipe radius.

The mean velocity gradient in the transfer duct is (approximately)

$$\left|\frac{d\bar{u}}{dn}\right| = \frac{\dot{m}}{\rho \pi R^2} \cdot \frac{1}{R} \tag{21}$$

For a given mass flow of 36 lb/sec per duct, a density of 1.0 lb/ft^3 and a duct radius of R = 0.271 ft, we obtain

$$\left|\frac{d\bar{u}}{dn}\right| \approx 6 \cdot 10^2 \ (sec^{-1}) \tag{22}$$

For y/R = 0.5, Eq. (20) yields a mixing length of ℓ = 0.031 ft. Substituting these values into Eq. (19), we obtain μ_t = 0.6 lb/ft-sec,

while the laminar viscosity of air at ambient temperature is approximately $\mu_L = 1 \cdot 10^{-5}$ lb/ft-sec. Therefore

$$\frac{\mu_t}{\mu_L} = \frac{0.6}{1 \cdot 10^{-5}} = 6 \cdot 10^4 \tag{23}$$

indicating that the effective turbulent viscosity is roughly four orders of magnitude higher than the laminar viscosity.

The Prandtl-Van Driest turbulent viscosity model is obtained by replacing the magnitude of the mean velocity gradient in Eq. (19) with the magnitude of the vorticity so that we can write

$$\mu_t = \rho \ell^2 |\Omega| \tag{24}$$

where

$$|\Omega| = \sqrt{\left(\frac{\partial u}{\partial y} - \frac{\partial v}{x}\right)^2 + \left(\frac{\partial v}{\partial z} - \frac{\partial w}{\partial y}\right)^2 + \left(\frac{\partial w}{\partial x} - \frac{\partial u}{\partial z}\right)^2} \tag{25}$$

and ℓ is determined by Nikuradse's correlation, Eq. (20). For flow passages with non-circular cross-sections, the geometric radius is replaced by the hydraulic radius.

3.4.3 Boundary Condition Treatment

In any attempt to solve the fluid flow governing differential equations careful attention must be given to the specification of boundary conditions. They must be physically correct and mathematically consistent. These general constraints still leave the investigator with a surprising variety of ways in which boundary conditions can be implemented. Some arrangements appear to work better than others depending on the flow configuration to be analyzed or on the nature of the flow.

In all calculations the no-slip conditions were enforced along all solid walls, in conjunction with appropriate thermal boundary conditions. No problems were encountered with these conditions. Difficulties, however, were encountered with the implementation of inflow and outflow boundary conditions which merit discussion. For the sake of simplicity for this discussion, we assume isothermal flow so that we deal with only four differential equations, namely the continuity and the three momentum (Navier-Stokes) equations.

Initial calculations of the nominal DFNUS HGM (fuel bowl - transfer ducts, but without turnaround duct) were performed by imposing all boundary conditions at the inflow boundary. Specifically, the four primary variables ρ, u, v, and w were held fixed. This implied that static pressure and mass flow were also held constant at the inlet. Eventually, integration in time starting from an appropriate initial condition should produce a solution for which the exit mass flow equals the inlet mass flow and for which the exit pressure is such that the average pressure gradient along the flow is consistent with specified mass flow and viscosity. Experience has shown that this convergence process may take considerable time (large number of time steps). In order to shorten the process, a "convergence acceleration" condition was generally applied at the exit. This meant that after each time step the three velocity components were scaled such that the exit mass flow would be equal to the inlet mass flow. For the fuel bowl and transfer duct configuration this set of boundary conditions appeared to work well. However, when applied to the turnaround duct, the result was a buildup of pressure waves both near the inlet and near the exit accompanied by a very discontinuous velocity field near the turnaround duct outflow boundary as illustrated in Fig. 35a. The boundary conditions were therefore reexamined.

We implemented a revised set of boundary conditions as follows. At the inlet flow boundary the total pressure and the flow angles (i.e., the flow vector direction) are specified and held fixed. While the density (and

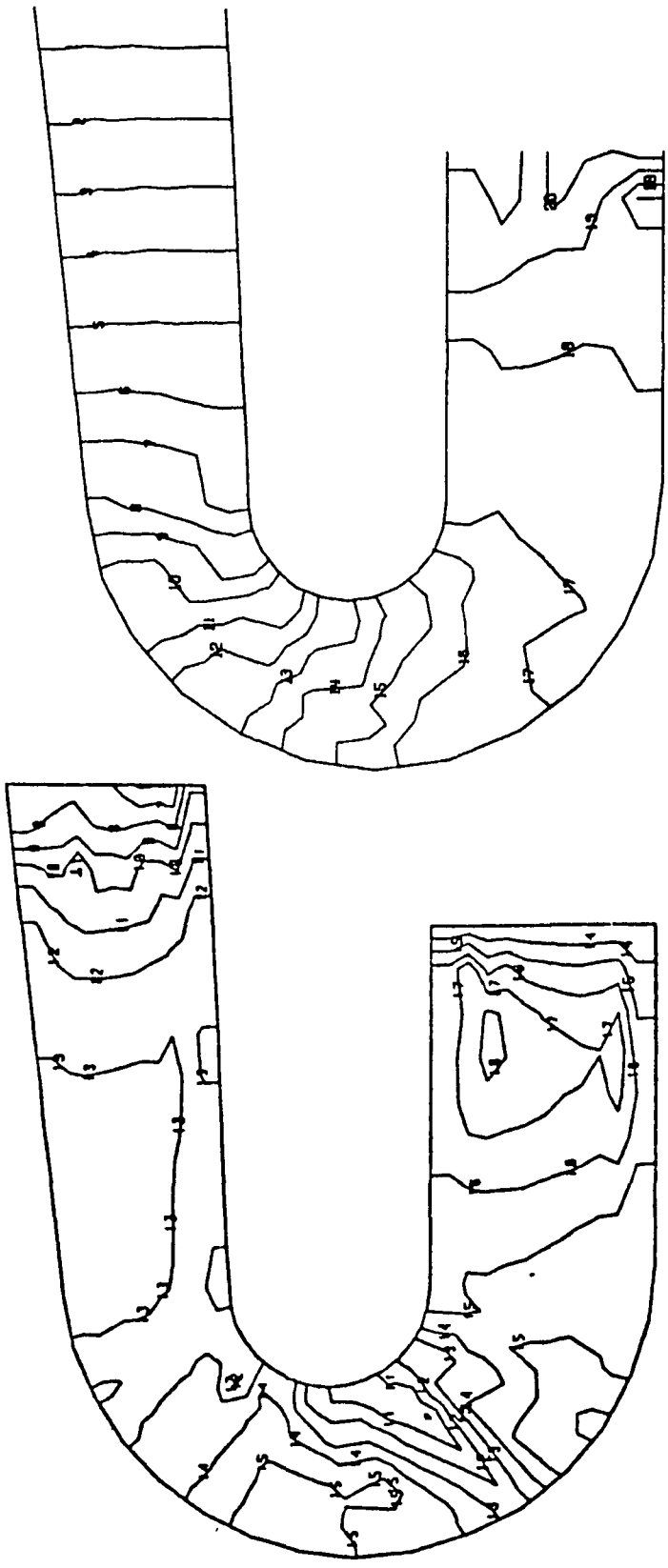

a. Original Boundary Conditions $164.5 \leq p \leq 205.6$ (psi)

b. Revised Boundary Conditions $165.0 \leq p \leq 202.9$ (psi)

Fig. 35 Effect of Boundary Condition Specification on Pressure Contours in Turnaround Duct

therefore the static pressure) is determined from the continuity equation, the three momentum equations are ignored. Instead, the magnitude of the velocity is computed from the definition of the total pressure and then resolved into its three components by using the specified flow angles. At the outflow boundary the static pressure is specified and held fixed. This implies that the density is fixed, and the continuity equation is therefore ignored. Using the density, the three velocity components are obtained from the momentum equations. Note that in contrast to the previously used boundary conditions, the mass flow at both flow boundaries is floating. Experience has shown that both inlet and exit mass flow smoothly converge to the same value which only depends on the specified viscosity and the imposed pressure gradient. A solution for specified mass flow is then easily obtained by changing the viscosity. Increased viscosity produces a reduced mass flow and vice versa.

The iteration on mass flow can be avoided by imposing a fixed mass flow at the inlet boundary. Again, the density (and thus the static pressure) is determined from the continuity equation. As before, the three momentum equations are ignored and the inlet velocity components are determined from the given flux terms. In this case convergence is reached when the floating exit mass flow converges to the value of the fixed inlet mass flow. Both variations of the new boundary conditions produced physically reasonable and stable results.

Typical pressure distributions obtained with the original boundary conditions and with the revised boundary conditions can be compared in Fig. 35a and 35b, respectively.

4. ANALYTICAL RESULTS

4.1 DFNUS NOMINAL CONFIGURATION

4.1.1 Turnaround Duct

In order to check out the previously described revised boundary conditions in conjunction with the multi-cycle finite difference scheme and the local time-step routine, axisymmetric turnaround duct calculations were performed. Although the real turnaround duct flow is not axisymmetric due to swirl and a nonuniform circumferential pressure distribution, the assumption of axisymmetric flow permitted us to perform a reasonably realistic calculation with a minimum number of 270 nodal points in a flow plane. A series of calculations was performed for specified constant upstream total pressure and downstream static pressure, for which approximate values were taken from the experimental effort. The viscosity was varied until the calculated mass flow through the turnaround duct was in agreement with the measured mass flow. Specified data and calculated results are summarized in Table 5.

The convergence of inlet and exit mass flow to a common value after starting the integration with initial values representing the anticipated nominal result (Case 3, m = 72 lb/sec) is shown in Fig. 36. All cases behaved as expected showing a monotonic increase in mass flow as the viscosity is gradually decreased. The viscosity is constant for each calculation and equal to the sum of the scaled laminar viscosity and a numerical viscosity added to supply additional stability for the coarse grid calculations. The numerical viscosity scale factor ε_μ was chosen such as to render the numerical viscosity roughly equal to the laminar viscosity.

Table 5 AXISYMMETRIC HGM TAD RESULTS

Case	Specified			Calculated		
	μ_L (lb/ft-sec)	ε_μ	$\dot{m}$ (lb/sec)	V_{max} (ft/sec)	P (psi)	M_{max}
1	0.6	0.5	30.0	209.0	165 - 203	0.184
2	0.3	0.25	45.0	315.1	165 - 201	0.276
3	0.1	0.05	72.0	591.2	153 - 191	0.497
4	0.05	0.025	82.0	786.3	139 - 188	0.656

All Cases: $P_{t,Inlet} = 205$ psi

$P_{Exit} = 164$ psi

$\mu = \mu_L + \mu_N \approx 2\,\mu_L$; $\mu_N \sim \varepsilon_\mu$

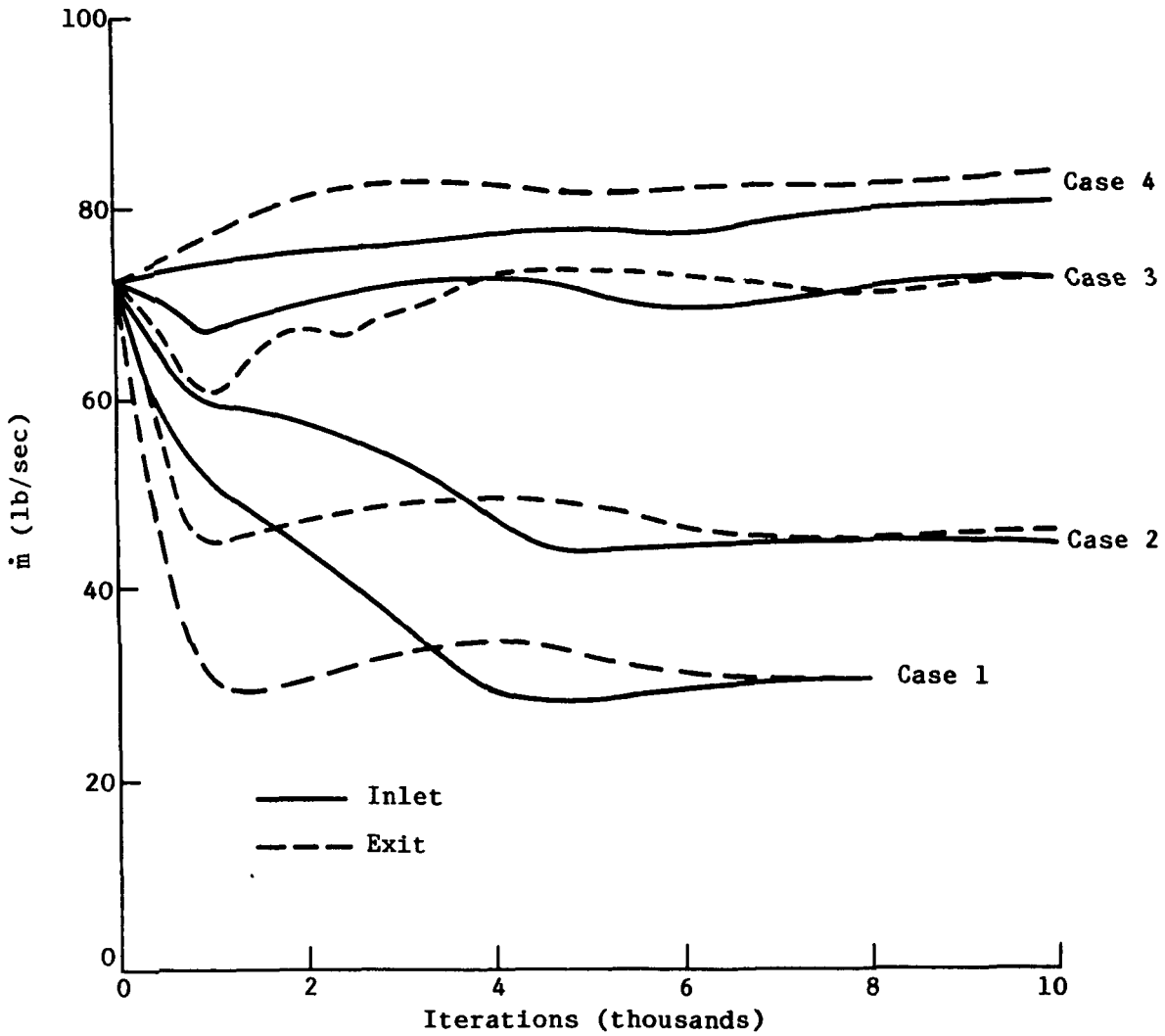

Fig. 36 Effect of Viscosity on Mass Flow

The following figures illustrate pressure contours, Mach number contours, and velocity vector plots for the cases calculated. The change in pressure contours (Figs. 37 and 38) from Case 1 with highest viscosity to Case 4 with lowest viscosity is particularly obvious, showing the gradual transition from highly viscous flow with strictly favorable pressure gradient to almost inviscid flow with distinct local pressure minima and an unfavorable pressure gradient downstream of the 180 deg turn.

While the Mach number contours (Figs. 39 and 40) appear to be very similar for the four cases, some distinctive features develop as the viscosity is decreased and the average flow velocity increases. Note the development of high speed regions at the inside wall upstream of the bend and on the outside wall downstream of the bend. Case 3 and Case 4 show detached Mach contours at the inner wall downstream of the 180 deg turn indicating the possibility of flow separation. This is confirmed in the velocity vector plots (Figs. 41 and 42) which show very slow flow for Case 3 and reverse flow for Case 4 in that region. While the turnaround duct exit shows the typical viscous laminar velocity profile for all cases, note that at the inlet, as the viscosity is decreased, the velocity retains more and more its initial plug flow profile.

4.1.2 Fuel Bowl and Transfer Ducts

In the spirit of tackling problems successively rather than simultaneously, calculations for the fuel turbopump HGM were first performed for the fuel bowl and transfer ducts without the turnaround duct. The grid for this configuration was illustrated in Figs. 17 through 19. To account for the effects of the turnaround duct on the flow in the bowl (and possibly the transfer ducts) turnaround duct exit experimental data were used to impose initial conditions at the bowl inlet. In fact, boundary conditions (aside from the no-slip wall boundary conditions) for these calculations were all imposed at the bowl inlet forming the upstream boundary, as discussed previously.

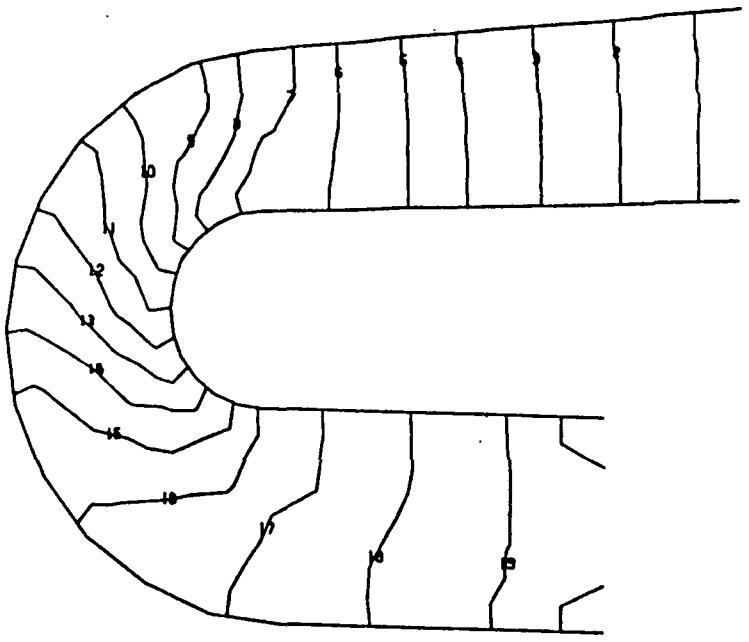

Case 1

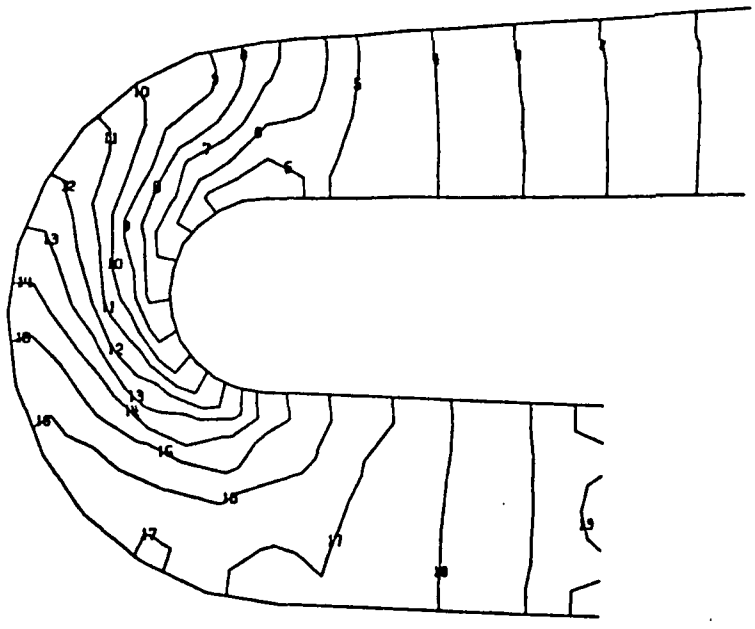

Case 2

Fig. 37 HGM TAD Flow - Pressure Contours

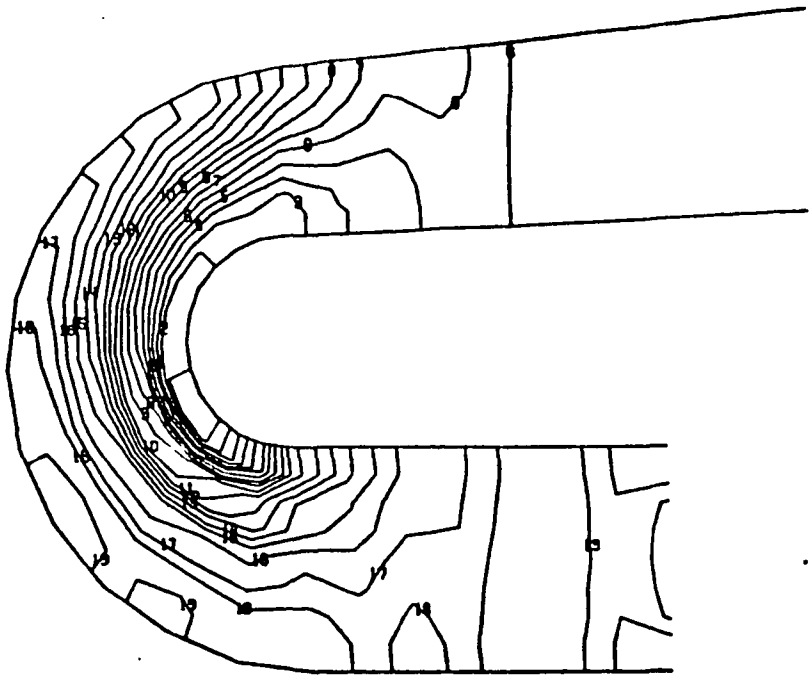

Case 3

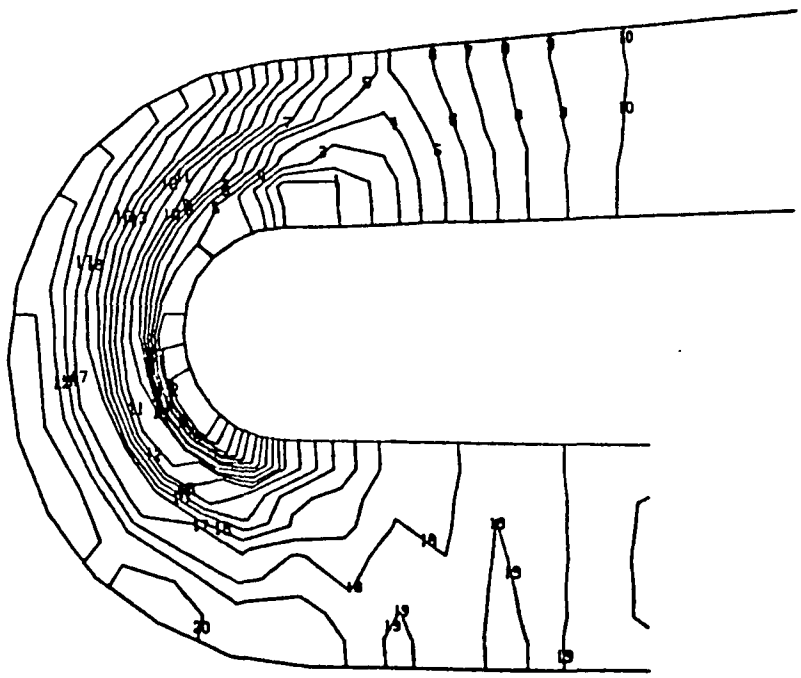

Case 4

Fig. 38 HGM TAD Flow - Pressure Contours

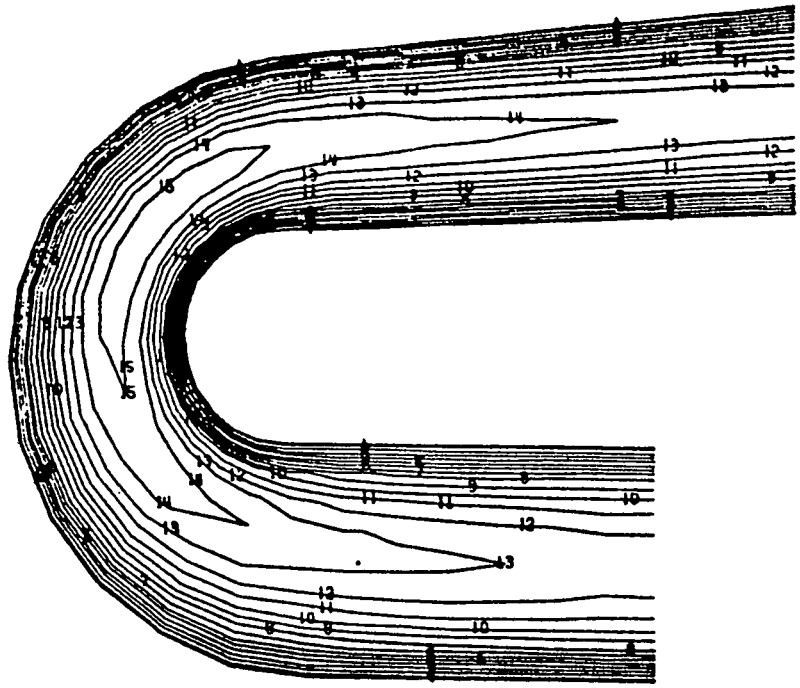

Case 1

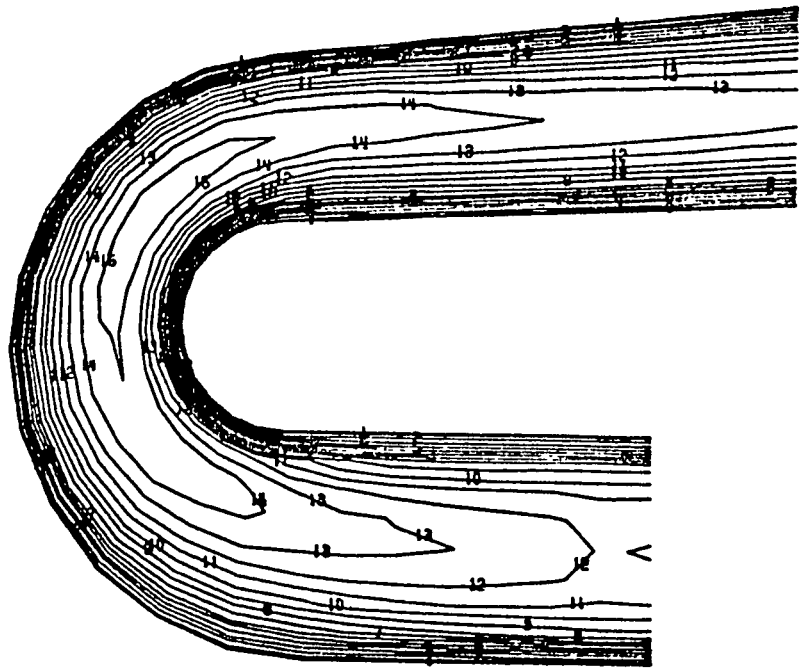

Case 2

Fig. 39 HGM TAD Flow - Mach Contours

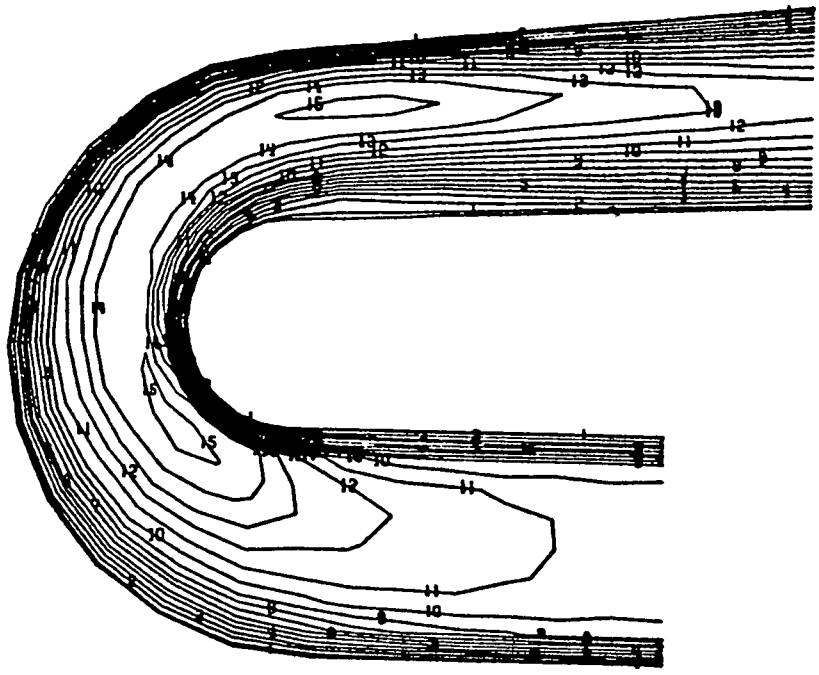

Case 3

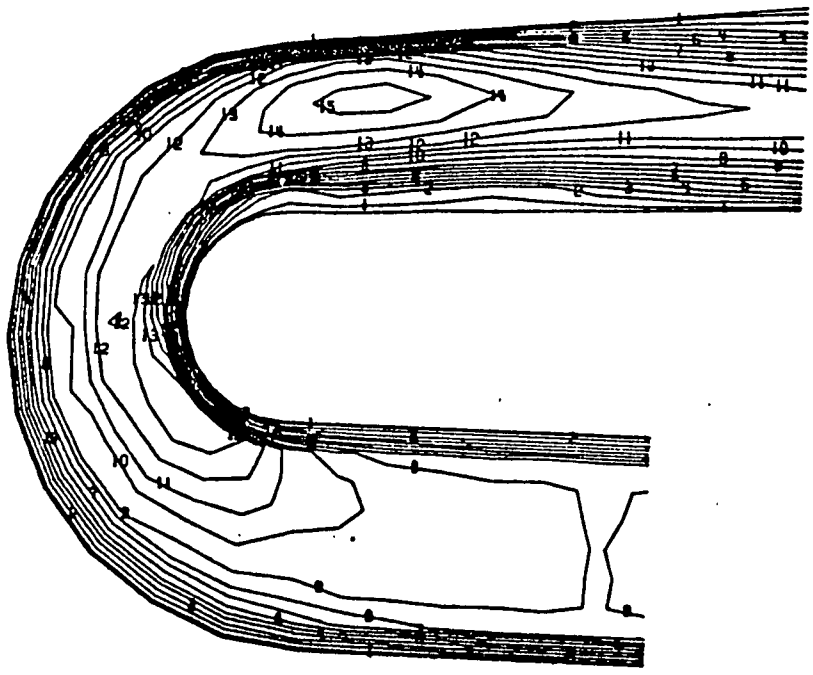

Case 4

Fig. 40 HGM TAD Flow - Mach Contours

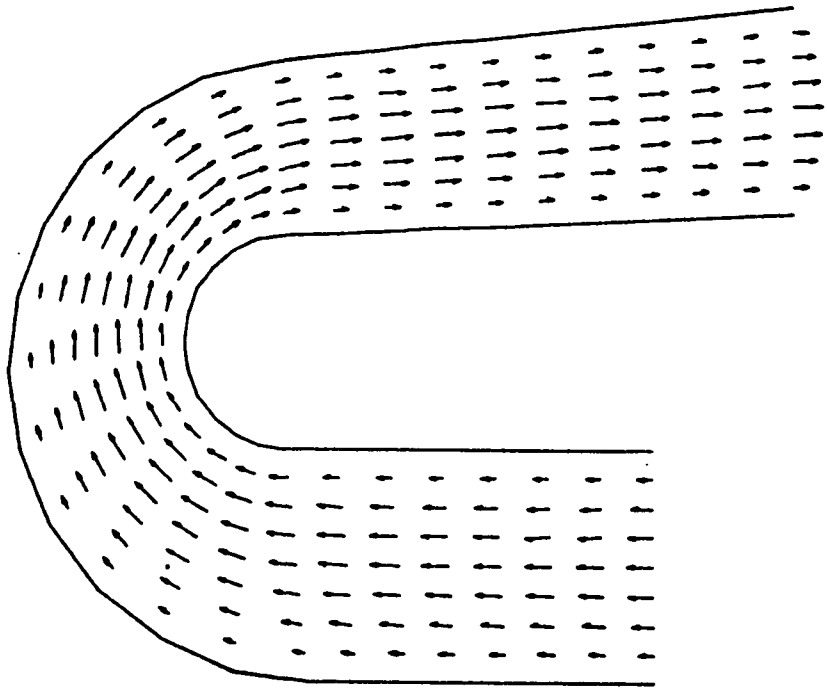

Case 1

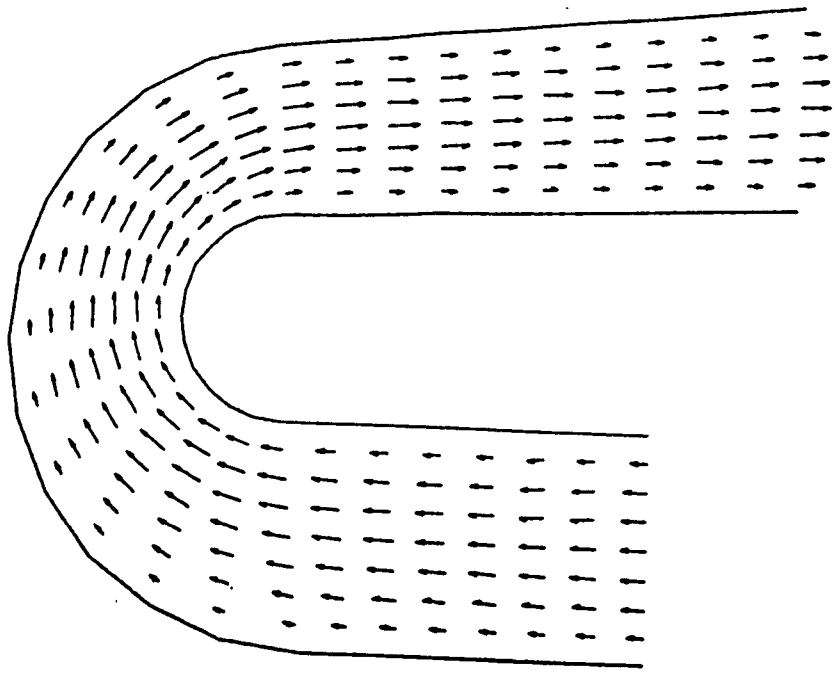

Case 2

Fig. 41 HGM TAD Flow - Velocity Field

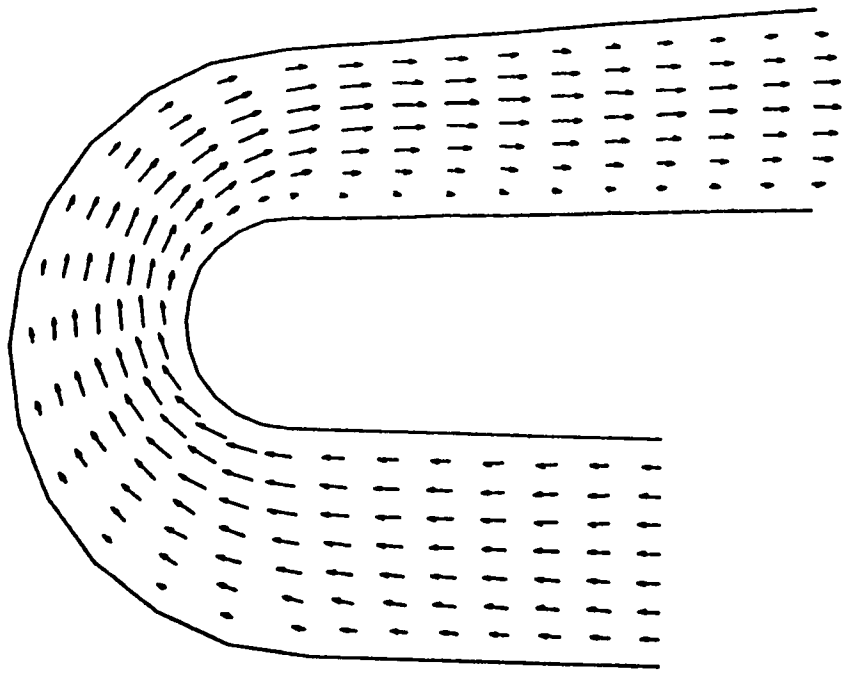

Case 3

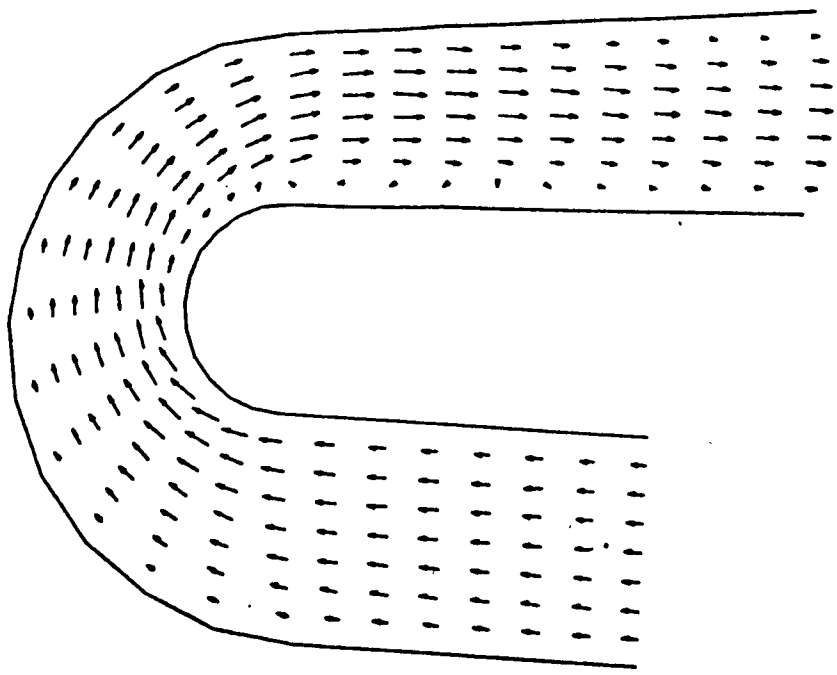

Case 4

Fig. 42 HGM TAD Flow - Velocity Field

Experimental data for the static and total pressure taken at the turnaround duct exit are shown in Fig. 43, indicating a circumferential distribution which deviates from the average by at most ± 2 percent. For the bowl inflow boundary condition we simplified the experimental distribution by assuming constant total pressure and static pressure linearly varying from the relatively high value at the back side (180 deg position) to the relative minimum at the front side (0 deg position) between the two transfer ducts, as also shown in Fig. 43. Bowl inlet boundary conditions for the velocity components were calculated such that all conditions were consistent with the available experimental data.

The entire flow field was then initialized as described previously. Figure 44 illustrates the velocity initialization in the bowl in terms of flow vector plots near the inner and near the outer bowl wall.

Integration of the fluid flow governing equations was performed using the two-step MacCormack predictor-corrector finite difference scheme. While the mass flow at the transfer duct exit was inforced through appropriate scaling of the velocity vector, convergence to the steady state solution was monitored in two ways.

Ideally, the unsteady terms of the governing equations should vanish as the steady state solution is approached. In practice, however, a discretized set of equations is solved, rather than the original partial differential equations. Hence, taking this into account, as well as other sources of error accummulation, one looks for a vanishing slope of the time derivative terms. The level at which these terms stabilize relative to their initial value is then a measure for the quality of the initialization. The behavior of the unsteady terms with time is shown in Fig. 45 in the form of the normalized sum of the squared time derivatives (summed over all nodal points).

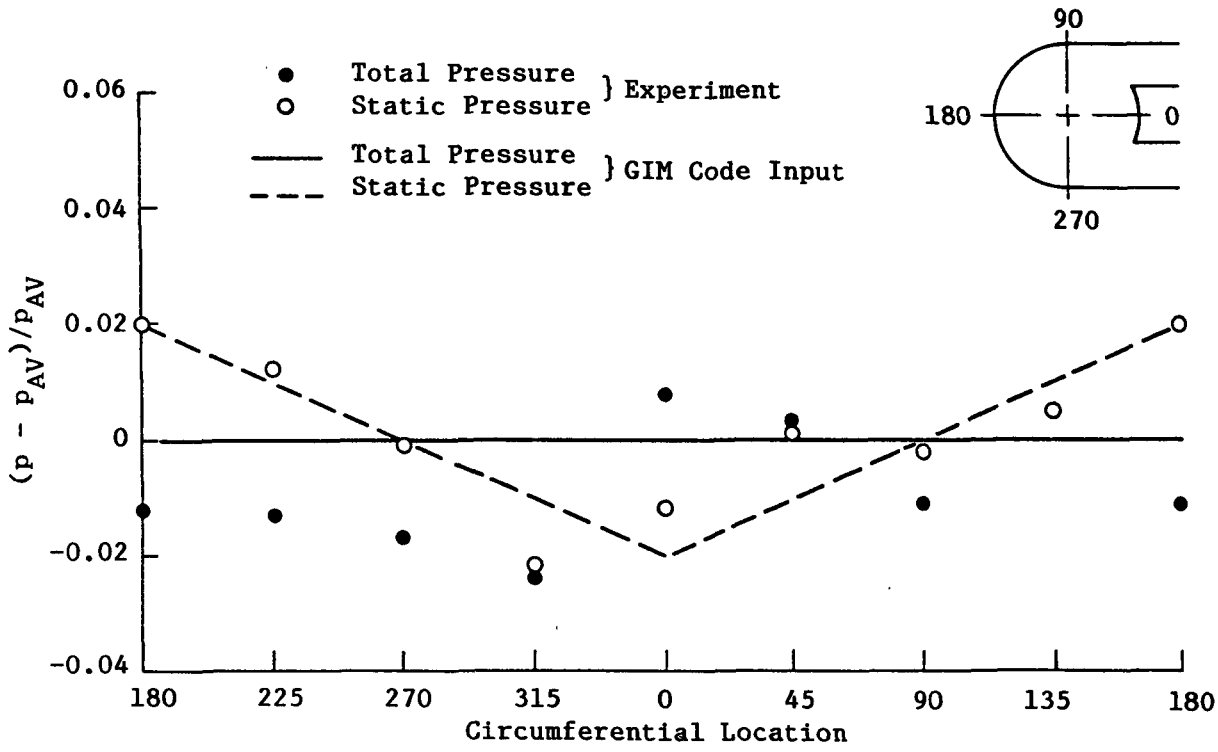

Fig. 43 Turnaround Duct Exit Pressure Variation

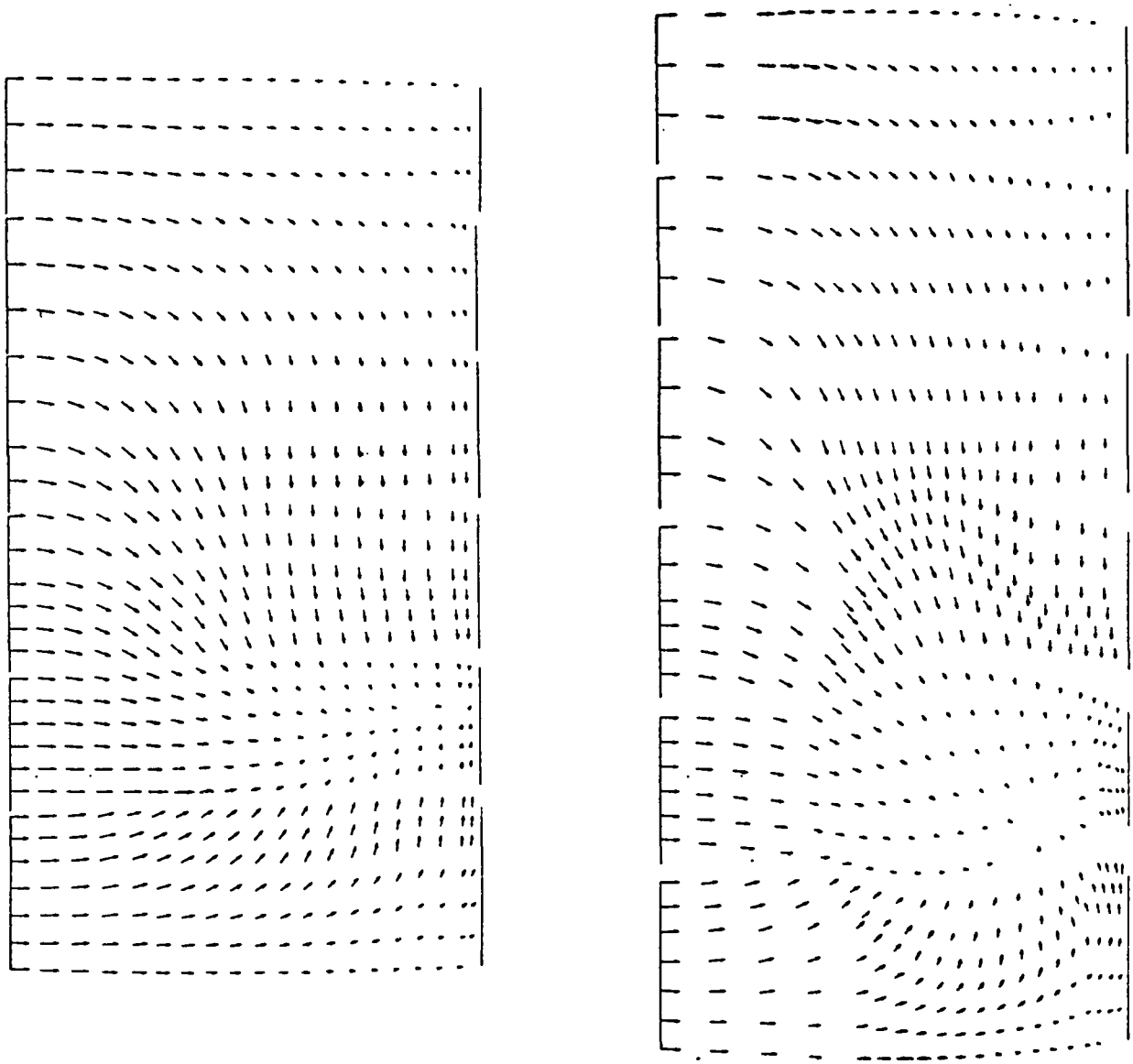

Fig. 44 HGM Bowl Velocity Vector Initialization Near Inside and Outside Wall

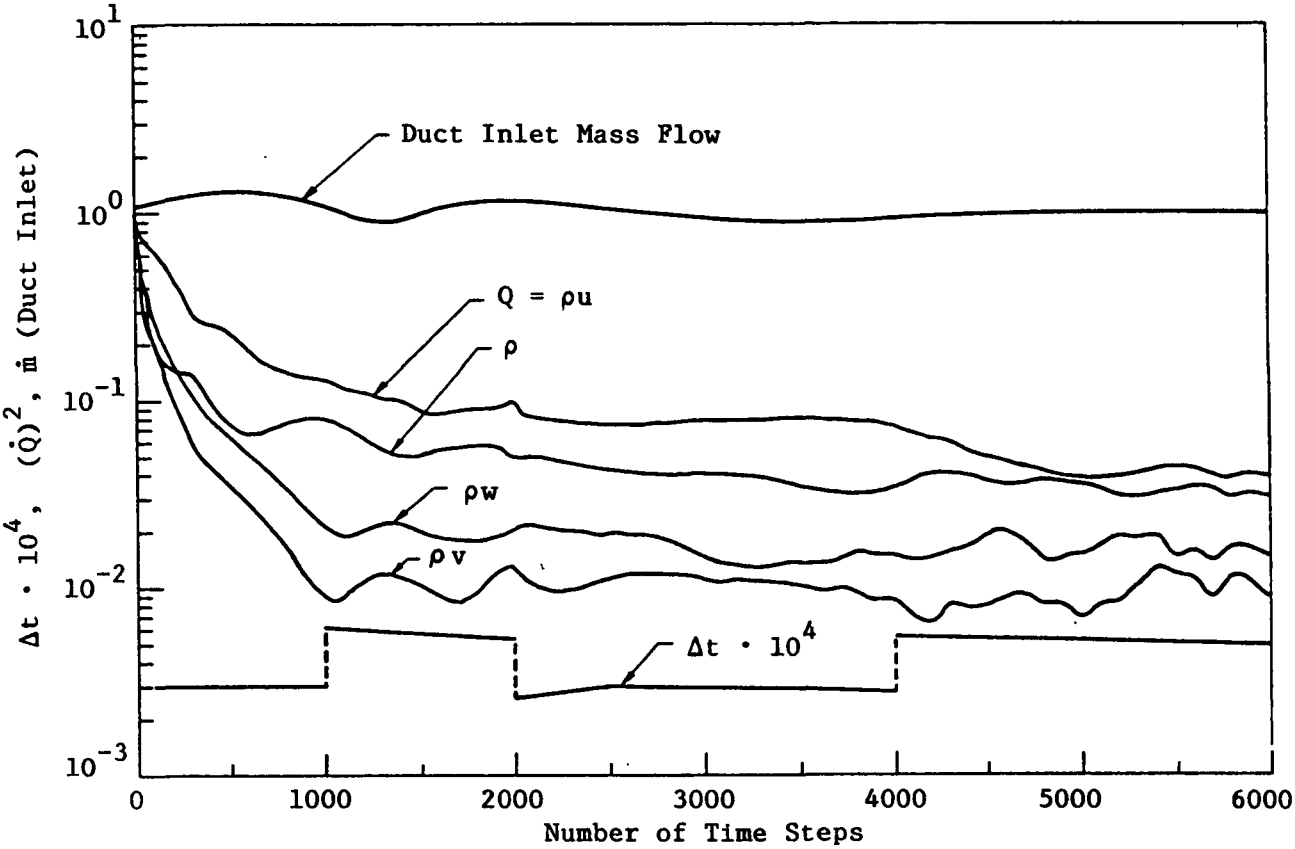

Fig. 45 Behavior of Unsteady Derivatives and Duct Inlet Mass Flow as Function of Time

It is also clear that once a steady state is reached, the mass flow through any definable cross-section along the flow must equal the inlet and/or exit mass flow. Therefore, as a secondary convergence criterion, the mass flow at the transfer duct inlet was monitored as a function of time. As seen in Fig. 45, the normalized transfer duct inlet mass flow exhibits a decaying oscillatory behavior, eventually reaching a steady value of unity after several thousand time steps, thus indicating that the duct inlet mass flow has settled on a value which is equal to that of the required steady state mass flow.

Flowfield results for the fishbowl are shown in Figs. 46 through 48 in terms of velocity vector plots, static pressure and Mach number contours, respectively, for a flow surface centered between inner and outer wall. Several prominent flow features can be identified from these plots.

First, almost the entire rear half of the bowl (within an angle of roughly 60 deg to either side of the symmetry plane) forms a region of rather constant static pressure in which the flow is gradually decelerated to stagnation conditions at the upper end of the bowl. Second, the highest velocities are encountered at the bowl inlet at an angular position of $30 \leq \varphi \leq 60$. Another region of relatively high velocity is seen to occur near the top of the bowl between $\varphi = 60$ and $\varphi = 90$ deg where the flow from the rear half experiences a relatively high acceleration as it enters the transfer duct.

Third, and as expected, a secondary stagnation region can be identified at the top of the fishbowl at an angular position of approximately 30 deg.

Finally, the high velocity (high momentum) of the flow at the angular position of the transfer duct inlet causes the flow to "pileup" at the upper transfer duct wall where it is redirected in various directions, thereby causing a swirl pattern and a region of flow separation in the transfer ducts as will be shown later.

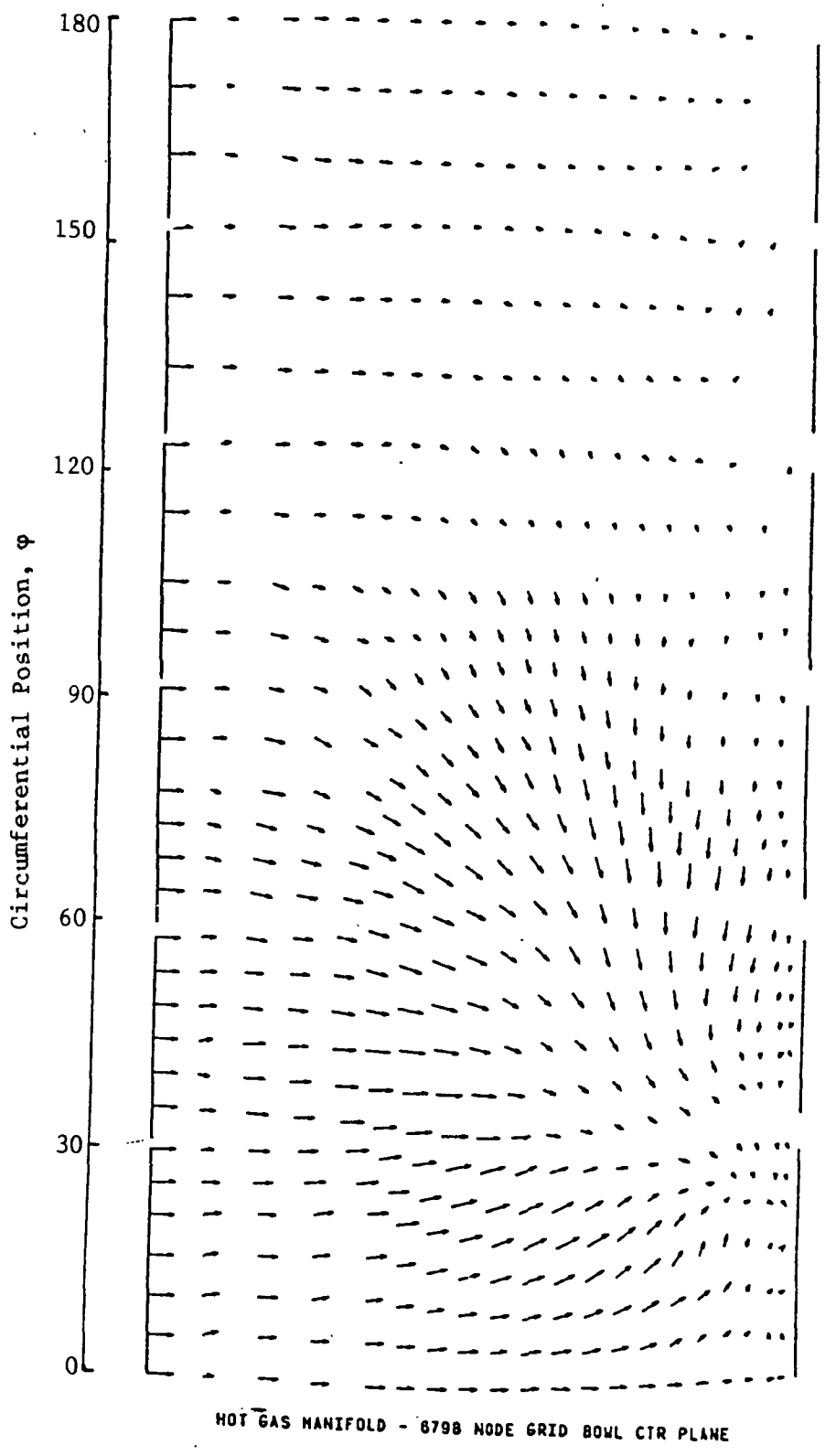

Fig. 46 HGM Bowl Center Plane Velocity Field

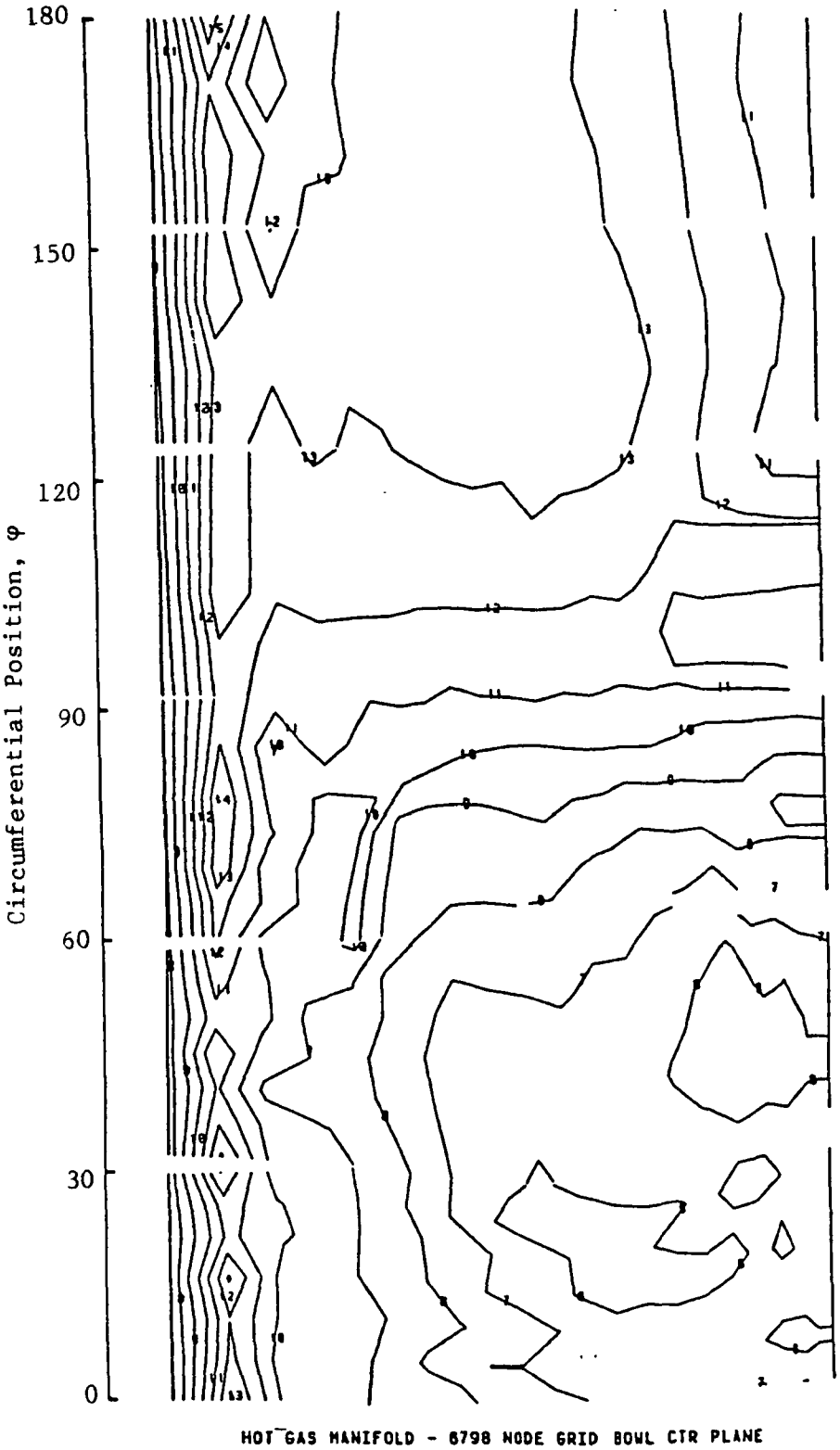

Fig. 47 HGM Bowl Center Plane Static Pressure Contours

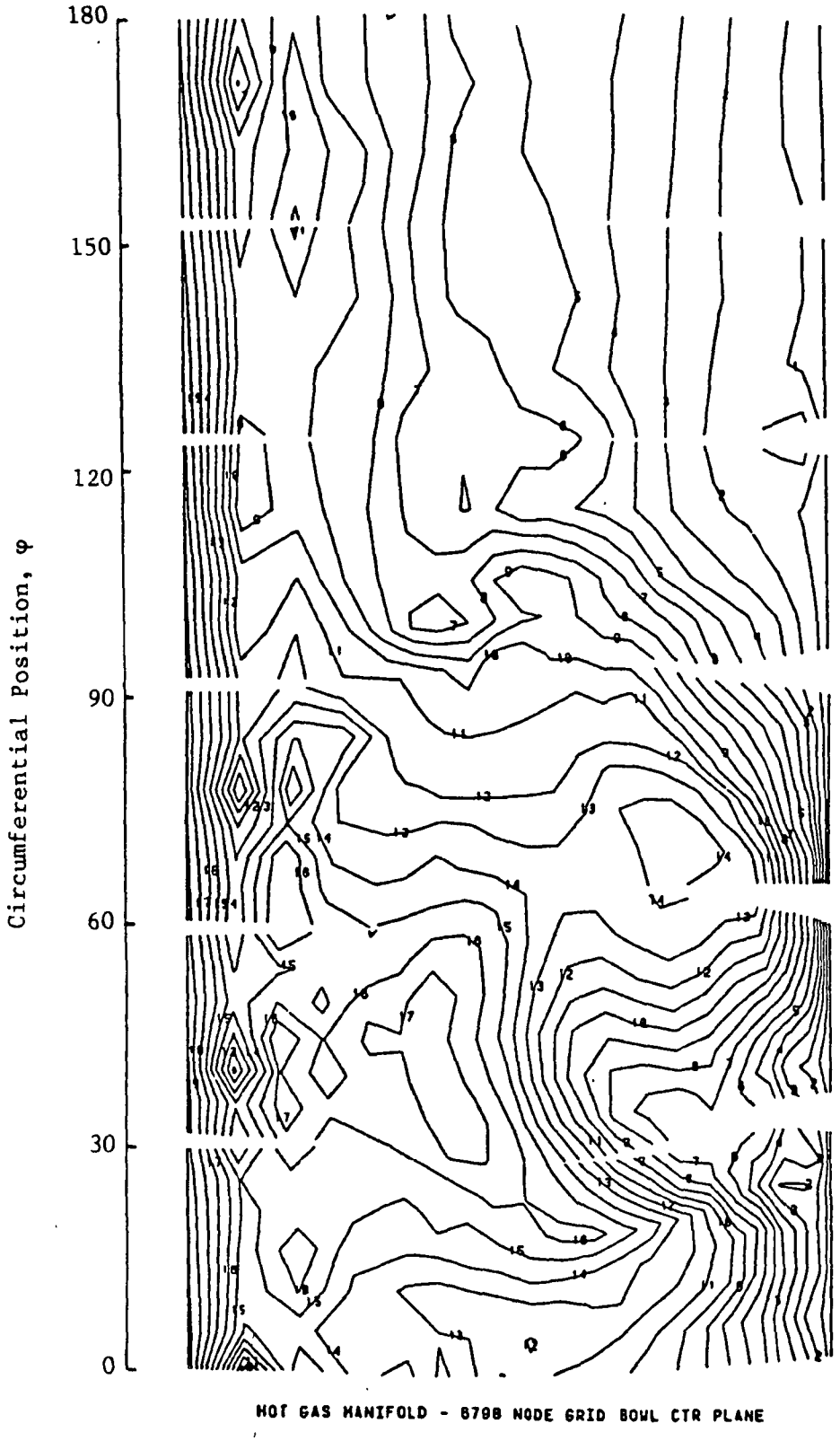

Fig. 48 HGM Bowl Center Plane Mach Number Contours

Flowfield results in the fishbowl can be compared with pressure distributions obtained experimentally. The comparison of static and total pressures versus circumferential location is shown in Figs. 49 and 50, respectively. Here "Model I" refers to the simple turbulence model consisting of the scaled up constant laminar viscosity only. "Model II" refers to the Prandtl-Van Driest model as described in Section 3.4.2. The computed circumferential pressure distributions for both turbulence models are seen to be in close agreement with the experimental data. The computational results provide additional detail in the vicinity of the transfer duct inlet in the form of distinct static pressure minima due to relatively higher velocities as the flow anticipates the turn into the transfer ducts. Other velocity and pressure results in the bowl were also surprisingly close between the two turbulence models. The reason for this close agreement is believed to be the fact that in this configuration the geometry is the main cause for large scale turbulence and that therefore the details of the turbulence models are of lesser importance in this case.

An overall view of the flowfield in the bowl and the transfer ducts is presented in Fig. 51 in terms of velocity vectors in the bowl center flow plane and an oblique flow plane in the transfer ducts. The particulars of the flow in the transfer ducts are shown in more detail in Fig. 52, presenting velocity vectors and Mach number contours. The flow separation and recirculation region found in the inner lower quadrant of the transfer duct is clearly visible. Note the corresponding low Mach number "bubble" in the Mach contour plot. These transfer duct flow features are in excellent qualitative agreement with the experiment which showed stagnation regions in the inner lower quadrants of the transfer ducts, as indicated in Fig. 53. Also shown in this figure are static pressure contours near the transfer duct exit, indicating the highest static pressure (i.e., a correspondingly low absolute velocity) in the inner lower quadrants.

An attempt was made to compare measured Mach number profiles in the transfer duct entrance to computed profiles. No agreement was found for

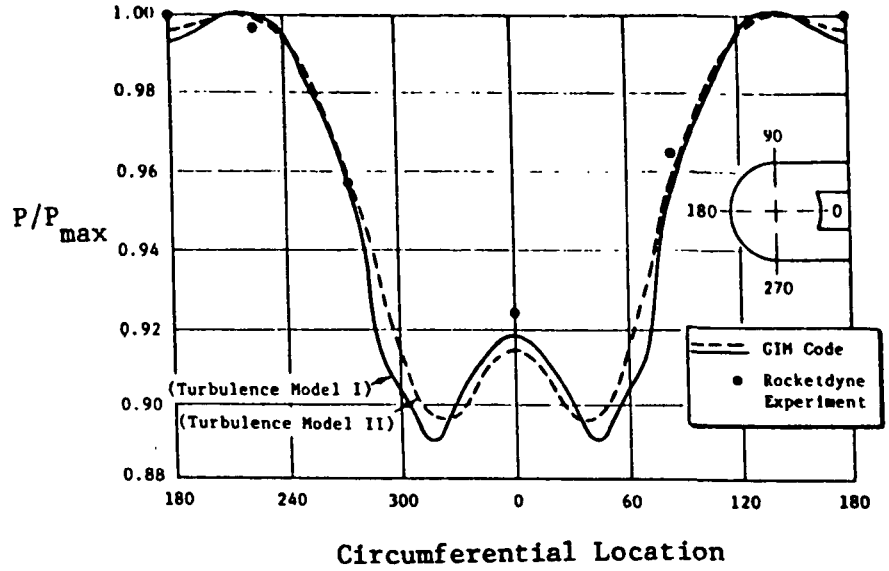

Fig. 49 Comparison of Computed Static Pressures to Measured Static Pressures in Bowl

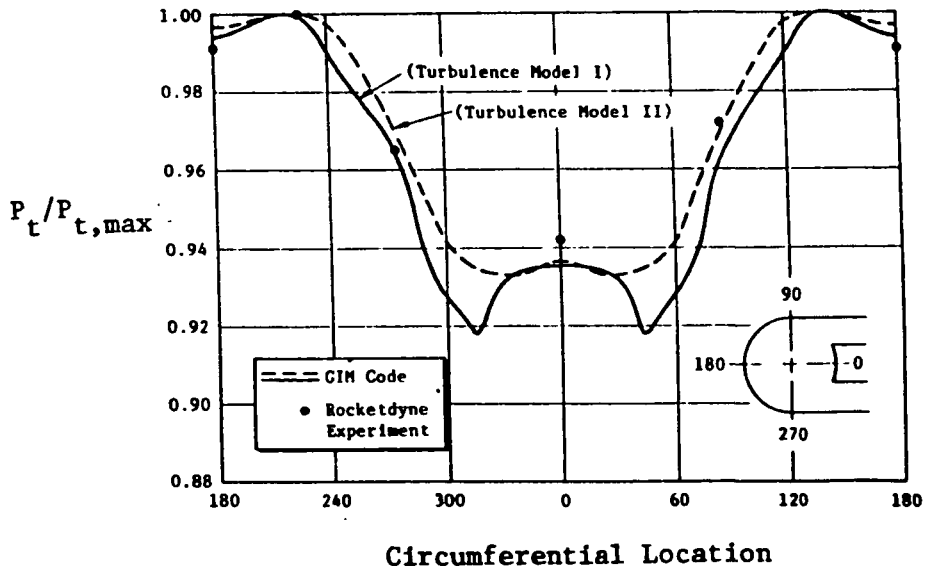

Fig. 50 Comparison of Total Pressures to Measured Data in Bowl

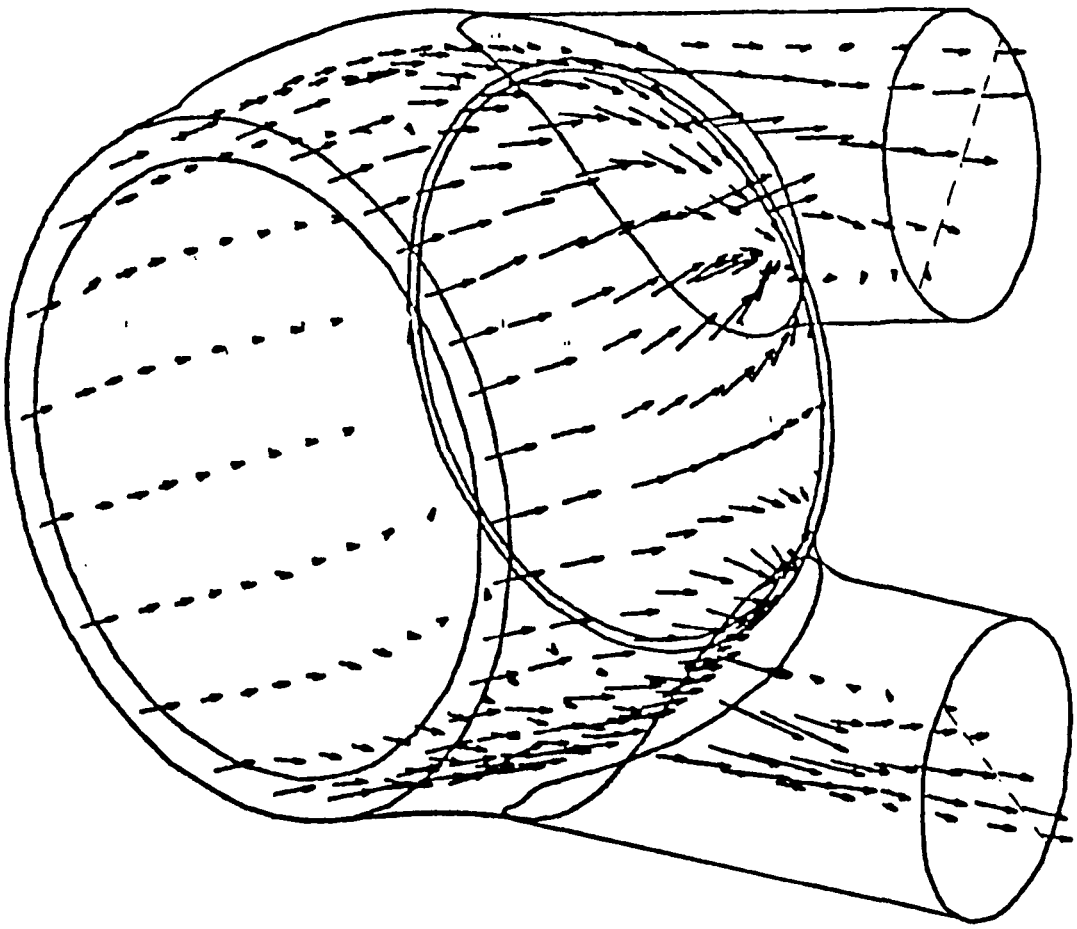

Fig. 51 Nominal HGM Bowl and Transfer Duct Flow Field

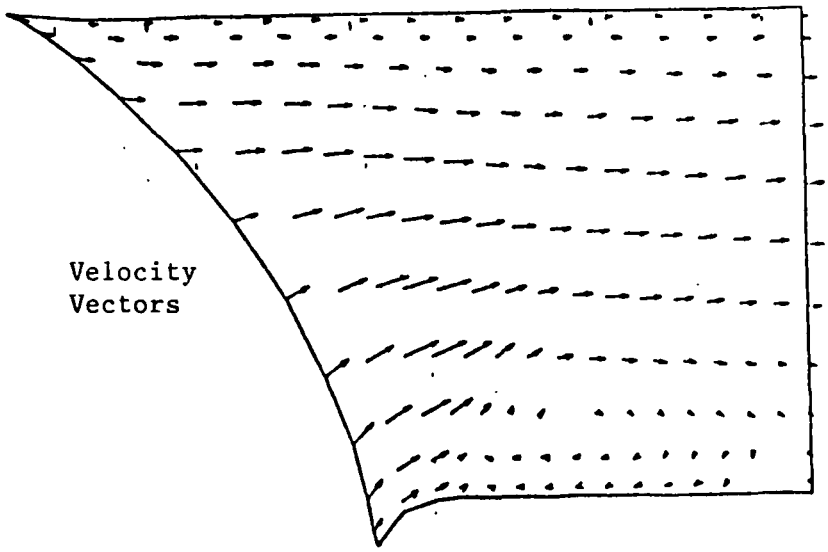

a. Velocity Vectors

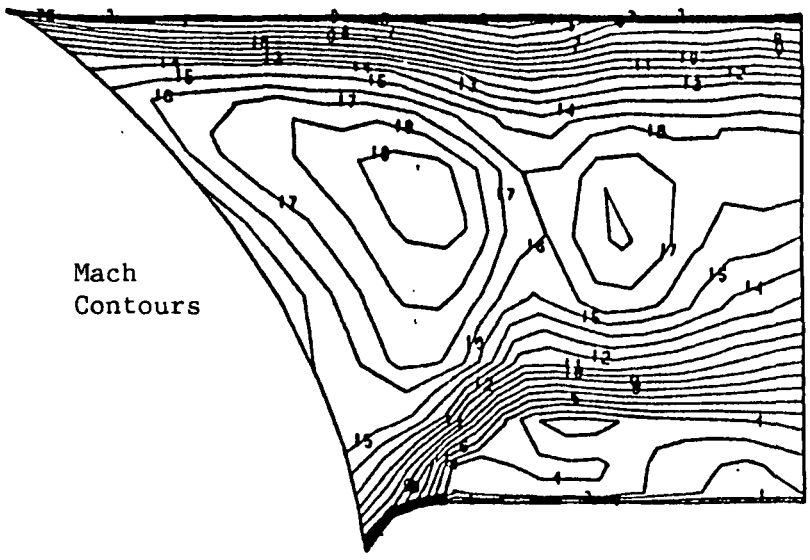

b. Mach Number Contours

Fig. 52 Nominal HGM Transfer Duct Flow Field Results

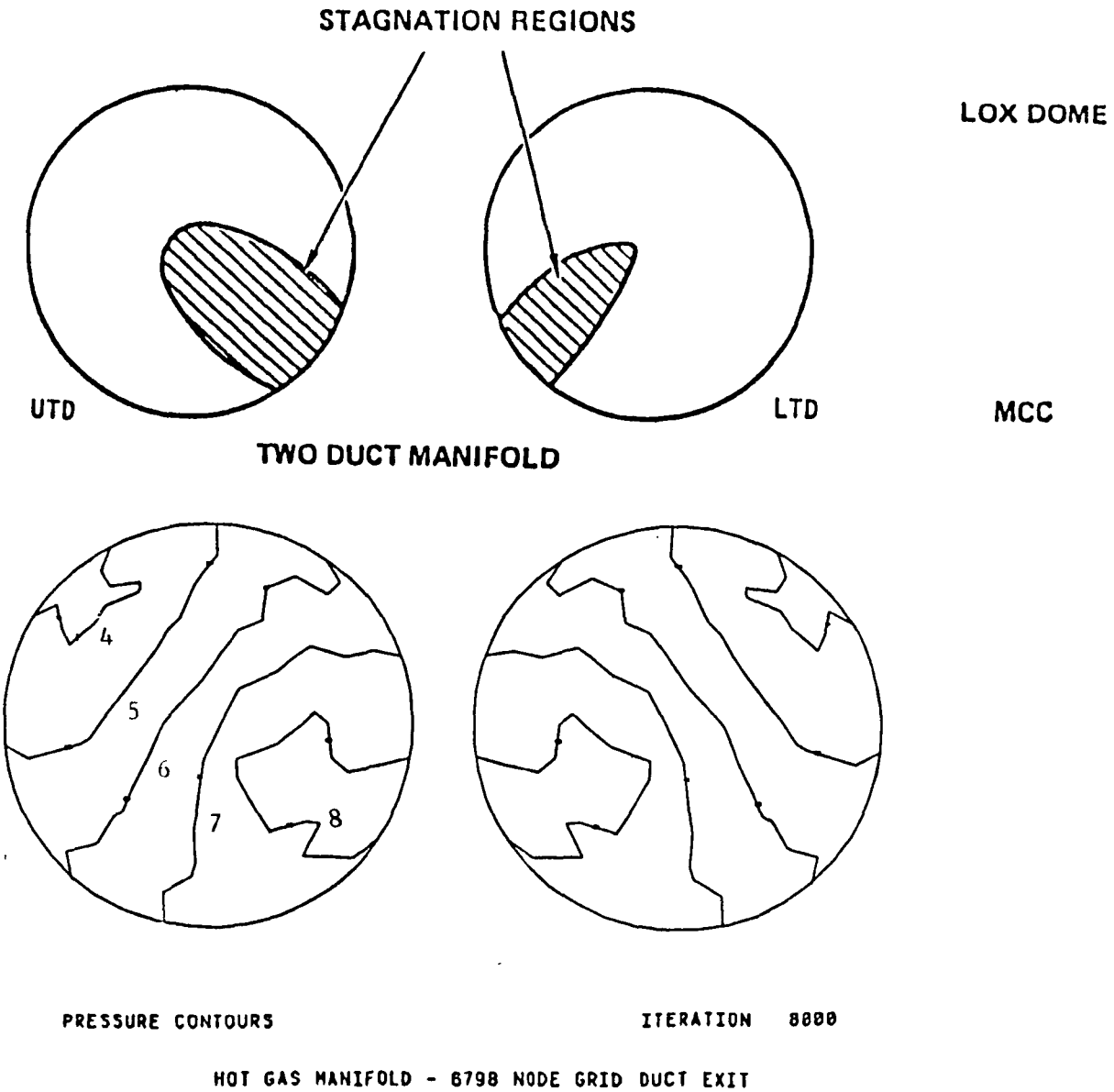

Fig. 53 Comparison of Computed Transfer Duct Exit Static Pressure Contours and Stagnation Regions from Experiment

these data as illustrated in Fig. 54. The reasons for the disagreement must be attributed to shortcomings in both the computational model and the experiment. While it is difficult to point to any single feature of the computational model which might be responsible, the coarse grid (i.e., lack of resolution) and the absence of a detailed turbulence model must certainly be considered contributing factors. Concerning the experiment, the data points were obtained using pitot probes aligned with the transfer duct axis. Flow visualization as well as the computational results indicate that the flow in this region is anything but aligned with the duct axis. Thus, anytime that pitot probes are not properly aligned with the direction of flow, the validity of the pressure data taken must be questioned.

For probably similar reasons, the computational model was not able to reproduce the details of the measured Mach number profiles at the transfer duct exit.

4.1.3 DFNUS HGM

This section describes the computational results obtained from the analysis of the complete hot gas manifold from the turbine exit to the transfer duct exit. The geometrical configuration was described previously and is illustrated in Figs. 29 through 31.

The multi-cycle predictor-corrector finite difference scheme was used to integrate the governing equations toward steady state. Turbulent flow was simulated using a high laminar viscosity at the value established for the solution of the flow in the turnaround duct, except for a slightly increased value of the numerical damping, which merely increases the effective viscosity by an amount proportional to the velocity. Inflow and outflow boundary conditions were imposed in terms of circumferentially constant total pressure at the turnaround duct inlet and constant static pressure over the transfer duct exit plane. Values for both were taken from

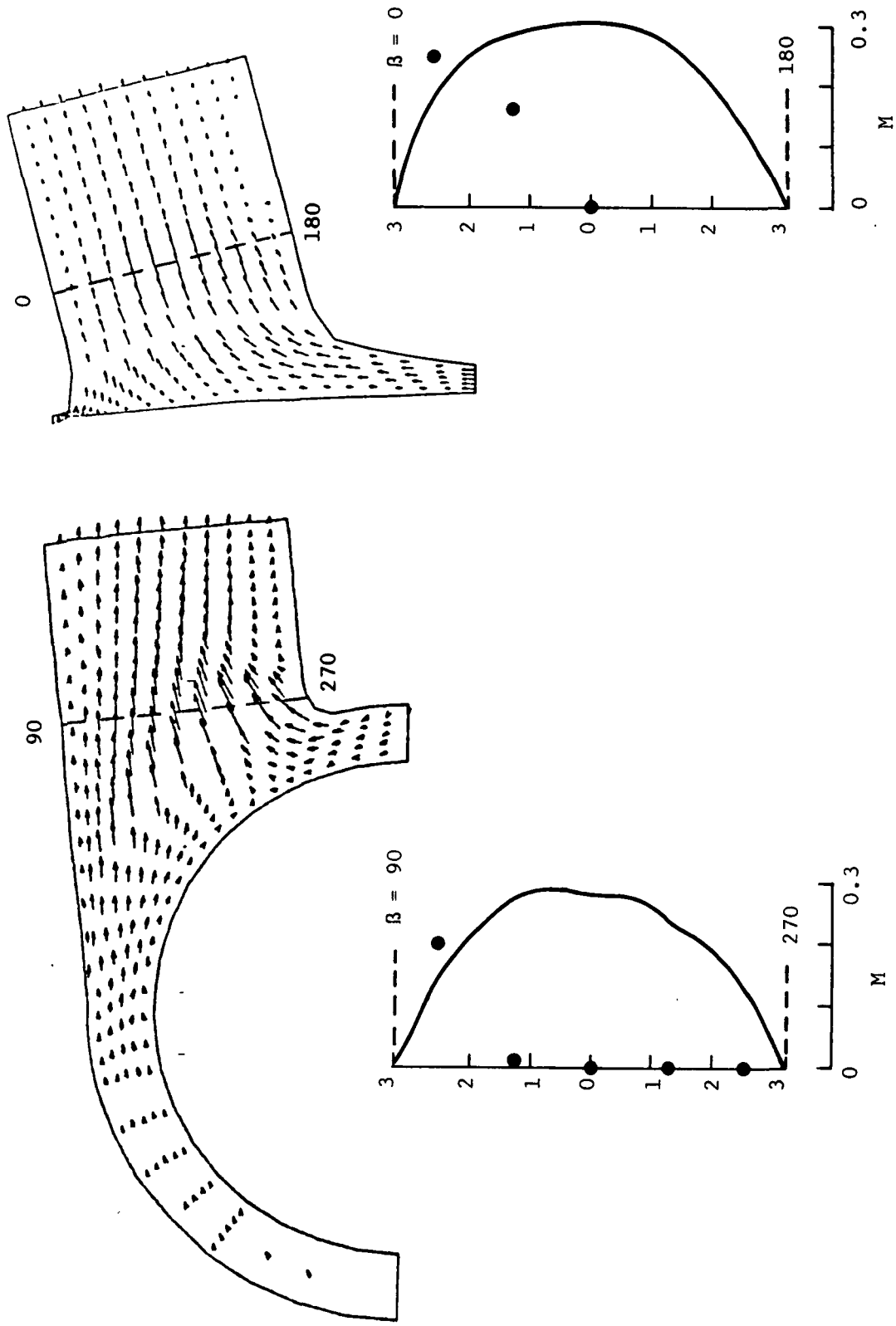

Fig. 54 Two-Duct HGM Duct Inlet Mach Number Variation

the experimental data*. The resulting mass flow through the manifold was at the required value which means that, under the adopted assumptions, the effective viscosity was consistent with the imposed pressure gradient.

Figures 55 through 57, representing a cut at φ = 45 deg through the turnaround duct and the bowl, joined to a center cut through the transfer duct, indicate an overall agreement with results discussed previously. From the velocity vector plot is is seen that a small region with nearly stagnating flow is found just downstream of the transfer duct entrance. The pressure contour plot confirms that this is a region of adverse pressure gradient and the Mach number contour plot indicates that a state of incipient separation has been reached at the bottom of the transfer duct.

Figure 58 shows a cut through the transfer duct (in a plane which is roughly perpendicular to the one shown previously) adjoined by a cut through the bowl normal to its axis. Apart from some small regions of instability manifesting itself in the form of "wiggly" velocity vectors and a concentration of high gradients in the contour plots, the results are largely as expected. No flow separation is found in this plane. Note that the flow component which has to negotiate the sharp turn from the bowl into the transfer duct is already small upstream of the turn (small Reynolds number per unit length).

Flow properties in an oblique cut at 45 deg relative to both previously shown cuts are illustrated in Fig. 59. Just as found in the earlier calculations, there is a relatively large region of very low velocity in the inner lower quadrant of the transfer duct. Although this velocity vector plot does not show any flow reversal as encountered previously, the present results are qualitatively in agreement with the earlier calculations.

*Recent experimental data indicate that the static pressure is not constant over the duct exit plane.

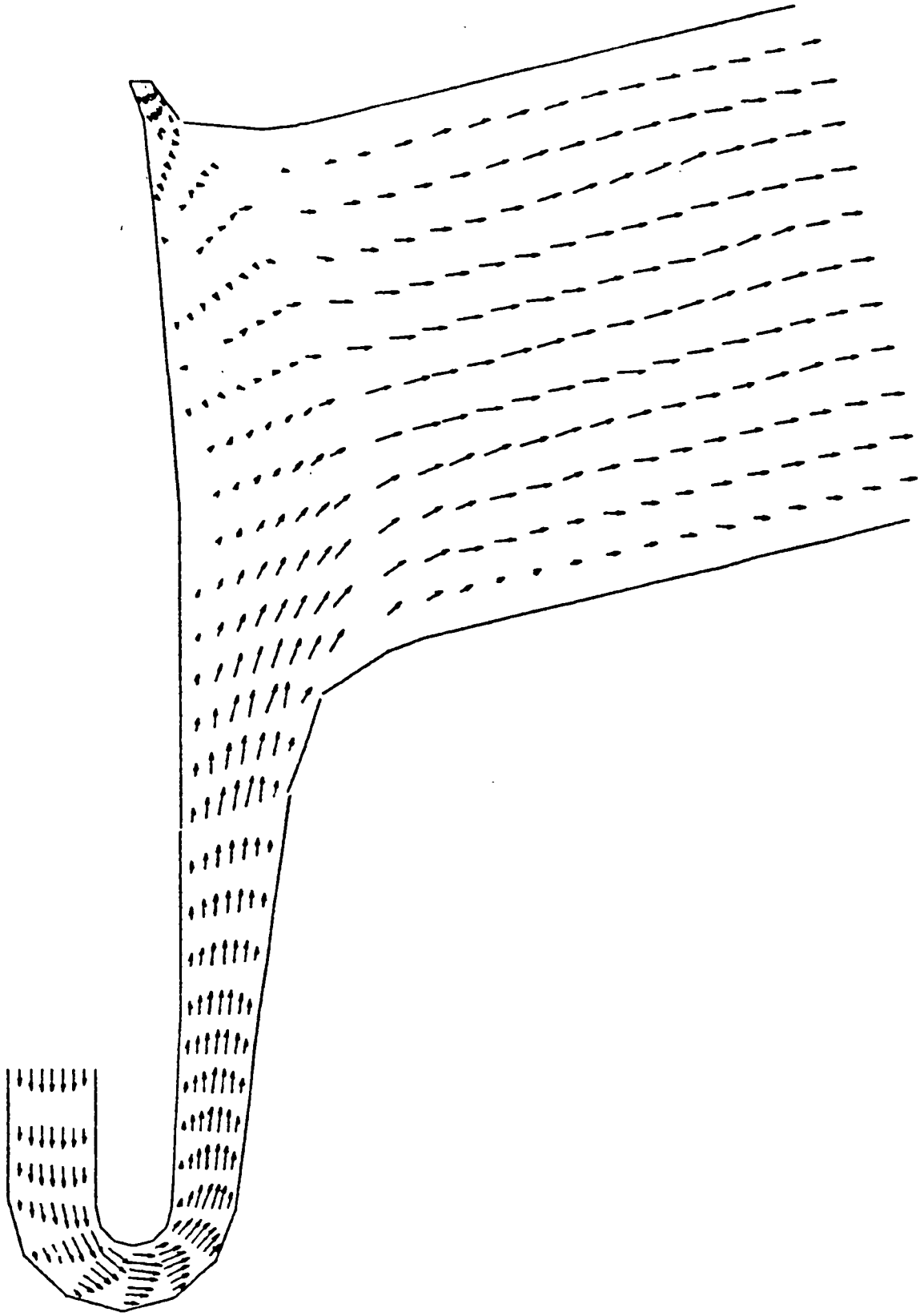

Fig. 55 DFNUS HGM Nominal Configuration Velocity Field

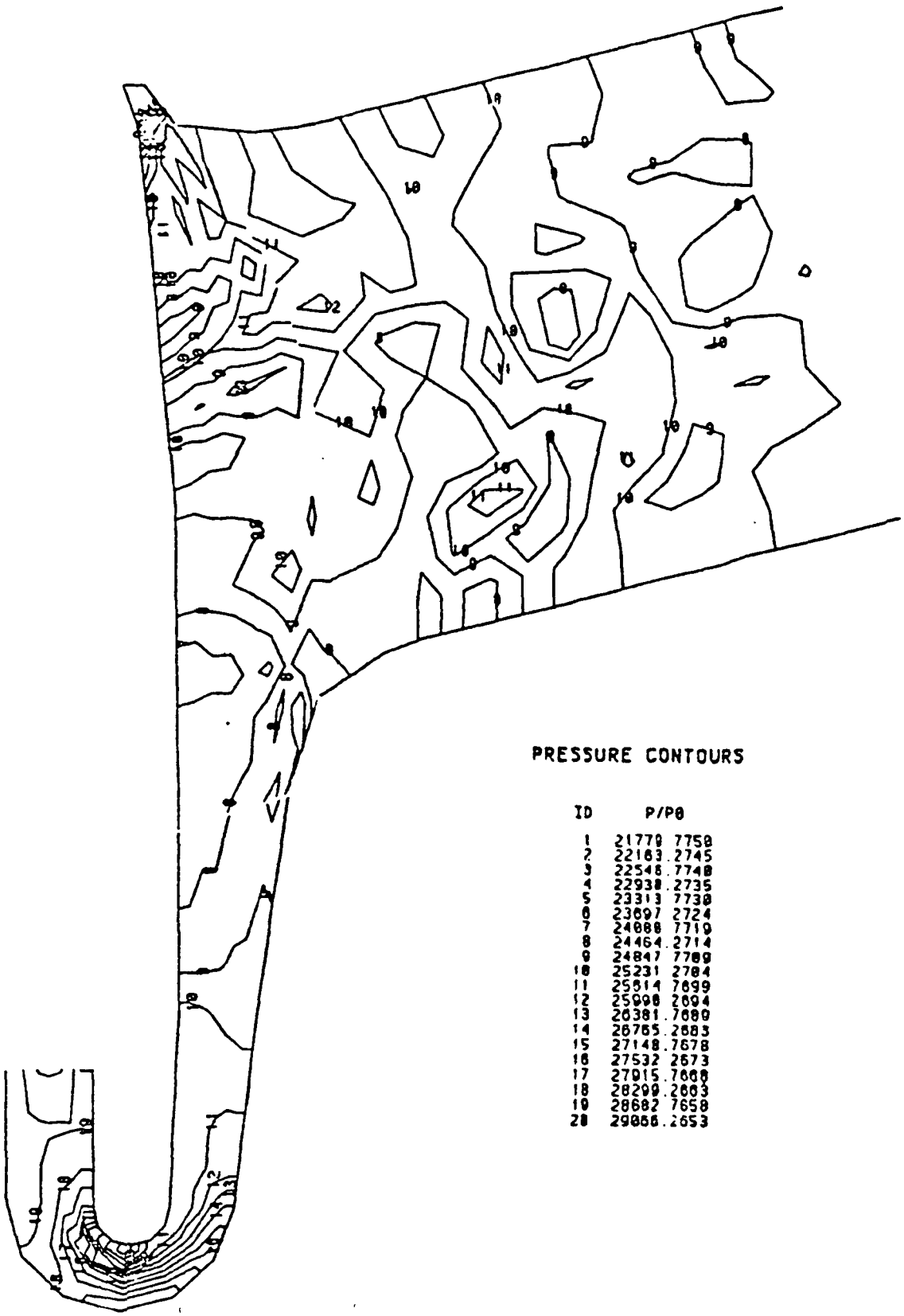

Fig. 56 DFNUS HGM Nominal Configuration Pressure Contours

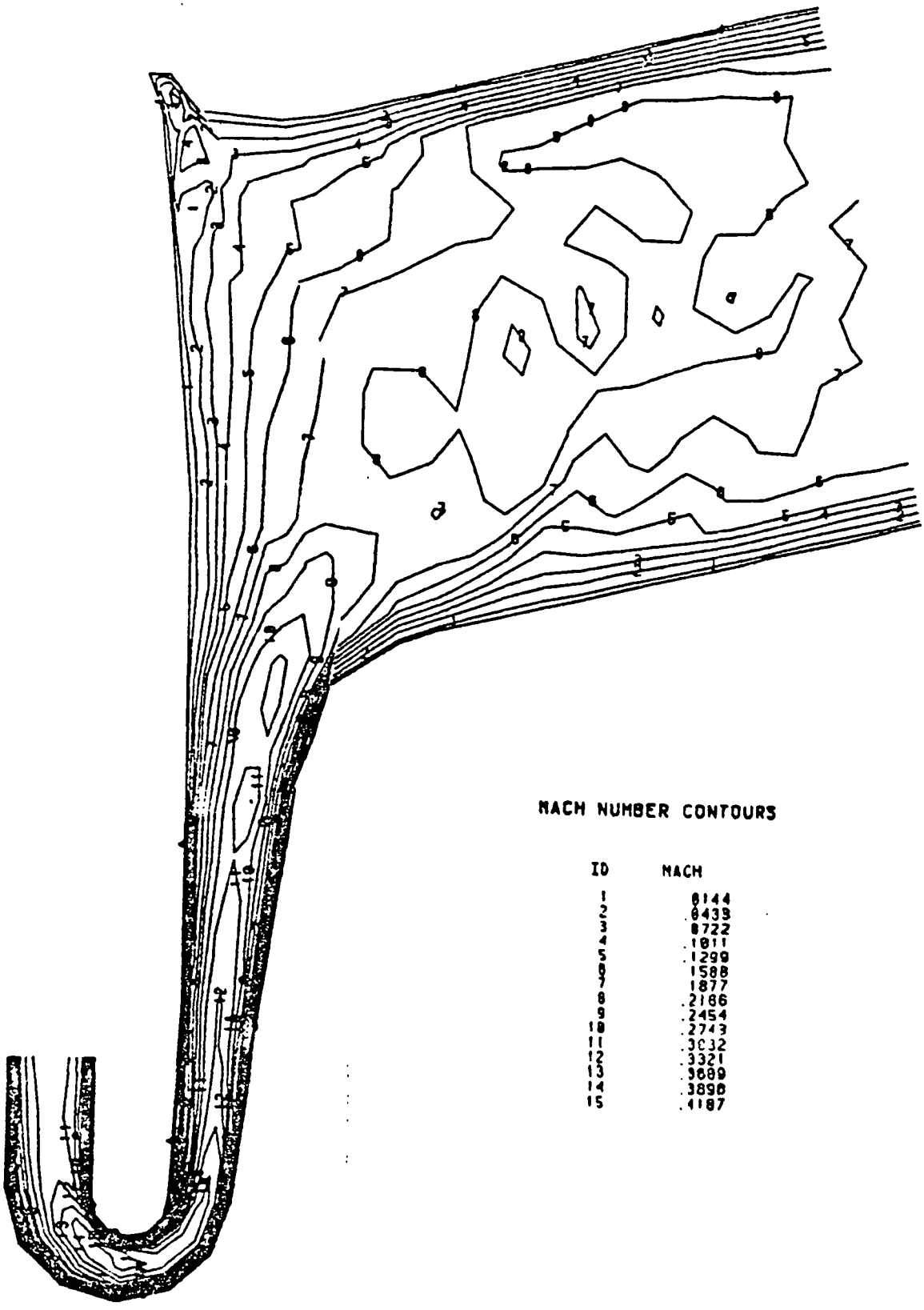

Fig. 57 DFNUS HGM Nominal Configuration Mach Number Contours

C-2

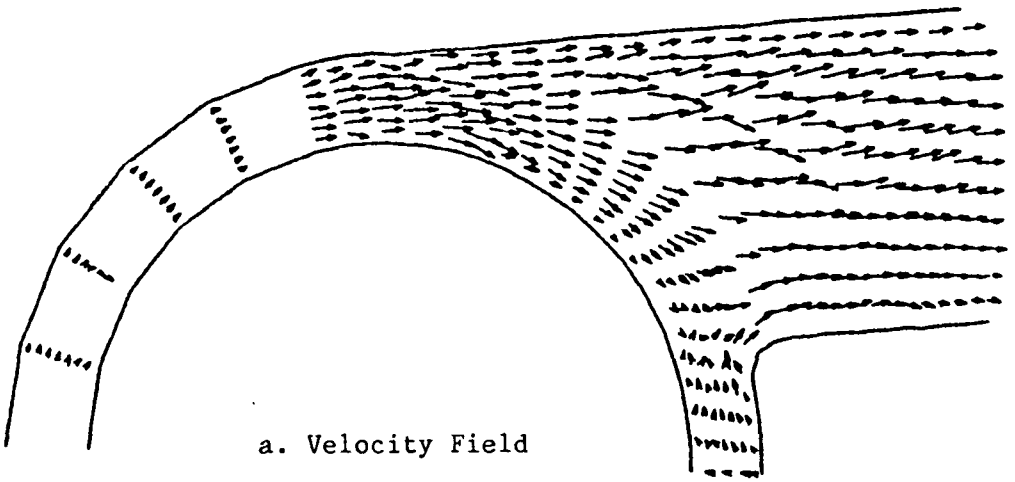

a. Velocity Field

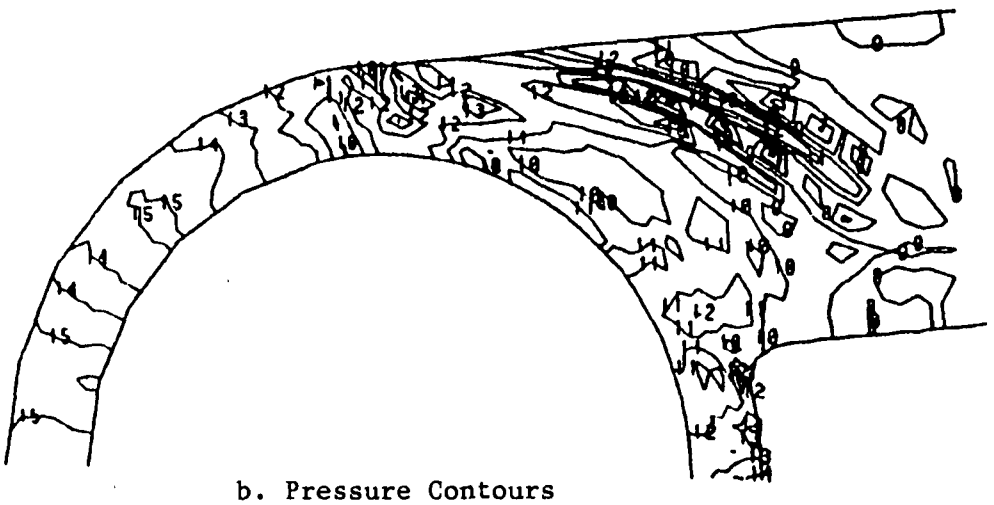

b. Pressure Contours

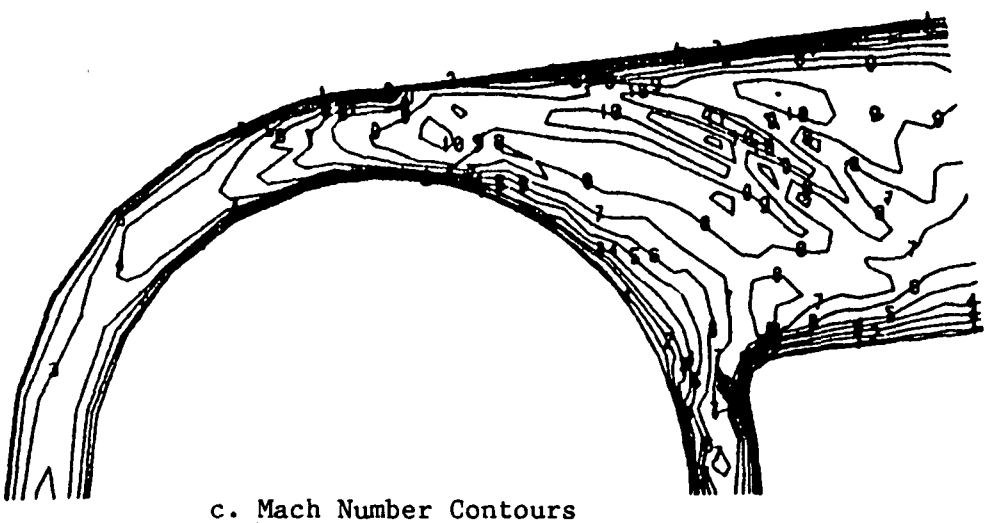

c. Mach Number Contours

Fig. 58 DFNUS HGM Nominal Configuration Bowl - Transfer Duct Flow Field

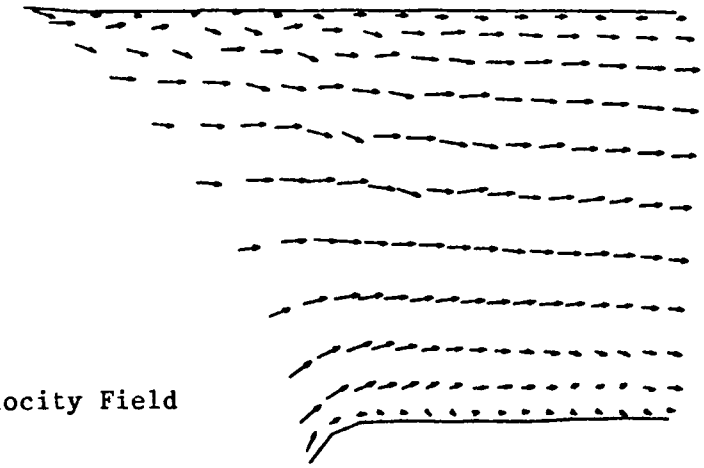

a. Velocity Field

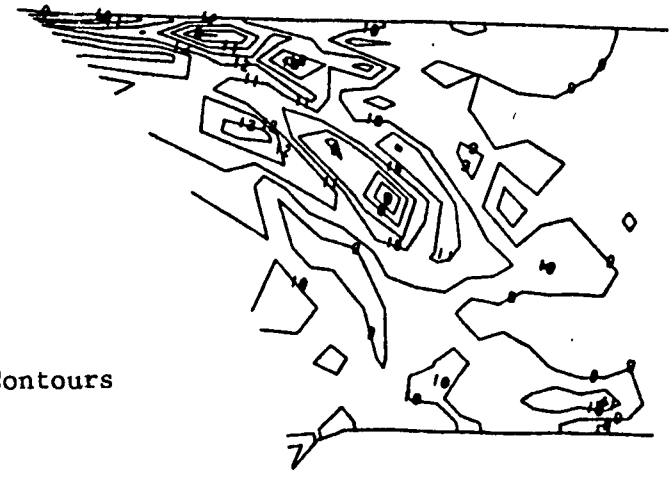

b. Pressure Contours

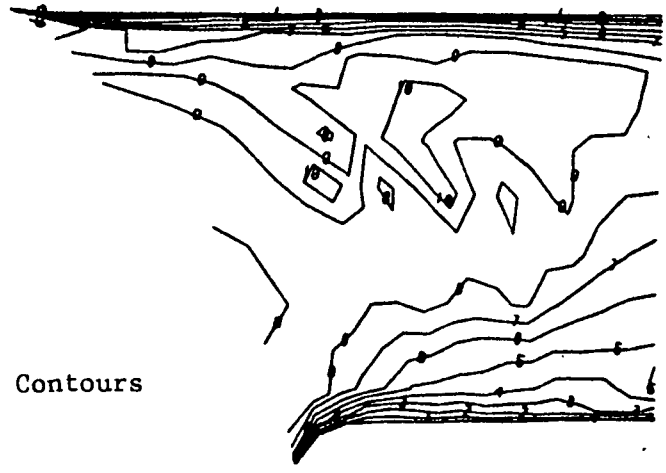

c. Mach Number Contours

Fig. 59 DFNUS HGM Nominal Configuration Bowl - Transfer Duct Flow Field

Figures 60 through 62 present an overall view of velocity vectors, static pressure and Mach number, respectively, in the bowl and turnaround duct as viewed from the side and slightly above. The information content is similar to that shown for the earlier calculations in an unwrapped view (Figs. 46 through 48), and close examination reveals many similar features in the two sets of figures. It will be noticed that the later contour plots lack the smoothness of the former ones. This smoothness in the earlier calculations was achieved by constantly monitoring the stability of the calculations. Properties at any node which exceeded a given tolerance of deviation from the mean among its surroundings were recalculated by averaging. In contrast to this, the more powerful and more stable multi-cycle finite difference scheme used in the latest calculations made it largely unnecessary to resort to averaging, but by itself did not achieve quite the same smoothness in the results. Secondly, the computational grid in the rear half of the bowl ($90 \leq \varphi \leq 180$) as used in the latest calculations was somewhat coarser than the grid used in the earlier calculations, for reasons of economy.

In Fig. 63 a comparison is made between experimental and computed static and total pressure data as a function of distance along the flow. The experimental data are those for the highest mass flow (i.e., highest Reynolds number) cases as previously compiled in Table 4. The computed data are presented in terms of local maxmimum and minimum values, i.e., all computed results are contained within the bands shown. As mentioned previously in the summary of the experimental effort, the total pressure at the turbine exit (T.E.) used as the upstream boundary condition was estimated since the experimental data at this station must be considered incorrect.

Not surprisingly, but believed to be in agreement with general engineering knowledge, the relatively highest total pressure loss occurs in the bend of the turnaround duct. The computed pressure loss from the exit of the turnaround duct (TADE) to the bowl inlet (B.I.) appears to be

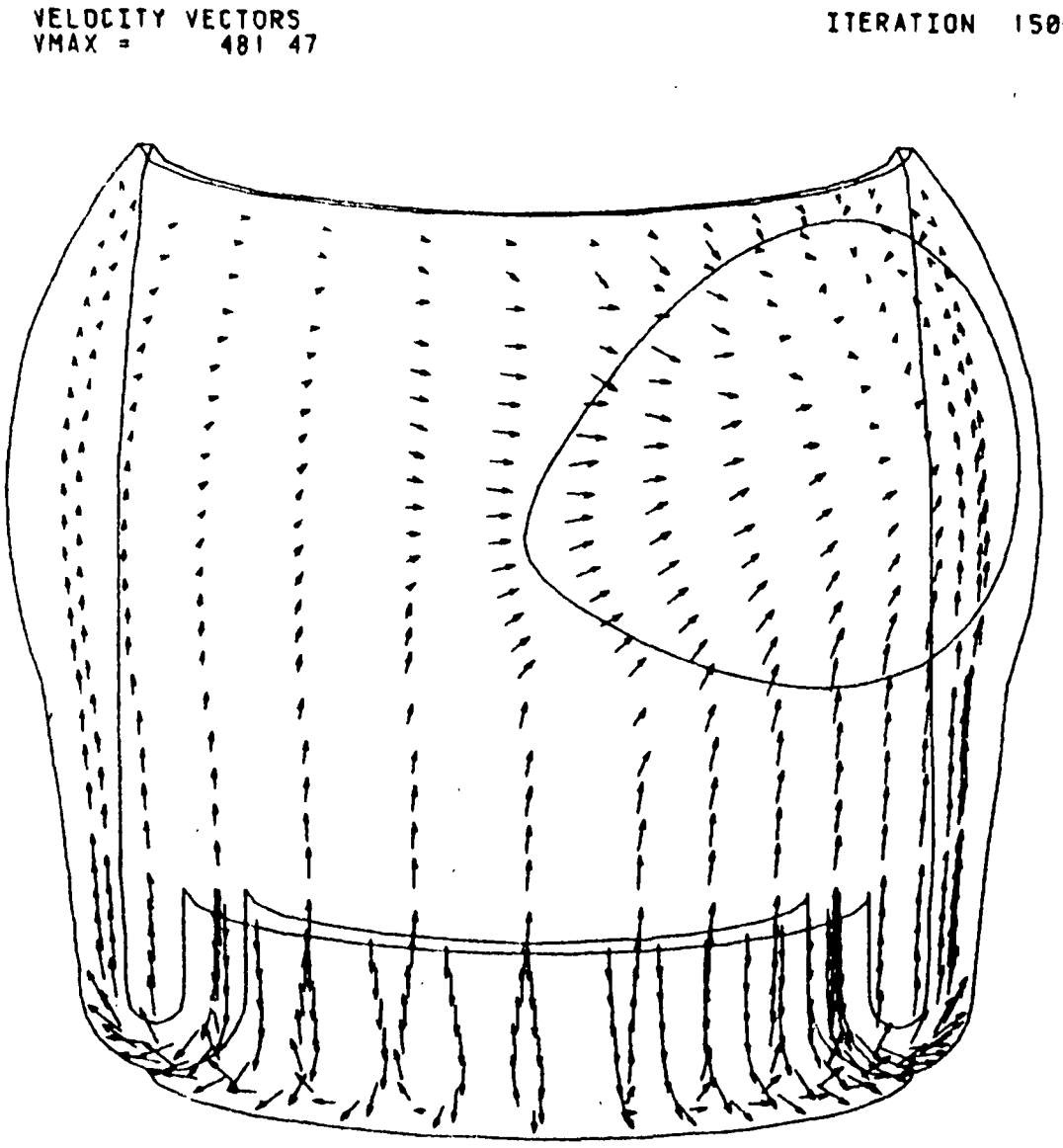

Fig. 60 DFNUS HGM Nominal Configuration Flow Field

ID	P/P0	
1	21770	7750
2	22163	2745
3	22546	7740
4	22930	2735
5	23313	7730
6	23697	2724
7	24080	7719
8	24464	2714
9	24847	7709
10	25231	2704
11	25614	7699
12	25998	2694
13	26381	7689
14	26765	2683
15	27148	7678
16	27532	2673
17	27915	7668
18	28299	2663
19	28682	7658
20	29066	2653

Fig. 61 DFNUS HGM Nominal Configuration Pressure Contours

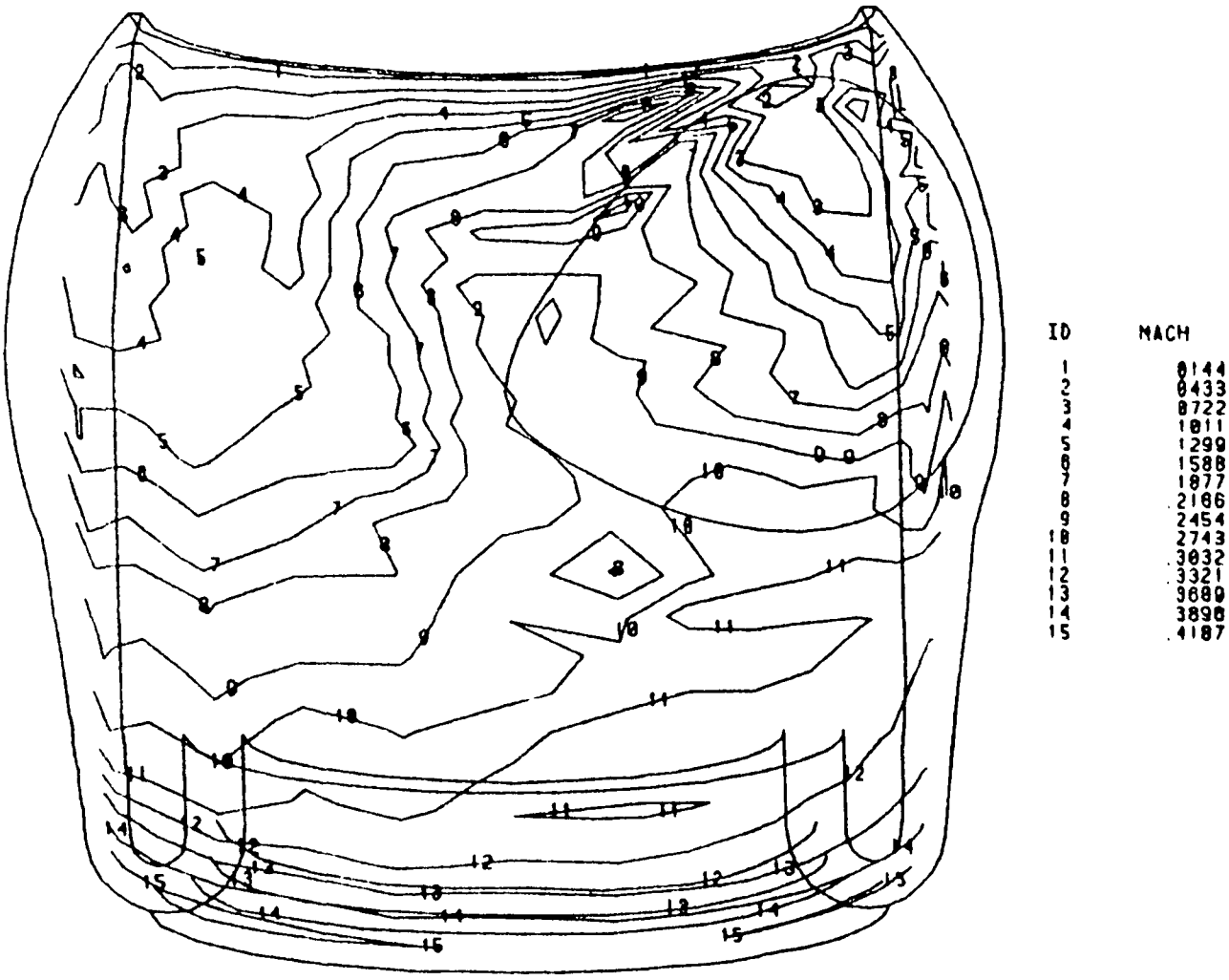

Fig. 62 DFNUS HGM Nominal Configuration Mach Number Contours

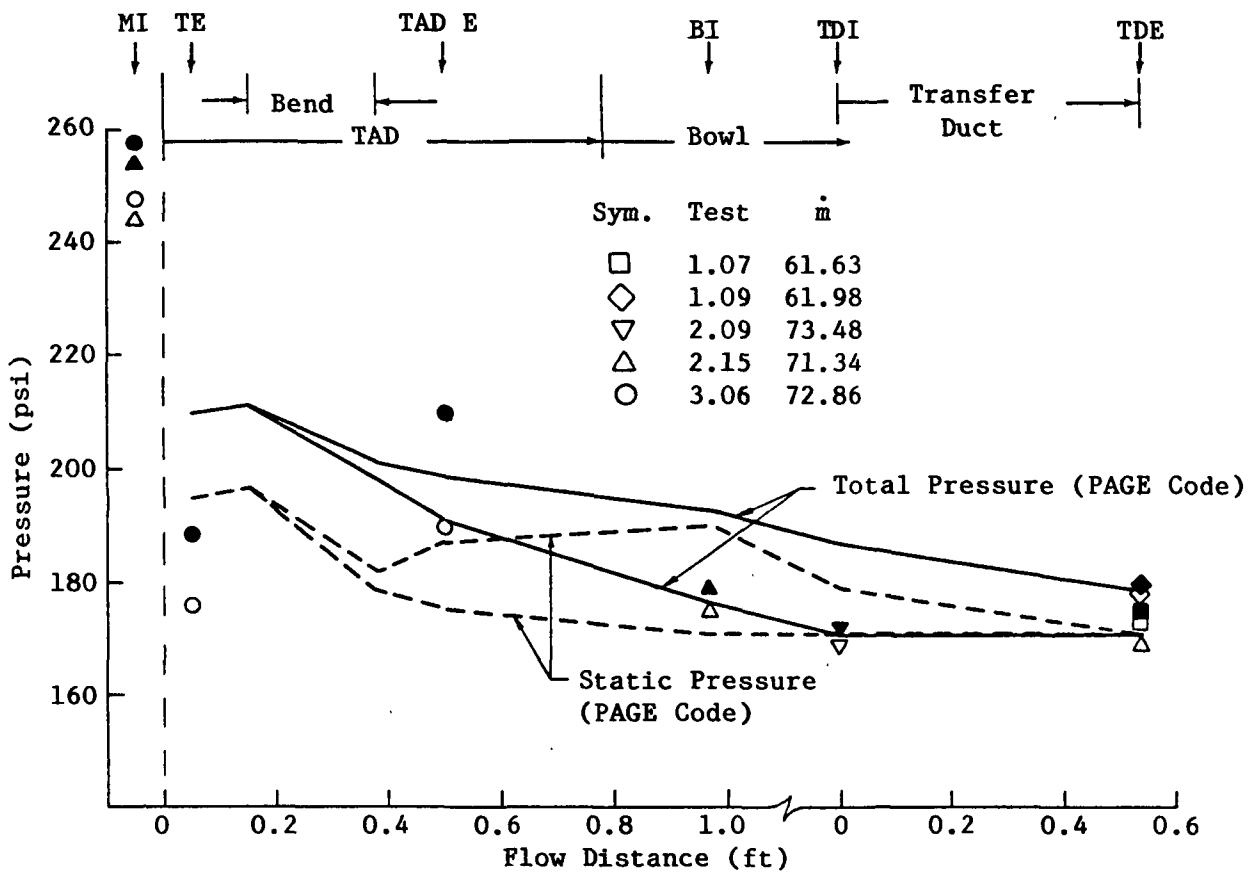

Fig. 63 DFNUS HGM Averaged Pressure Along Flow (Open symbols indicate static pressure; solid symbols indicate total pressure).

Legend:

MI = Model inlet
TE = Turbine exit
TAD E = Turnaround duct exit
BI = Bowl inlet
TDI = Transfer duct inlet
TDE = Transfer duct exit

smaller than that indicated by the experimental data. From there to the transfer duct exit (T.D.E.) the computed pressures are roughly in line with the experimental data. The overall computed total pressure loss from the turbine exit to the transfer duct exit lies between 15 and 19 percent (of the assumed initial total pressure), and between 33 and 50 percent of this loss occurs in the turnaround duct.

Next, computed circumferential pressure distributions at the turnaround duct exit are compared with experimental data and the pressure distributions assumed as upstream boundary condition in the earlier calculations. Figure 64 shows that the computed static pressure distribution straddles both the experimental data and the previously assumed linear distribution with the maximum at the back side of the manifold and the minimum at the front side between the transfer ducts.

The corresponding computed total pressure distribution is shown in Fig. 65. Note that the total pressure is practically constant over the front side of the bowl displaying a small increase toward the back side.

Both distributions display noticeably larger oscillations on the back side of the bowl ($90 \leq \varphi$ 270) than on the front side ($270 \leq \varphi < 90$) due to the already mentioned coarse grid on the back side, especially in the circumferential direction. Nevertheless, the results do seem to justify the previously adopted assumption that the effects of the flow in the turnaround duct on the flow in the bowl and transfer duct can be simulated (without including the turnaround duct) by using appropriate upstream boundary conditions.

Circumferential distributions of static and total pressure at the bowl inlet (a cross-section just passing through the lower edge of the transfer ducts) are again compared with experimental data in Figs. 66 and 67. The computed results are seen to follow the trend of the experimental data. In spite of the oscillations from grid plane to grid plane in the

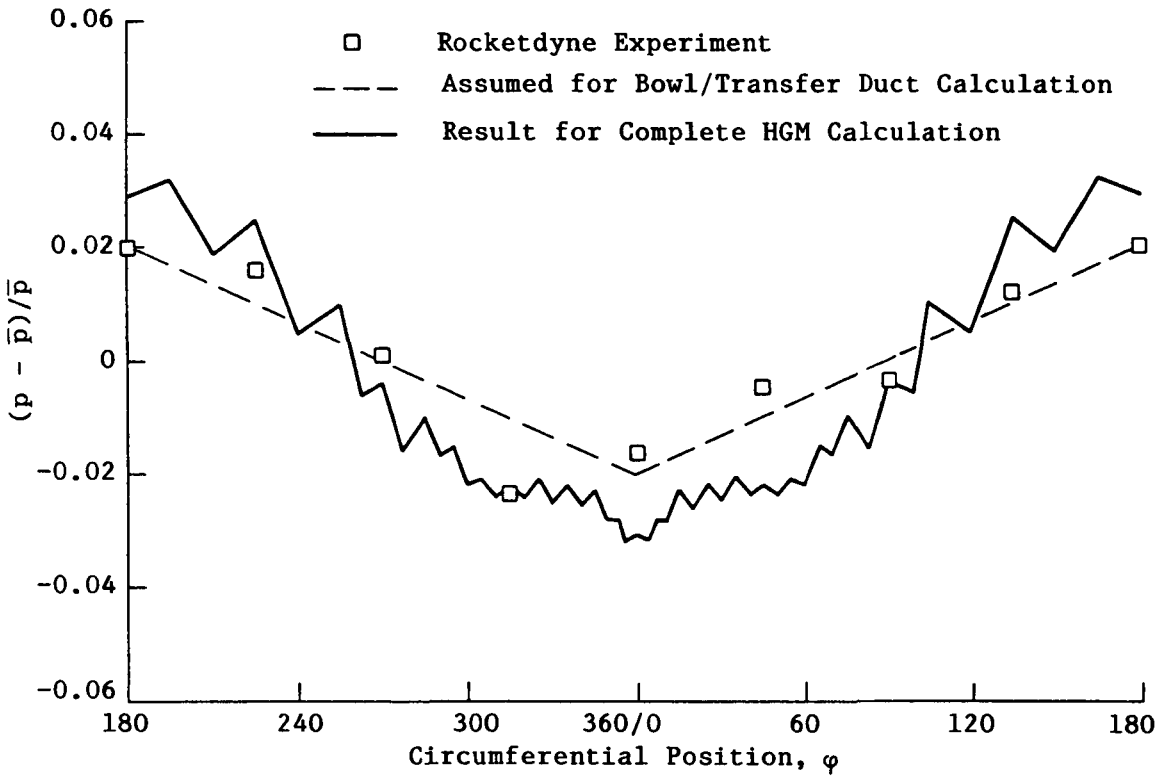

Fig. 64 Turnaround Duct Exit Static Pressure Distribution

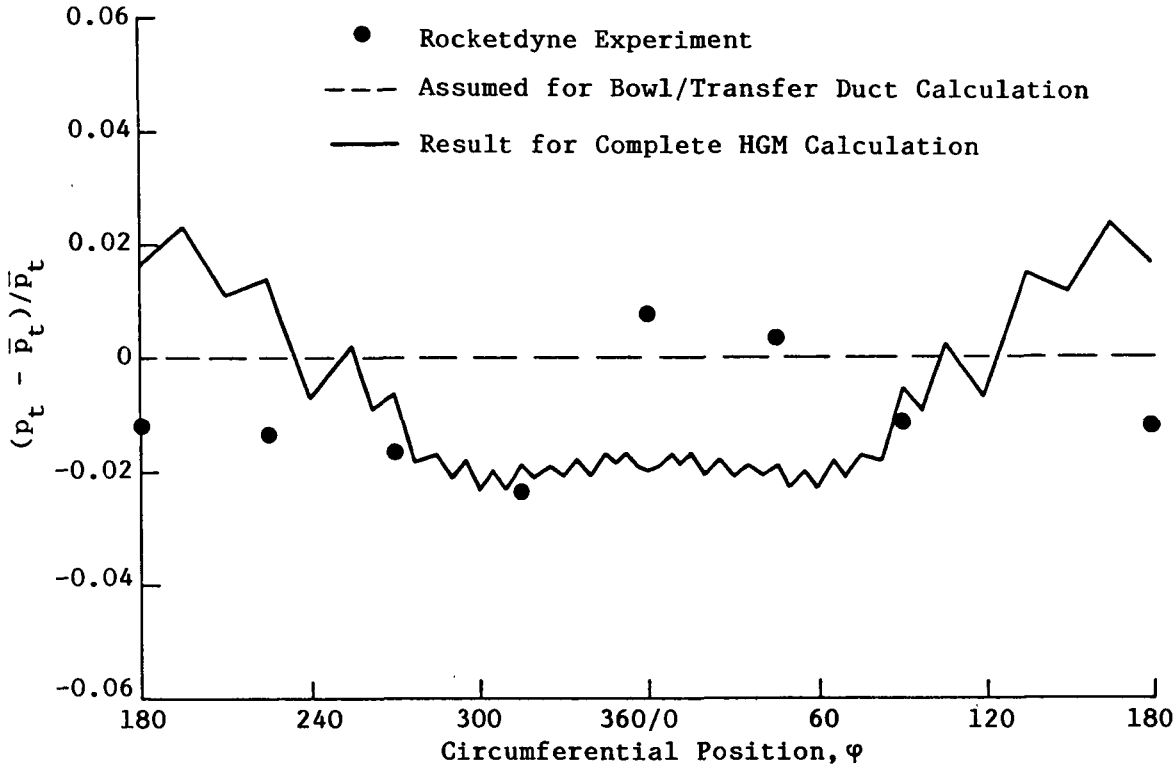

Fig. 65 Turnaround Duct Exit Total Pressure Distribution

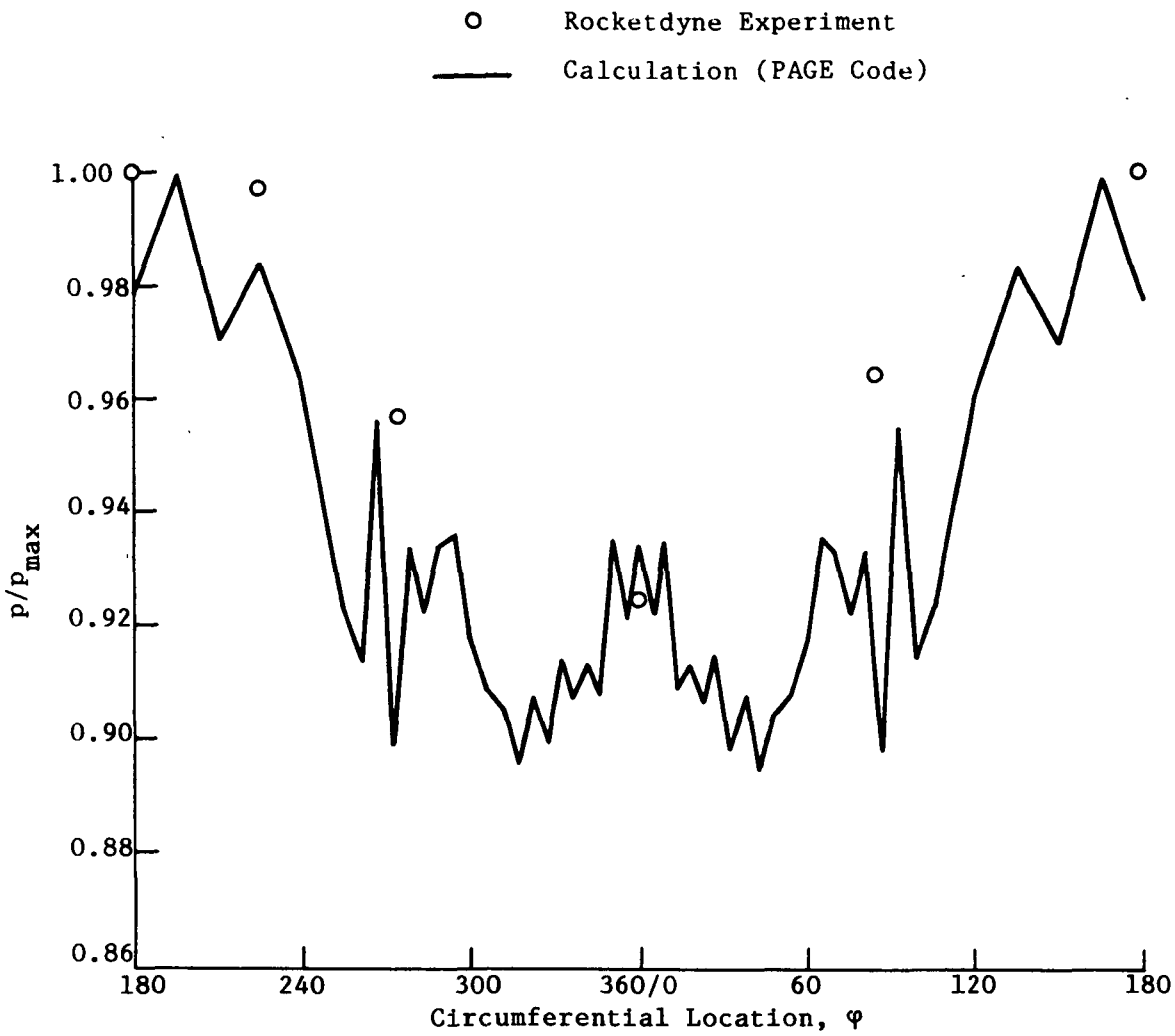

Fig. 66 DFNUS HGM, Bowl Inlet Static Pressure

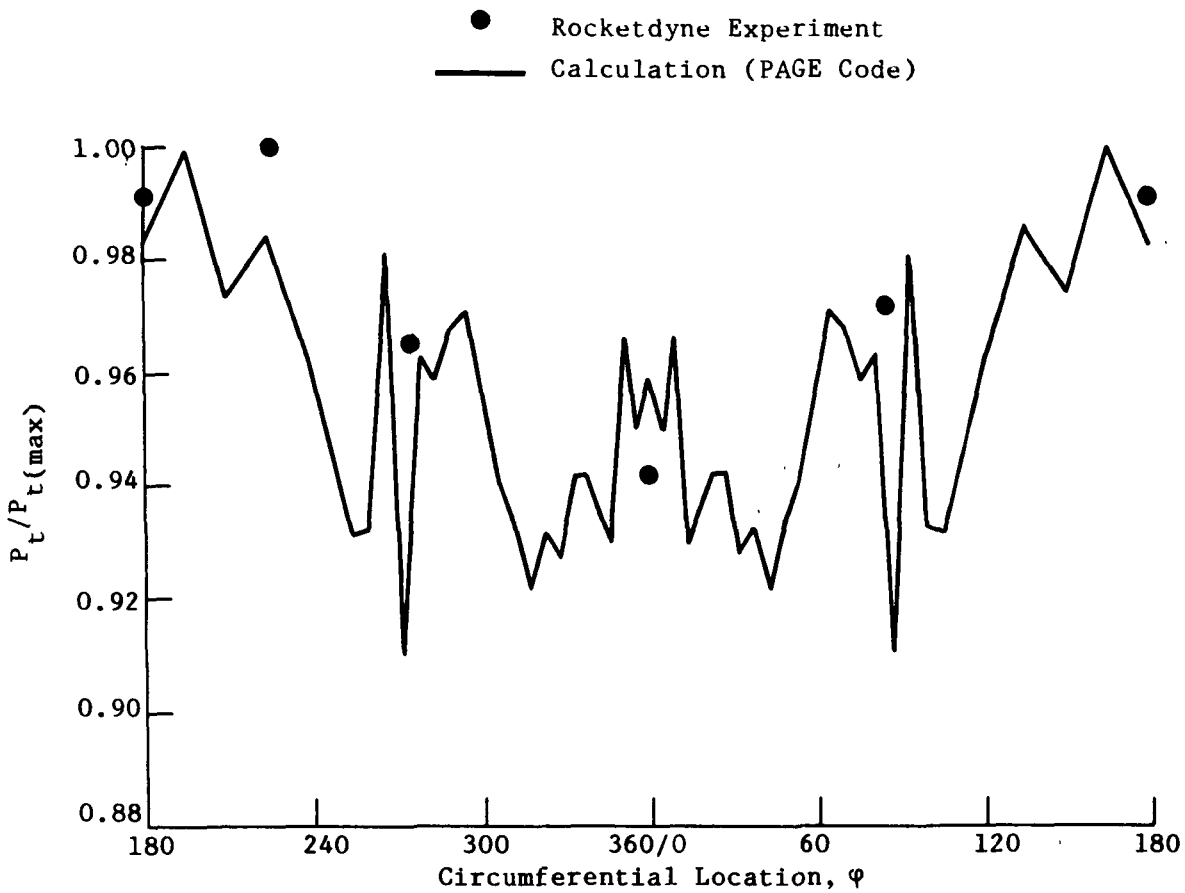

Fig. 67 DFNUS HGM, Bowl Inlet Total Pressure

circumferential direction, the expected minima in the static pressure just upstream of the turn into the transfer duct ($\varphi \approx 45$ deg) are clearly visible. Both static and total pressure display local maxima between the transfer ducts and absolute maxima on the opposite side of the bowl, in agreement with the experimental data.

As a final comparison between analysis and experiment, Mach number profiles at the transfer duct exit are illustrated in Fig. 68. Dashed and solid curves represent the results from the earlier calculations without the turnaround duct, while the dash-dotted curves represent the results from the analysis of the complete HGM. Neither one of the calculations reproduces the details of the experimental profile. However, qualitatively at least, results from the later calculations do indicate a slight minimum near the duct center, so prominently displayed in the experimental data.

4.2 CONFIGURATION VARIATIONS

4.2.1 Modified Transfer Duct Inlet

Having demonstrated that available numerical analysis is capable of producing results which agree with experimental data, another goal of the effort undertaken here was to use the analysis to explore changes in the geometric configuration which would result in more favorable flow behavior.

Figures 21 through 24 illustrated a computational grid of the hot gas manifold incorporating a greatly increased radius of curvature of the transfer duct inlet fairing, especially in the region just upstream of the duct flow separation region found in both analytical and experimental studies of the nominal HGM configuration. Neither the transfer duct location, nor its orientation nor its size was affected by this modification. Flowfield calculations for the modified configuration were then performed using initial and boundary conditions identical to those previously used for the nominal configuration.

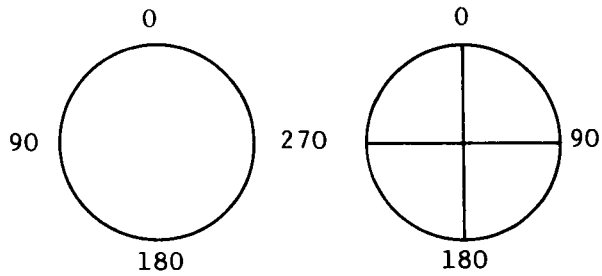

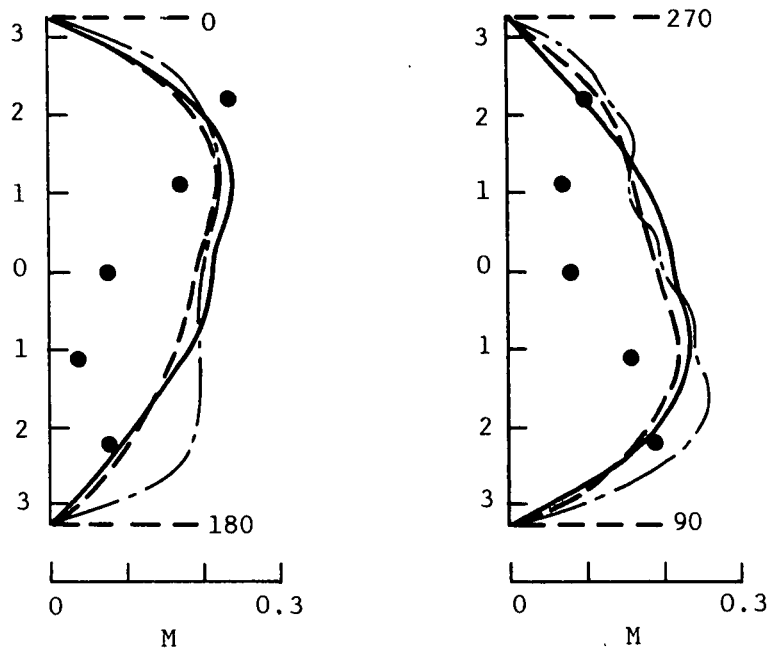

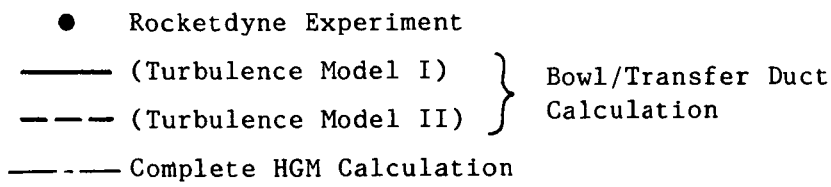

Fig. 68 Transfer Duct Exit Mach Number Profiles

Results are shown in Figs. 69 through 75. Figure 69 gives the same overall view of the HGM flow field as shown for the unmodified manifold in Fig. 51. Note the absence of any flow recirculation in the present case. Details of the velocity vector plots and Mach number contours in the oblique longitudinal cut through the transfer duct are compared in Figs. 70 through 73 for the two configurations. Hence, a significant result of decreasing the curvature in the transfer duct inlet fairing is the elimination of flow separation in the duct.

The effect of the transfer duct inlet modification on the duct exit flow properties is shown in terms of relative static and total pressure profiles across the duct exit plane. Figure 74 shows a significant reduction in static pressure nonuniformity, and the same holds for the total pressure distribution shown in Fig. 75.

Flow visualization experiments as well as computational analyses have shown certain swirl patterns to exist in the transfer ducts. Although the present relatively coarse grid analysis shows good agreement with experimental pressure distributions we believe that it is not accurate enough to predict swirl patterns reliably. Nevertheless, an attempt has been made to compare the swirl encountered in the present analysis for the two HGM configurations in terms of the ratio of average cross flow to average axial flow along the transfer duct. The results, displayed in Fig. 76, show that, in the transfer duct inlet region, swirl is somewhat higher for the modified inlet configuration. In the cylindrical portion of the ducts, however, the situation is reversed. At the duct exit, swirl in the modified duct is found to be almost 35 percent lower than that calculated for the nominal duct.

4.2.2 Turnaround Duct Variations

A limited study was performed to explore the effect of slight changes in the geometry on the flow properties in the turnaround duct relative to

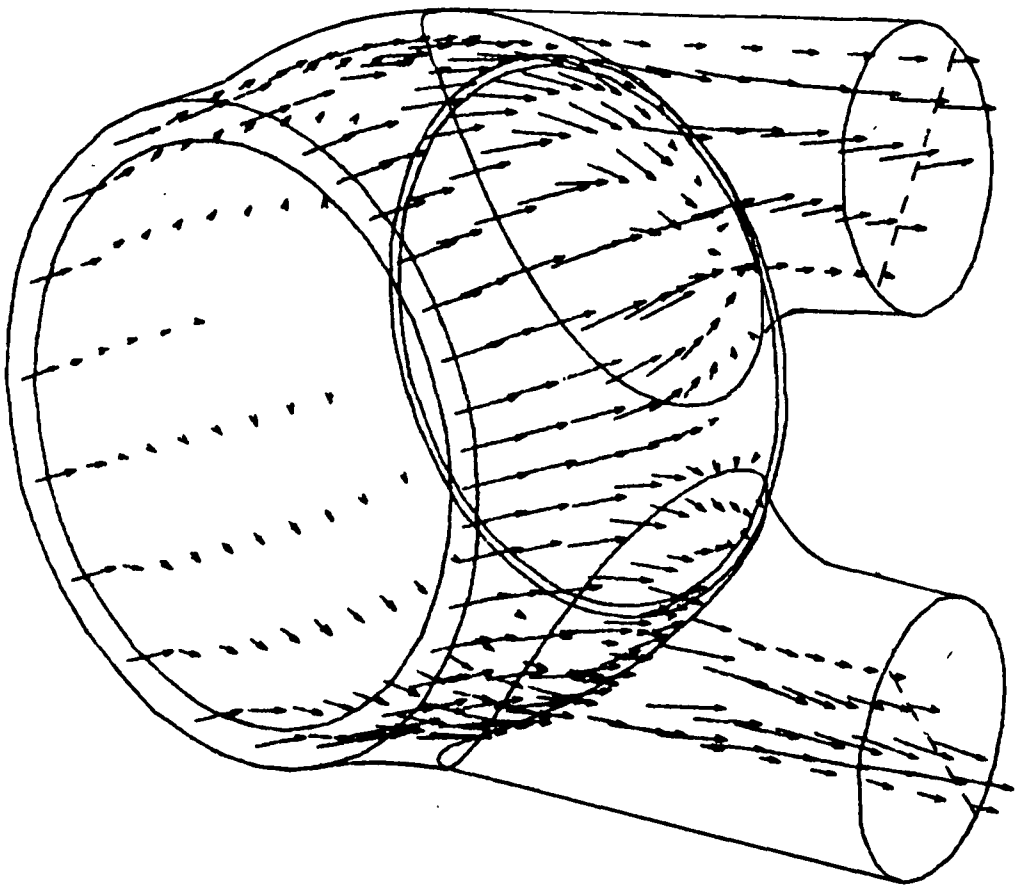

Fig. 69 Modified HGM Bowl and Transfer Duct Flow Field

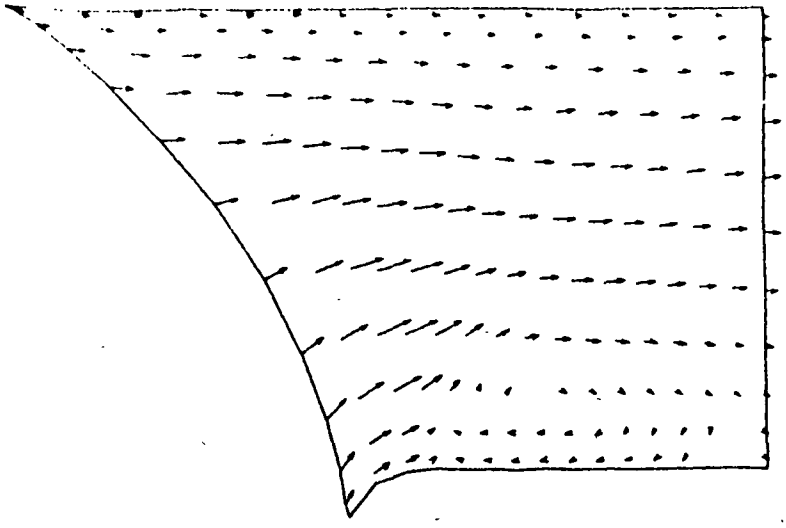

Fig. 70 Nominal HGM Transfer Duct Flow Field

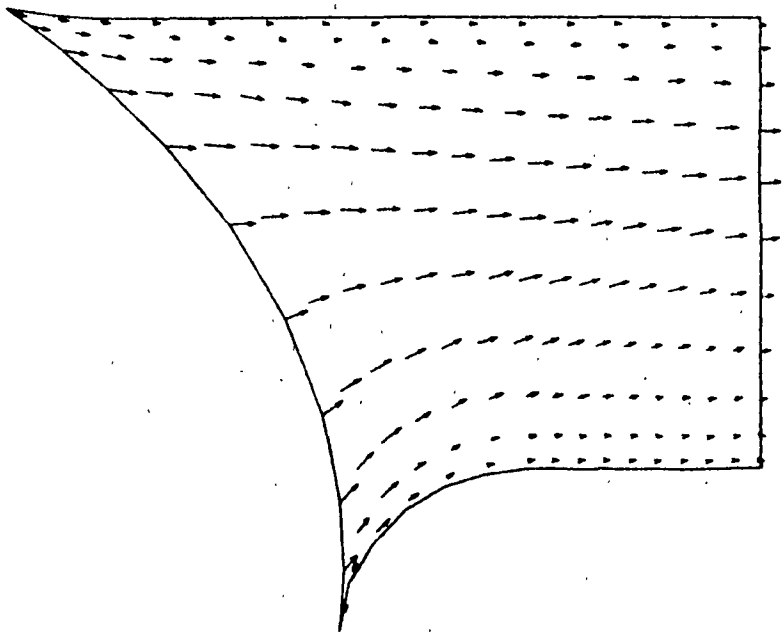

Fig. 71 Modified HGM Transfer Duct Flow Field

ORIGINAL PAGE IS
OF POOR QUALITY

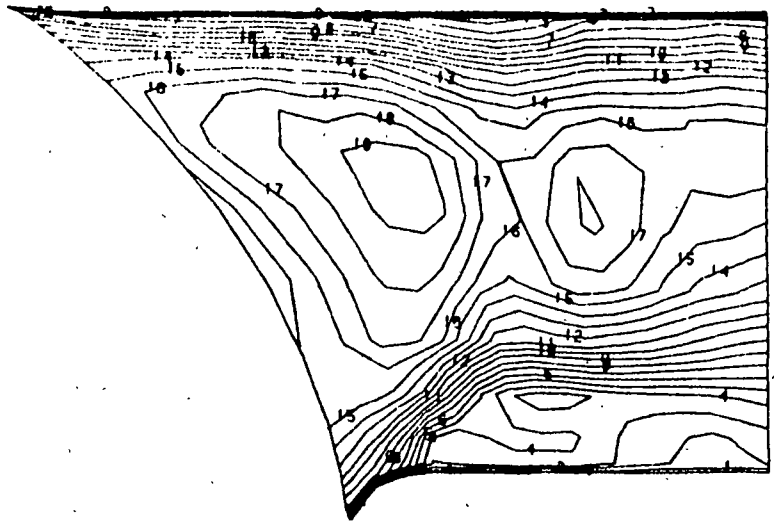

Fig. 72 Nominal HGM Transfer Duct Mach Contours

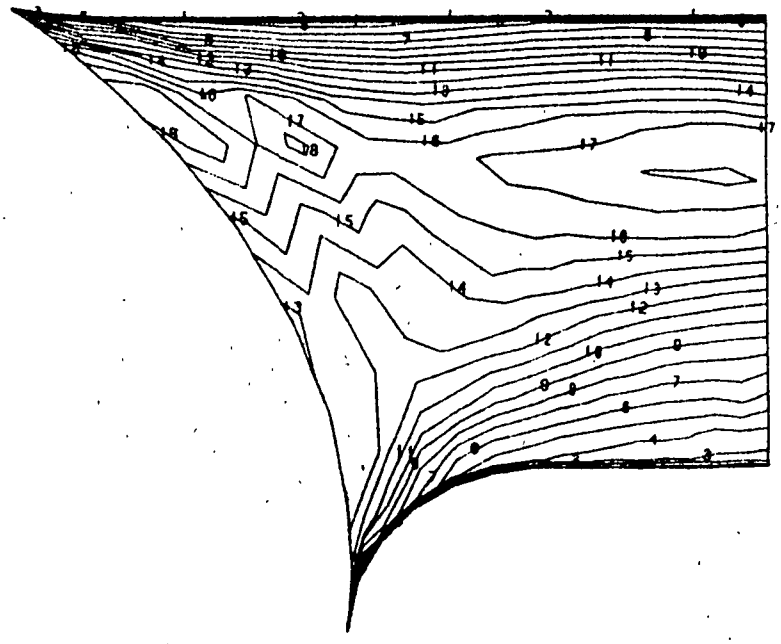

Fig. 73 Modified HGM Transfer Duct Mach Contours

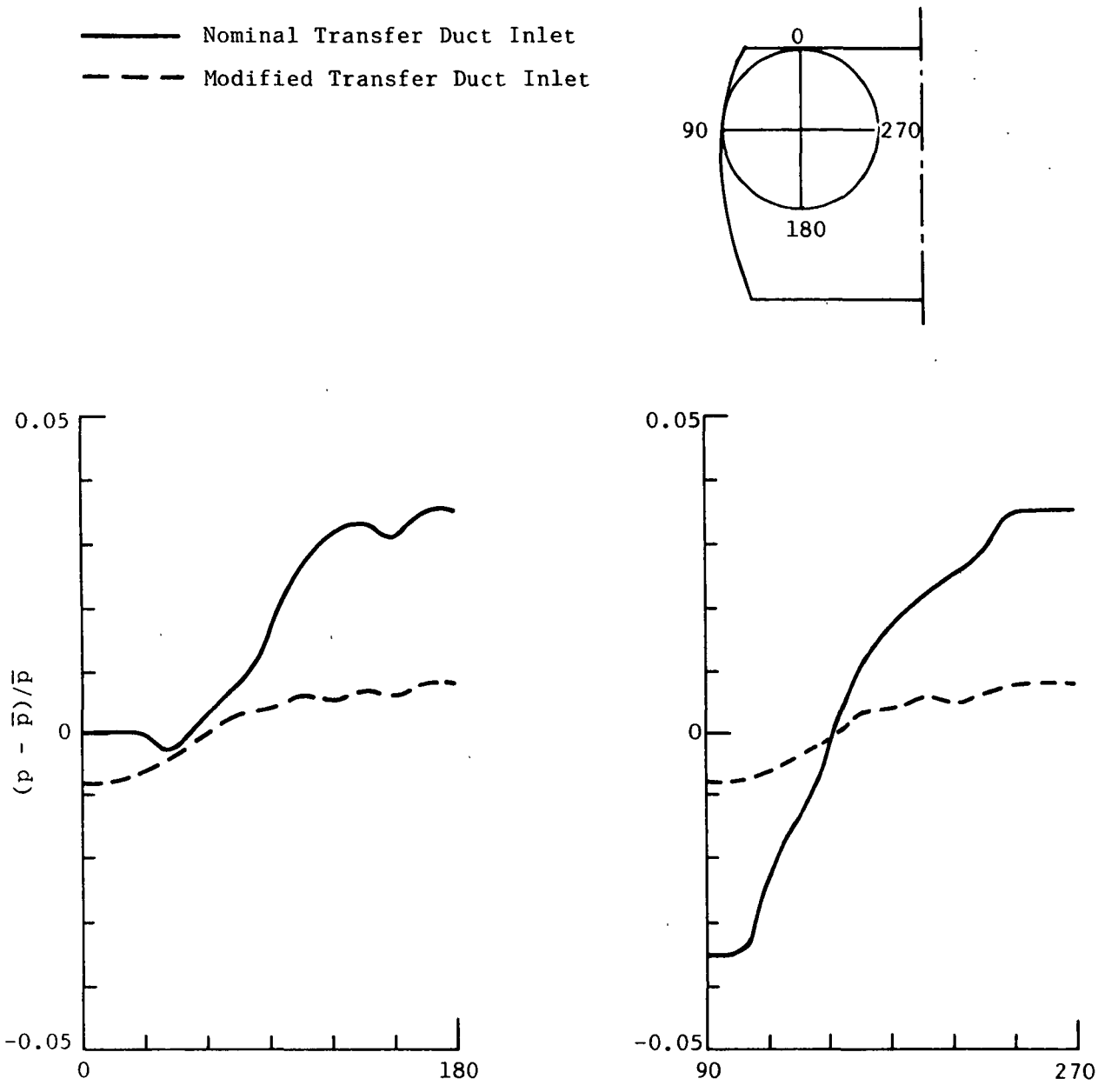

Fig. 74 Transfer Duct Exit Static Pressure Profile

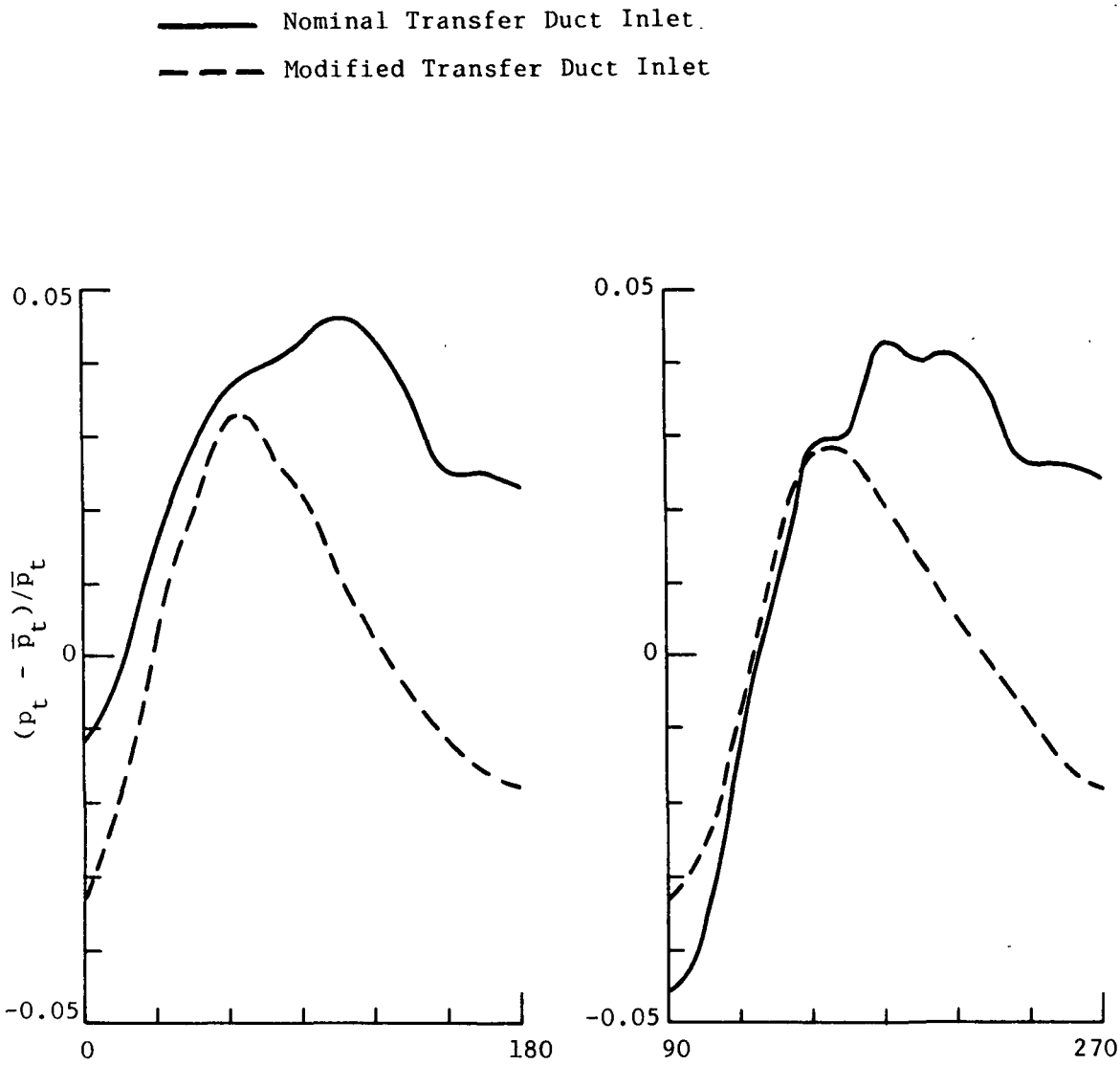

Fig. 75 Transfer Duct Exit Total Pressure Profile

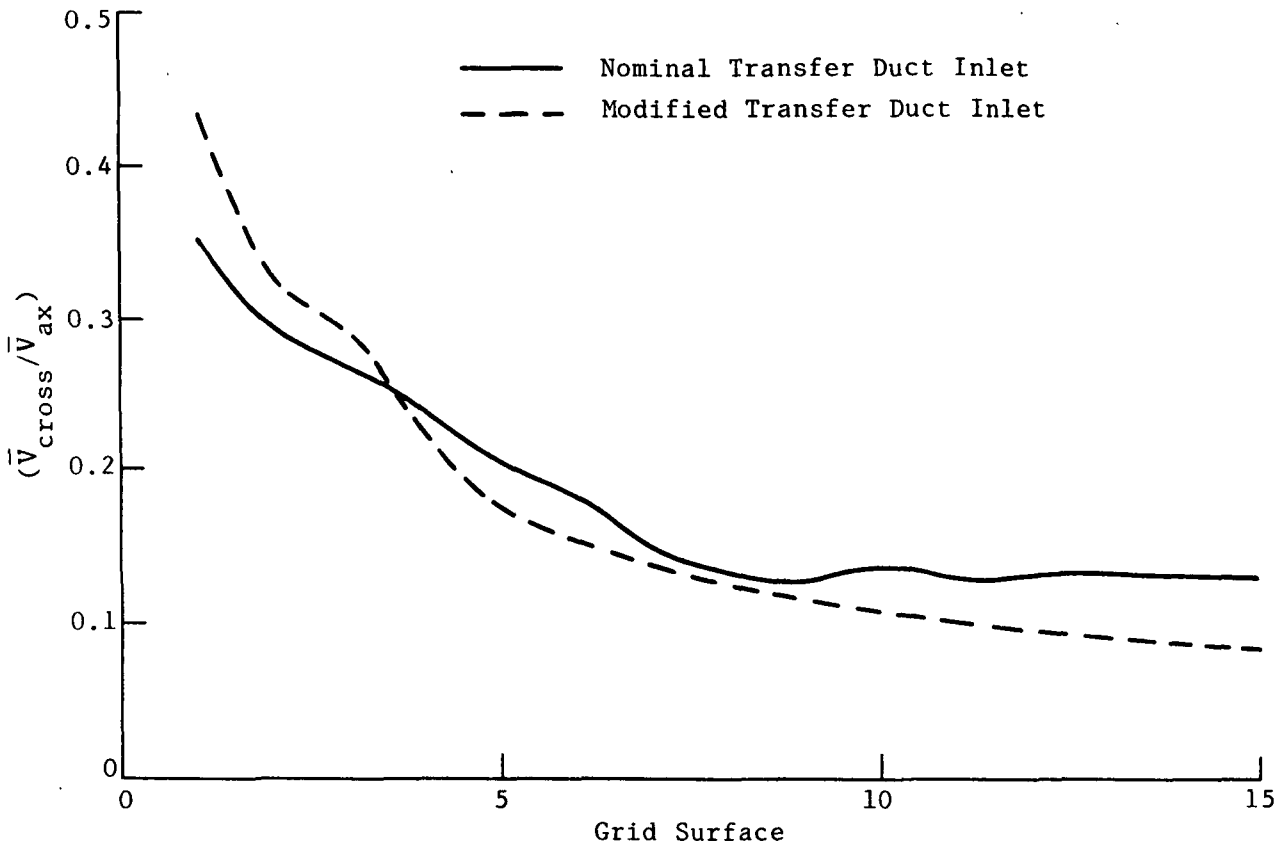

Fig. 76 Twin Duct HGM - Ratio of Average Cross Flow to Average Axial Flow Along Transfer Duct

the nominal DFNUS turnaround duct configuration. The changes implemented affected mainly the wall contours in the 180 deg bend while the dimensions of the inflow and outflow cross-section were held at the values for the nominal duct.

The modified geometries are compared to the nominal geometry in Fig. 77. The first change implemented (Version 2) was to slightly decrease the curvature of the bend while keeping the cross-sectional distribution versus flow distance near that of the nominal configuration (Fig. 78). For the second change (Version 3) we used the outer wall from Version 2 while retracting the inner wall so as to open up the narrowest passage in the bend. The result is also shown in Fig. 78, indicating an increasing flow area through most of the bend with a local minimum at the exit of the 180 deg turn.

Axisymmetric flowfield calculations were performed using 510 nodes in the grid plane. Inflow and outflow boundary conditions were specified in terms of inlet total pressure and exit static pressure, and were the same for all three cases. A relatively high effective viscosity was used to simulate turbulent flow resulting in a calculated mass flow at approximately 50 percent of the experimental value. The viscosity was the same for all three cases.

Velocity vector plots are compared in Fig. 79. Differences between the three cases are very subtle and hardly noticeable. Some slight quantitative differences can be detected in the static pressure contours shown in Fig. 80. The most noticeable effect appears in the Mach number contour plots shown in Fig. 81. For the first two cases the highest velocity is found in the second half of the bend, i.e., just downstream of the narrowest flow passage. In contrast, for Case C, the flow velocity is much more uniform throughout the bend reaching a maximum just downstream of the 180 deg turn.

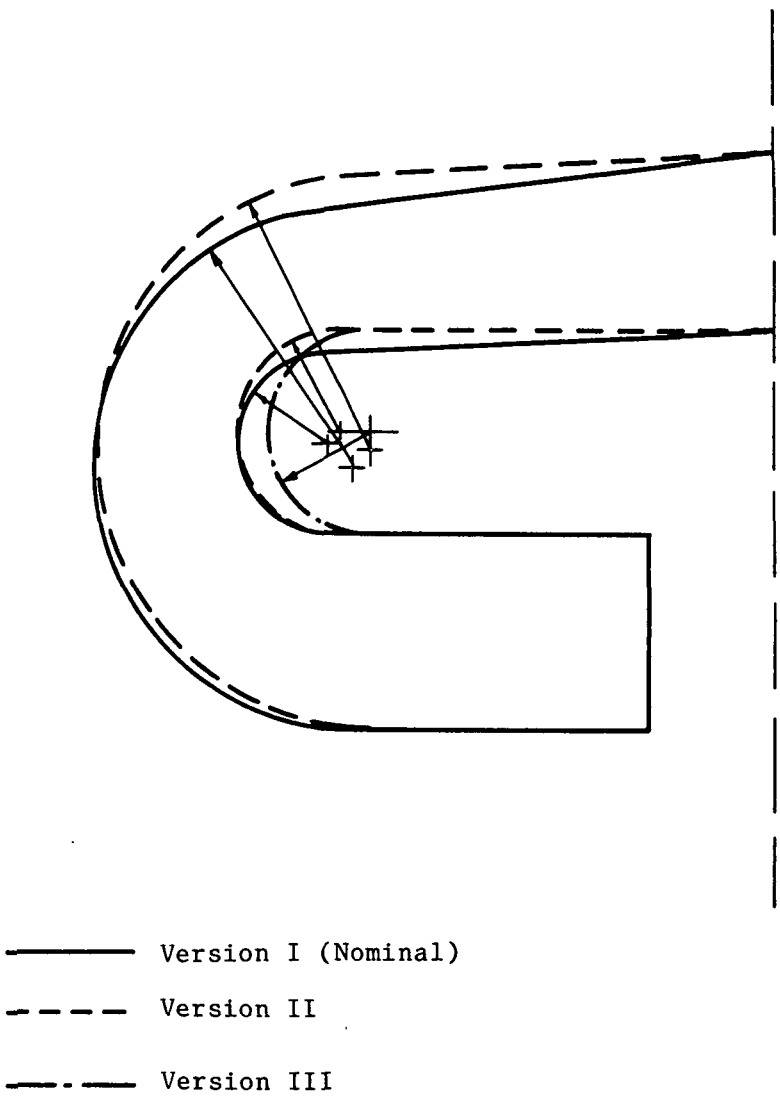

Fig. 77 Turnaround Duct Variations

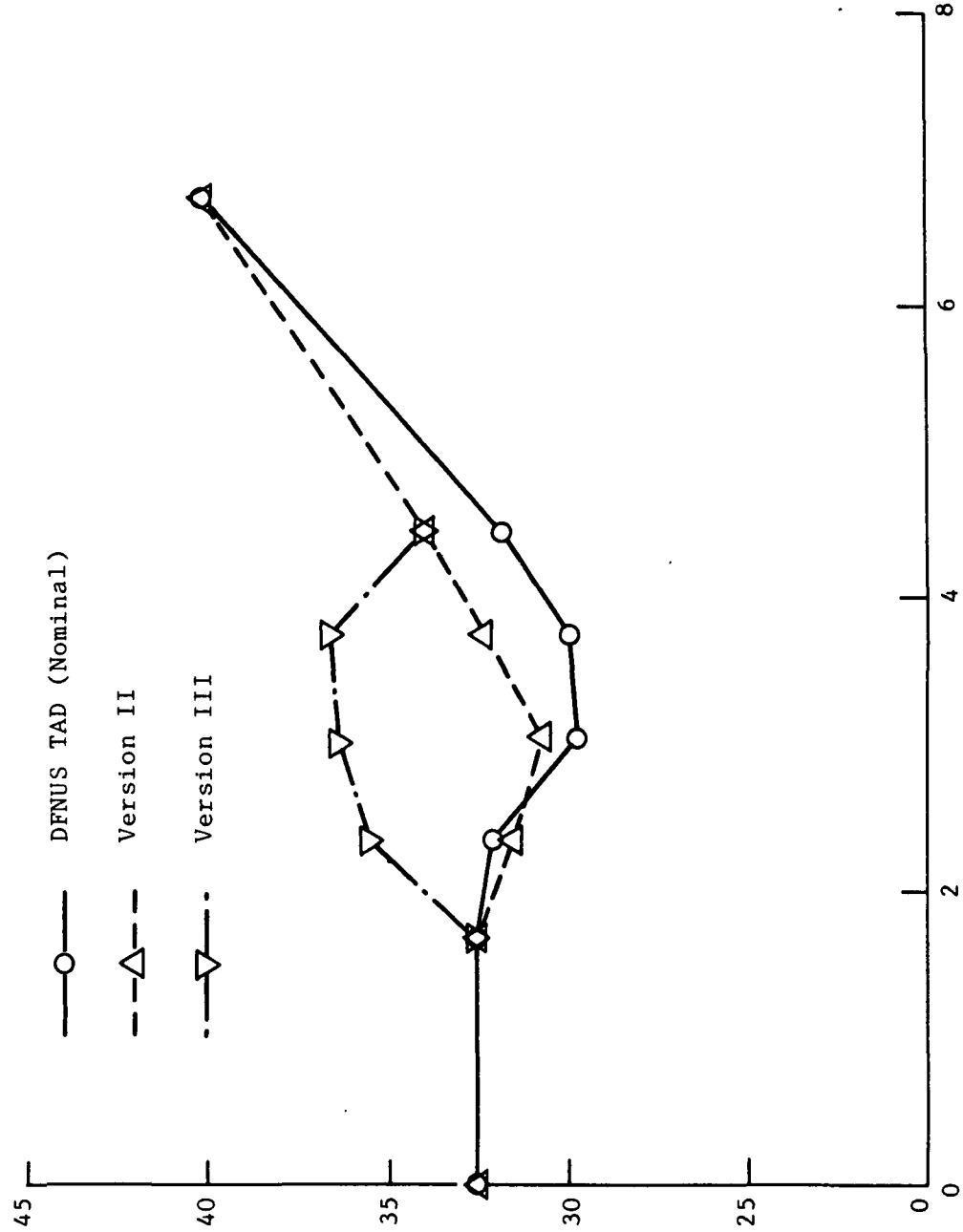

Fig. 78 Turnaround Duct Cross-Sectional Area Variations

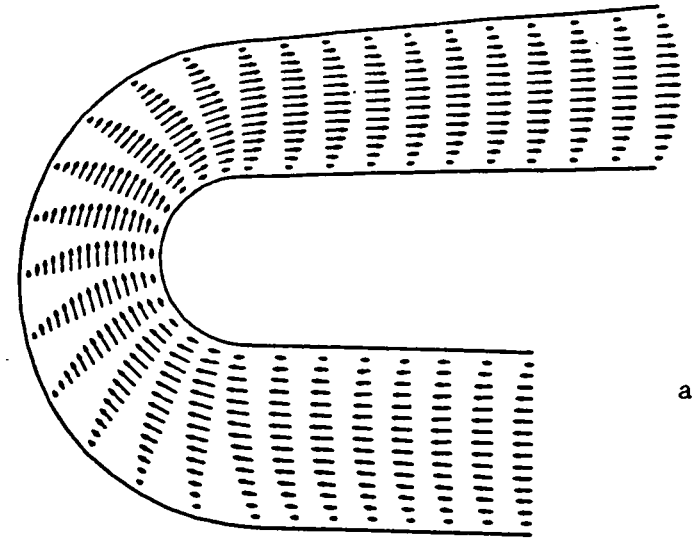

a. Nominal DFNUS

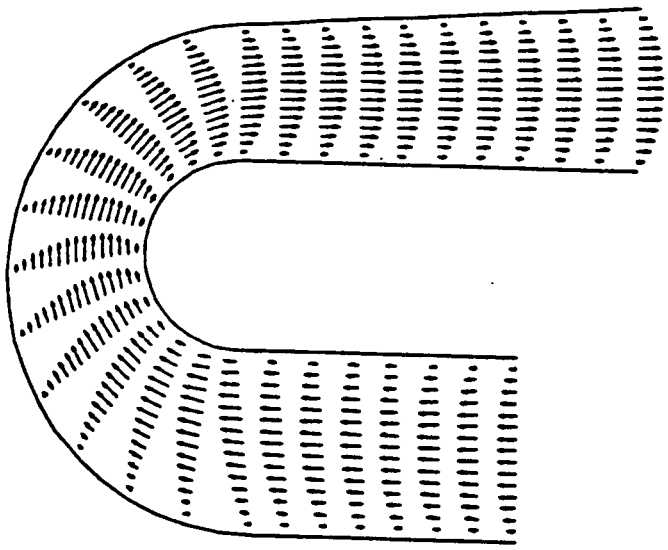

b. Version II

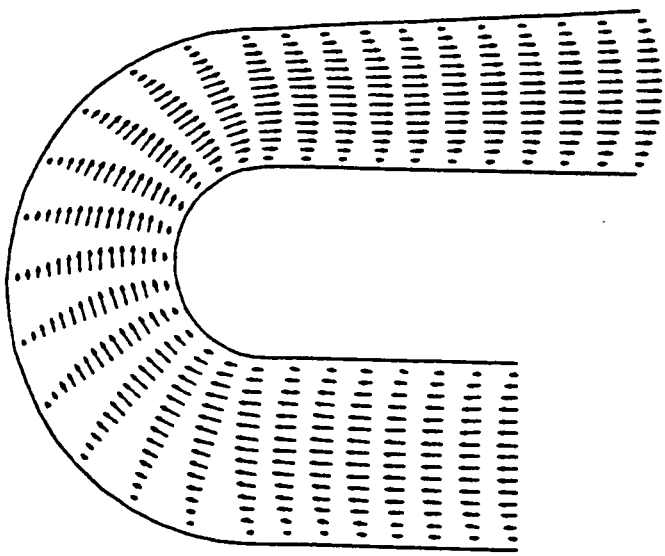

c. Version III

Fig. 79 Axisymmetric Turnaround Duct Variations, Velocity Vectors

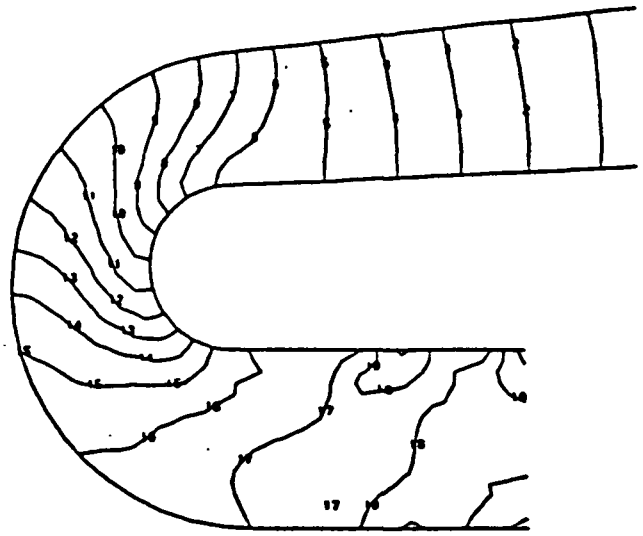

a. Nominal DFNUS

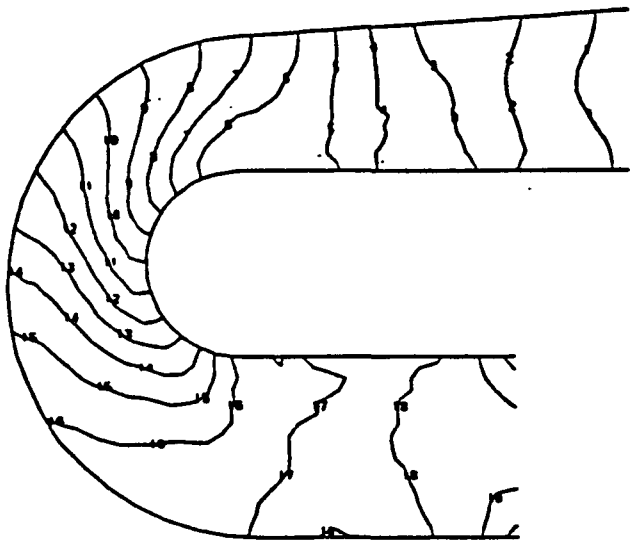

b. Version II

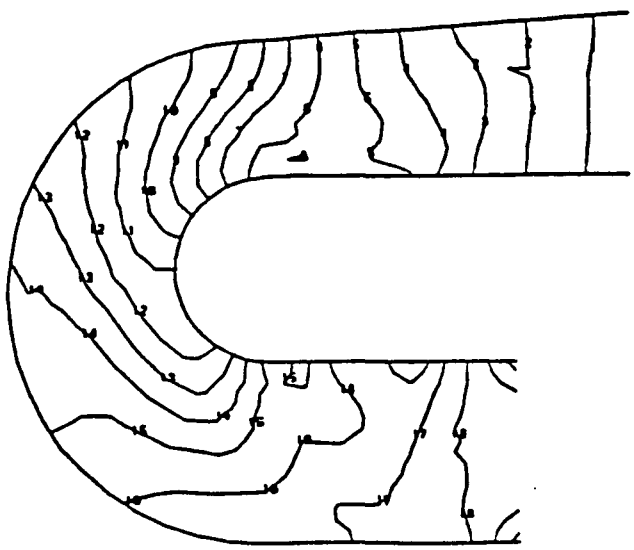

c. Version III

Fig. 80 Axisymmetric Turnaround Duct Variations, Static Pressure Contours

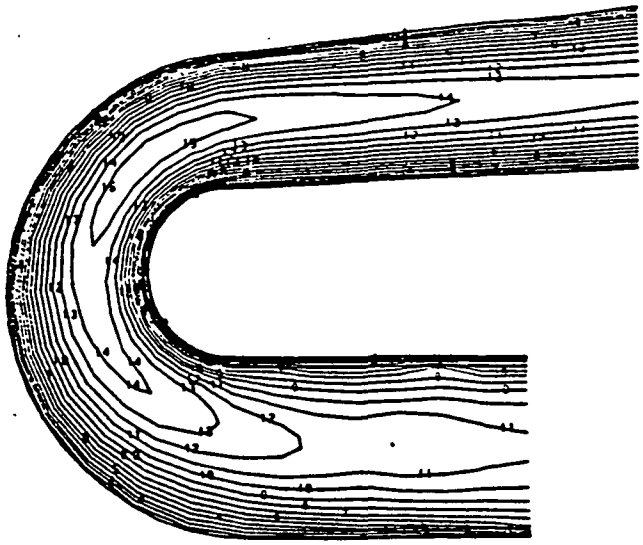

a. Nominal DFNUS

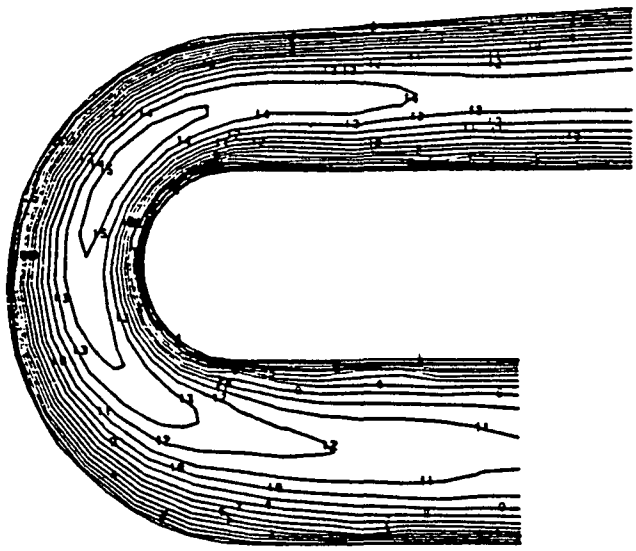

b. Version II

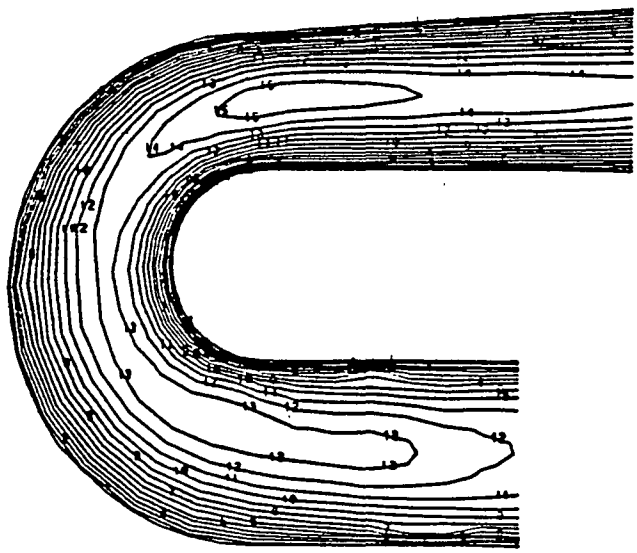

c. Version III

Fig. 81 Axisymmetric Turnaround Duct Variations, Mach Number Contours

Table 6, in which some numerical results are compared, indicates that the static pressure gradient is practically the same for all three cases. In terms of mass flow, however, version 3 allows a 14 percent higher mass flow relative to the nominal duct, at the same pressure gradient and viscosity. It is concluded, therefore, that opening up the flow passage in the turn where the highest flow losses are to be expected results in a more efficient configuration. This is a preliminary conclusion and should be explored further in the future.

Table 6 RESULTS OF TURNAROUND DUCT VARIATIONS

Case	$-\frac{p}{p_{inlet}}$	$\dot{m}$	$\frac{\dot{m}}{\dot{m}_{nominal}}$
Nominal	0.2312	32.3	1.0
Version 2	0.2317	32.8	1.015
Version 3	0.2320	36.9	1.142

5. CONCLUSIONS

It was experimentally demonstrated that a new twin-duct SSME high pressure fuel turbopump hot-gas manifold yields improved flow uniformity as compared to the original three-duct design. This advanced HGM design shows promise in leading to longer life and higher power level versions of the SSME.

Major flow improvements were accomplished in the turbine exit/turnaround duct region by increasing the annular path cross-sectional area downstream of the 180 deg turn, the fishbowl volume, and by contouring the two larger transfer ducts with the outer fishbowl housing. These increases, in general, decreased the local dynamic pressure and allowed the flow to turn more gradually into the transfer ducts. This substantially reduced the circumferential pressure gradient at the turbine exit and downstream of the 180 deg turn. Although flow separation in the transfer ducts could not be eliminated, it was substantially reduced with the result of much improved flow uniformity at the transfer duct exits.

The Lockheed PAGE code was used to computationally model the new twin-duct HGM and to compare calculated flow field characteristics with experimental data. It was found that computed pressure distributions agreed well with measured circumferential pressure distributions downstream of the 180 deg bend in the turnaround duct and in the fishbowl entrance just below the transfer ducts. Furthermore, the computer model correctly predicted flow separation and flow reversal in the lower inner quadrant of the transfer ducts. The computer model did not reproduce the details of the Mach number distributions in the transfer duct as obtained from experiment. As there are known shortcomings in the model as well as known uncertainties about the validity of these particular measurements, the clarification of this disagreement must await further study.

Using the PAGE code, a study was performed on configuration variations with the goal of flowfield improvement. Computational results for the flow in a modified HGM with much improved fairing of the flow contour at the junction of the transfer ducts to the fishbowl outer wall predict that through proper inlet contouring it will be possible to further substantially reduce the extent of the stagnation/recirculation regions in the inner lower quadrants of the transfer ducts, or to perhaps eliminate them altogether. The same calculations also resulted in more uniform static and total pressure distributions over the transfer duct exit cross-section.

From a study of variations in the wall contours of the turnaround duct it is concluded that enlarging the cross-sectional area in the 180 deg bend where the largest losses occur should result in decreased pressure losses for a given mass flow or increased mass flow for a given pressure loss, i.e., a more efficient flow configuration.

Computational fluid dynamics has been applied to realistic flow problems in the SSME and found to be a useful tool for analysis. These results are, in fact, expected to influence the actual design of improved hardware. The three-dimensional flowfield calculations performed under this effort demonstrate what can be achieved with present computational technology. They require an intimate knowledge of the computational analysis on the side of the investigator and the most up to date computational resources available. To the designer, however, the computational analysis can provide details of the flow conditions which, previously, were largely inaccessible. Once a computational model has been set up, variations in the flow parameters or modifications in the flow geometry can be implemented with relative ease, helping future designs to be optimized before rather than after constructing the hardware.

6. REFERENCES

1. Pelaccio, Dennis G., "Duct Flow Nonuniformities Study," Final Report RI/RD83-160, Rockwell International, Rocketdyne Division, 30 June 1983.

2. Pelaccio, D.G., F.F. Lepore, G.M. O'Connor, G.V.R. Rao, G.H. Ratekin, S.T. Vogt, "Experimental Evaluation of an Advanced Space Shuttle Main Engine Hot-Gas Manifold Design Concept," 20th Joint Propulsion Conference, AIAA Paper 84-1463, June 1984.

3. Lepore, F.F., and Vogt, S., "Solid Wall Hot-Gas Manifold Testing Series IV Test Results," Rocketdyne Briefing No. ATU-83-006, Canoga Park, Calif., 13 January 1983.

4. Rosen, R., P.Y. Liang, Y.H. Quan, G.V.R. Rao, and T.T. Yang, "Investigation of a Complex Rocket Engine Manifold Flow to Determine its Major Characteristics," presented at AIAA/SAE/ASME 20th Joint Propulsion Conference, Cincinnati, Ohio, Paper No. 84-1462, June 1984.

5. Prozan, R.J., L.W. Spradley, P.G. Anderson, and M.L. Pearson, "The General Interpolants Method," AIAA Paper 77-642, Albuquerque, June 1977.

6. Spradley, L.W., J.F. Stalnaker, and A.W. Ratliff, "Solutions of the Three-Dimensional Navier-Stokes Equations on a Vector Processor," AIAA J., Vol. 19, No. 10, October 1981.

7. Gordon, W.J., and C.A. Hall, "Construction of Curvilinear Coordinate Systems and Applications to Mesh Generation," J. Numer. Math., Vol. 1, 1973, pp. 461-477.

8. Spradley, L.W., J.F. Stalnaker, M.A. Robinson, and K.E. Xiques, "Finite Element Algorithms for Compressible Flow Computation on a Supercomputer," Finite Elements in Fluids, Vol. 6, Edited by Gallagher, Corey, Oden, and Zienkiewicz, John Wiley, New York, 1984.

9. Schlichting, H., Grenzschicht-Theorie, 3rd Edition, Verlag G. Braun, Karlsruhe, 1958.